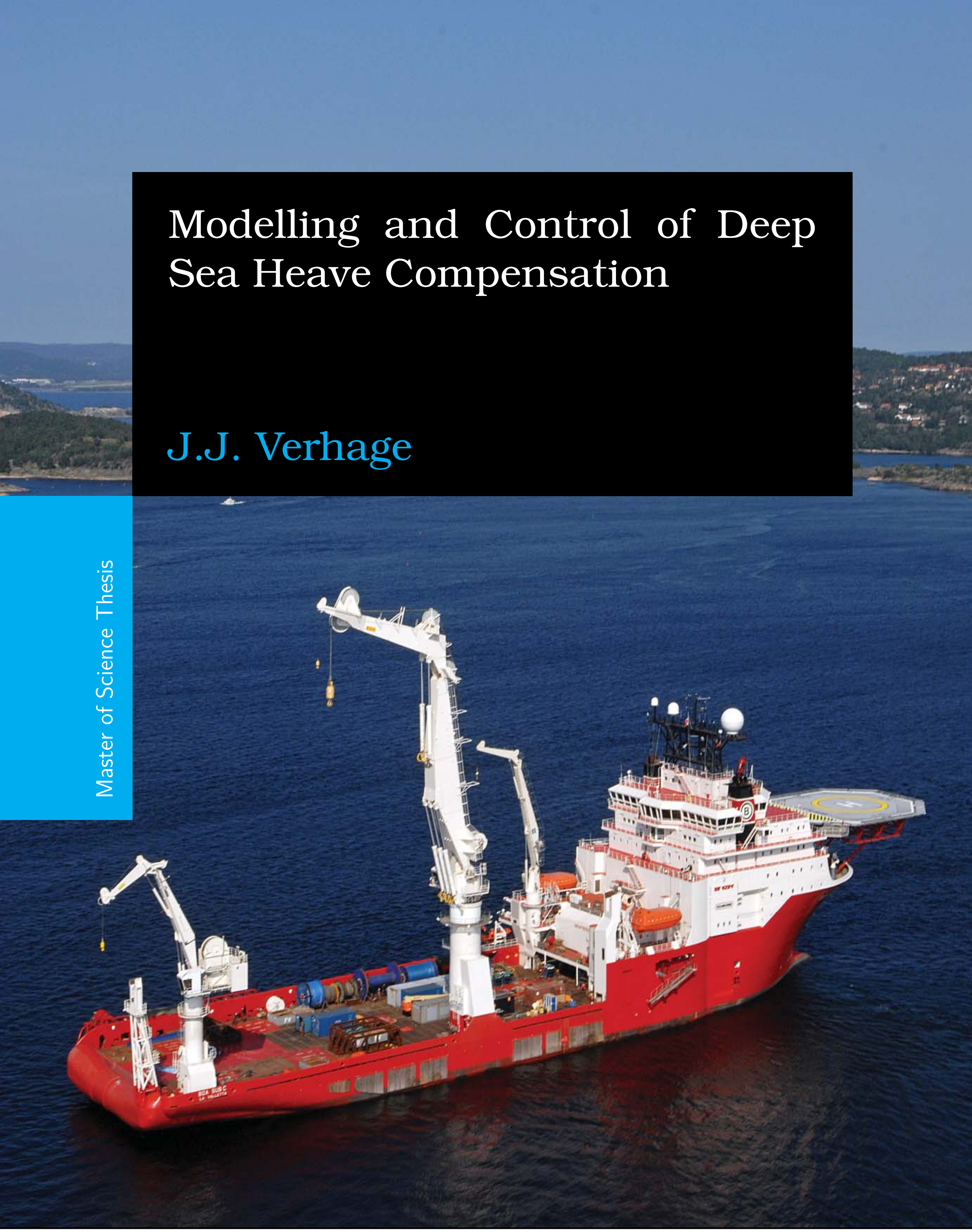

Modelling and Control of Deep Sea Heave Compensation

J.J. Verhage

Master of Science Thesis

TU Delft Delft University of Technology

Delft Center for Systems and Control

Modelling and Control of Deep Sea Heave Compensation

MASTER OF SCIENCE THESIS

For the degree of Master of Science in Systems and Control at Delft University of Technology

J.J. Verhage

November 7, 2017

Faculty of Mechanical, Maritime and Materials Engineering (3mE) · Delft University of Technology

The work in this Thesis is supported by IHC Systems, part of Royal IHC. Their cooperation is hereby gratefully acknowledged.

Abstract

Heave Compensation (HC) greatly improves the operability of lifting operations at sea, performed from ships under influence of heave motion. Especially with long cables and heavy payloads, the payload starts moving with larger amplitudes than the ship itself when no HC control is involved. HC aims to decouple the ships vertical motion due to the waves (the heave) with the cable, such that the cable and payload are as unaffected as possible by the heave motion. Several implementations are possible for HC, but in this Thesis only Hybrid Heave Compensation (HHC) is elaborated.

In order to decouple the cable from the ship's motion, the cable is actuated. In this Thesis a heave compensation cylinder is evaluated to control the cable length. This is a set of hydraulic cylinders between two sheaves, with the cable wound around them.

Cable dynamics are very important when lifting a payload to deep sea. Cable lengths of up to 3000 m are considered in this Thesis. In contrast to most papers on HC, a lot of effort is put in the cable model, which has proven to be necessary. In most papers, the cable is simulated as a single mass-spring-damper, which has consequently only one resonant frequency. The cable model in this Thesis is based on PDE equations and includes the first twenty resonant modes of the cable and payload. Simulations point out that multiple modes are significantly present in the payload motion and forces in the cable, which indicate that these resonant modes cannot be neglected.

The most basic control strategy in HC is feedforward on the heave measurement, which is taken as benchmark. A PID on velocity is added to the feedforward to assist in decoupling the ship from the cable, which is a common control strategy in HC. This controller however causes worse payload movement compared to the benchmark in simulations with long cable lengths. Another control strategy is feedback on the measured force at the top of the cable combined with the feedforward, which performs better than the benchmark. This controller however cannot cope with steady state errors, causing the heave compensation cylinder to drift to it's limits.

A better option is to combine the velocity and force feedback in parallel, combined with the feedforward. Two options for balancing between force and velocity feedback are evaluated under different working conditions; the controllers are simulated under multiple cable lengths, payload masses, noise and control delays. It turns out that force feedback combined with a low bandwidth velocity feedback performs best at the different scenarios. This is in comparison to velocity feedback with additional damping from the force PID and the benchmark controller. The parallel PID with emphasis on force feedback performs especially well on damping resonant modes in the cable and payload and limiting force variations. Under the conditions as in this Thesis, the parallel PID controller with emphasis on force feedback is recommended for use in HC control.

Contents

Preface

This document is a part of my Master of Science graduation Thesis. The subject of heave compensation in deep sea came from IHC, where doubts arose about the cable dynamics with long cables and how to cope with these using control. After being introduced to the subject I was also interested in the cable dynamics and how higher resonant frequencies influence the payload's motion. From the Literature Survey [1] conducted as initialisation to this Thesis, it followed that usually only a single mass-spring-damper is modelled as cable. Such an model is however a lot easier to control as less resonant frequencies have to be dealt with, and the model was assumed to deviate from reality especially with long cables. This interesting problem is handled in this Thesis and influences the control strategy and what can be achieved with control.

In this work I am greatly supported by my supervisors, both from the IHC Systems R&D Department and the Delft University of Technology. Namely my Supervisors at IHC, ir. P.M. Van den Bergh and ir. J. Osnabrugge and my Supervisor at the Delft Delft University of Technology, dr. ir. J.W. van Wingerden.

Chapter 1

Introduction

In a world with a high demand for energy, hard-to-reach oil fields at sea and wind farms are becoming more and more important. These two fields often require lifting operations at sea. In order to exploit an oil field located at deep sea, machinery is installed on the sea bed. This installation, and later on maintenance, requires lifting operations at sea. Building wind farms and maintaining them requires lifting too. In addition, there are numerous other fields which also require lifting operations at sea. Think of cargo transfer between ships, ROV deployment, salvaging, rescue operations, deep sea mining and offshore construction.

A mayor issue in lifting at sea is the vertical heave motion of a ship. This is transmitted to the on-board crane, which has to perform the lifting operation. If there is no control applied to the crane, the load's motion is affected by the ship's heave. These motions are paired with force variations in the lifting cable, whose tension can eventually become zero. This phenomenon causes slack wire, and can lead to large impacts on the cable or even to breaking it. Other problems arise if a soft landing of the payload on deck of another ship, the seabed or anything else is required, as pointed out in the proceeding Literature Survey [1]. The heave motion is very hard or even impossible to compensate for the human lifting operator.
This is why already in 1970 a paper was written with some proposals to reduce this heave induced motion according to [2]. This technique is further investigated and improved, and is called Heave Compensation (HC) in literature. Also in this Thesis it will be called like this. What HC involves and how it works is evaluated in Chapter 2.
A HC system can enlarge the operational window of lifting vessels, which depends on the sea state. Obviously, an effective HC leads to more safety, so lifting operations can safely be done at a rougher sea. Hence, by improving HC it is possible to reduce the downtime of lifting vessels due to a too rough sea. Other advantages of HC include less cargo loss (due to cable breaking) and more intuitive lifting control for the crane operator, which will increase the handling speed.

A special challenge in HC is the handling of a payload when the cable is very long, required for deep sea lifting ($\gtrsim 1$ km depth). These operations are for example necessary for deep sea mining, one of the markets in which the supporting company IHC Systems, part of Royal IHC (IHC) is active. An artist impression of deep sea mining is given in Figure 1-1. The depicted machinery has to be lowered safely to the sea bed, which can be several kilometres down. These operations and machinery are expensive, thus preventing damage due to the lifting process is valuable. The inevitably long cables used for these lifting operations however cause problems. The cable's stiffness is smaller for longer cable lengths, which brings the resonant frequencies of the cable closer to the frequencies contained in the heave motion. This can lead to large oscillations of the payload when the heave is not (fully) rejected with HC. The amplitude of these oscillations can be severe, which makes it impossible to softly land a payload on the sea bed.

Based on data from [3], only 11.7% of the world's sea floor is submerged between 0 and 1000 below sea level, compared to 24.8% which is between 0 and 3000 m. This shows that the area in which lifting operations can be performed increases a lot when deep sea is covered.

In this Thesis, the use of common uniform steel cables is assumed, as these are mostly used in HC. This choice limits the maximum cable length, because the specific density of steel is a lot higher than water, such that the cable has to hold a large fraction of it's own weight. This limits the depth at which the cable can be used. When considering a realistic safety margin and including the ability to hold a payload, a maximum operating depth is chosen as 3000 m down. The largest fraction of the sea bed is however located between 3 and 6 km down according to [3]. These depths might be reached when using steel cables with a variable diameter or polymer cables. In order to keep the investigation general applicable, the use of a regular steel cable is assumed as commonly used for HC in practice. The presented framework can however be used to investigate other cables.

Figure 1-1: An artist impression of deep sea mining equipment operating at the sea bed. This equipment has to be lowered carefully to the sea bed using lifting operations. Image courtesy of IHC

1-1 Problem Statement

The Problem statement is defined as followed:

"Design heave compensation controller to minimise payload motion and force variations for a cable length of up to 3000 m"

In this Thesis, the goal is to minimise the payload's motion and force variations, with emphasis on the payload motion. The payload is assumed to move only vertically, which is the only payload movement referred to in this work. This stabilisation of the payload is done by controlling a heave compensation system with a heave compensation cylinder (see Section 1-2). In this Thesis the control law is designed and validated to work with cable lengths of up to 3000 m.

1-2 Thesis Outline

An introduction to HC is given in Chapter 2, which also evaluates actuation principles for HC. Out of these, the mechanical HC configuration as visualised in Figure 1-2 is chosen for this Thesis. In this set-up, the heave compensation cylinder is responsible for minimizing the payload's motion (x_{load}), as induced by the heave (x_{heave}) of the ship. This hardware structure is described in Chapter 3. The winch is used to lower or raise the load according to the operator's demand, this movement is however not considered in this Thesis.

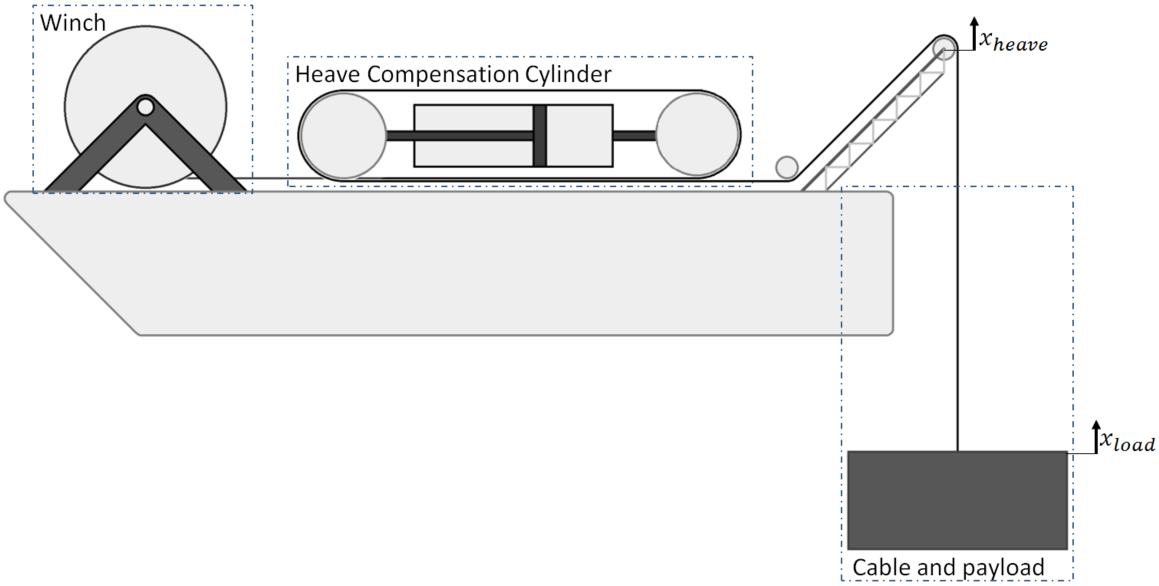

Figure 1-2: Mechanical design of the heave compensator on a ship, comprising of a winch, a heave compensation cylinder, a cable and a load. The variables x_{heave} and x_{load} are shown at the points where they are defined. Note that this figure is not drawn to scale.

In Chapter 4, the cable model is elaborated. The cable dynamics are very important in this Thesis, such that two different cable models are created and compared. Out of these, the most realistic model is taken for simulation and control. A range of controllers is designed in Chapter 5, which are all based on the PID structure. In this chapter, the best controllers are selected for one test case and assuming perfect measurements. In Chapter 6 these controllers are simulated with parameter variations (cable length and payload mass), noise and control delays. A conclusion of the results of this Thesis is given in Chapter 7.

Chapter 2

Introduction to Heave Compensation

In Chapter 1 the term Heave Compensation (HC) is introduced, which is elaborated in this chapter. There are three types of HC, which all aim to decouple the payload's motion from the ship's heave by changes in the cable length. These types are:

- Passive Heave Compensation (PHC)
- Active Heave Compensation (AHC)
- Hybrid Heave Compensation (HHC)

These groups are divided to their nature of actuation. PHC is heave compensation with a fully passive mechanical working principle. These systems are basically (non-linear) mass-spring-damper interconnections. AHC depends only on active actuation in order to decouple the payload from the ship. This method requires sensors and a controller to determine the desired actuation force. At last, HHC is a combination of both PHC and AHC. In this Thesis the type HHC is used, so first PHC and AHC have to be introduced to fully understand the working principle and to explain why HHC is chosen for this Thesis.

2-1 Passive Heave Compensation

A PHC system aims to reduce the transmission of the heave motion by inserting a relatively soft element in the cable. This results in a lower spring constant of the combined cable system which usually decouples the motion better than a stiff connection as a smaller force variation is present in the cable. When the combined system has an natural frequency in the range of the frequencies which are present in the heave, amplification of the heave motion can occur, which has to be avoided. According to [2], this is done by creating a system of which the damped natural frequency is placed below[1] the expected frequencies of the waves. When the

---

[1] This means that the natural frequency is only exited by very slow varying motions, slower than usual ship motions.

PHC system is well tuned, the heave motion is not transferred to the payload.
The mechanical design of those PHC systems often consist of a hydraulic cylinder between two sheaves. This cylinder is connected to a gas-backed accumulator such as depicted in Figure 2-1. Due to the large compressibility of gas with respect to oil and the large volume of the accumulator, the passive cylinder has a relatively low stiffness. The amount of gas in the accumulator is adapted to the static load of the payload and cable due to gravity. When done properly, the cylinder's piston moves around the centre of the cylinder's stroke with an appropriate stiffness. When the cylinder moves, the viscosity of the hydraulic fluid causes the damping.

2-2 Active Heave Compensation

In contrast to PHC, AHC aims to decouple the heave motion using active actuation. Most commonly, this works by measuring the motion of the vessel and calculating which vertical motion the crane tip undergoes. This signal is then used to control the cable length such that the heave motion is decoupled.
The actuation of AHC can be done in different ways. The two most used actuation methods are direct control of the winch or a heave compensation cylinder. It's an advantage of AHC that the behaviour of the system can be modified to a more desired one by control design. It is also possible to aim at other objectives, like a constant cable tension or to synchronize the motion of a payload to the deck of another vessel. A disadvantage of AHC in comparison to PHC is that AHC consumes energy. This power demand can be large compared to the total power demand of the ship when lifting heavy payloads.

2-3 Hybrid Heave Compensation

As the name says, Hybrid Heave Compensation (HHC) is a hybrid system, consisting of a PHC part and an AHC part. The HHC system utilizes in general a PHC setup to hold the load and decouple the load's motion in a passive, energy efficient manner. In parallel to the passive cylinder, a relatively small active cylinder is placed used to improve the performance. A common implementation of this combination is depicted in Figure 2-1, which is also the configuration as investigated in this Thesis.
Note that, like an AHC system, the HHC requires sensors, which can be quite expensive. However, the active actuator can be dimensioned a lot smaller, which reduces the cost a lot. The main advantage of an HHC system is the fact that it uses less energy than an AHC, with a better possible performance than a PHC. This advantage is at the cost of a still relatively expensive system due to the required machinery and less adaptable than an AHC system in for example following other references.

As stated, the winch itself can be used for heave compensation, but due to the use of inevitably long cables, the inertia of the winch's drum is very large when almost all of the cable is wound around it. In order to rotate such that the heave motion is cancelled, the drum has to

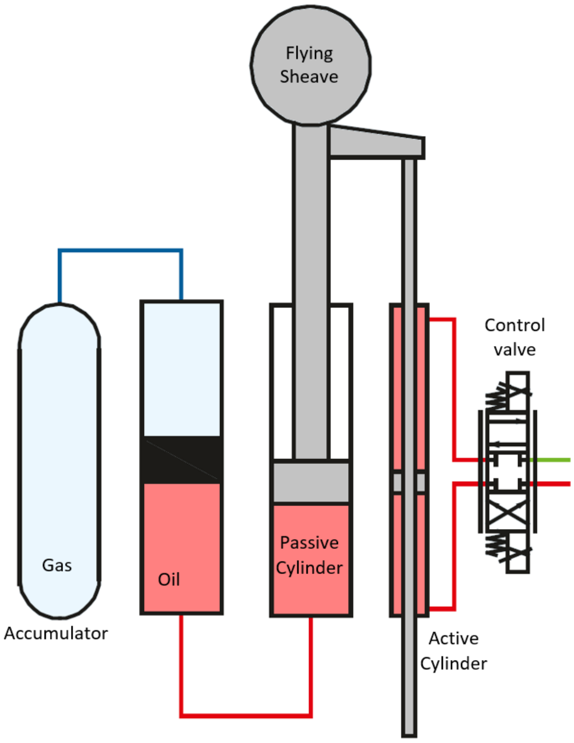

Figure 2-1: A general hybrid heave compensation system consisting of a hydraulic cylinder, a double acting active cylinder and an accumulator (not drawn to scale). Picture adapted from [4]

accelerate a lot, which requires a lot of force and power. In the case deep sea operations or heavy payload lifting, a large static load has to be dealt with, which results in high losses or the demand for a more complex regenerative system. When a heave compensation cylinder is used for AHC, the actuator's inertia is a lot smaller, but due to the static load there is still a high power demand.

In the case of HHC, the passive cylinder cancels the static load, which greatly reduces the forces which has to be delivered by the active cylinder, which in it's turn reduces the power demand. Given that heavy loads and cables are, it is safe to assume that HHC is chosen for use with deep sea HC.

Chapter 3

Modelling the Heave Compensation System

The entire heave compensation-system model is described in this chapter; both for simulation and control purposes. For each component a high fidelity (non-linear) model is constructed for simulation, a linearised model of the same part is derived from this model which is used for frequency analysis and control design in Chapter 5. The cable model itself is elaborated in Chapter 4, although the interconnections structure is defined here. The following sub-models are described in this chapter:

- heave compensation cylinder
- Inertial Measurement Unit (IMU)
- force sensor

The relevant mechanical parts are depicted in Figure 3-1, along with the definition of the most important positions and forces used as in-/outputs to the separate components:

x_{heave} = vertical position of the crane tip in the earth frame [m]
x_c = vertical position of the top of the cable model in the earth frame [m]
x_{act} = position of the actuator w.r.t. the initial position of the actuator [m]
x_{load} = vertical osition of the payload in the earth frame [m]
F_c = force exerted on the cable [N]
l_c = length of the cable [m]

The top of the cable (x_c) is a virtual position on the cable, which is as close as possible to the crane-tip and only moves vertically. The piece of cable between the winch and the depicted x_{act} is neglected, both in mass and stiffness. No lowering or raising of the payload

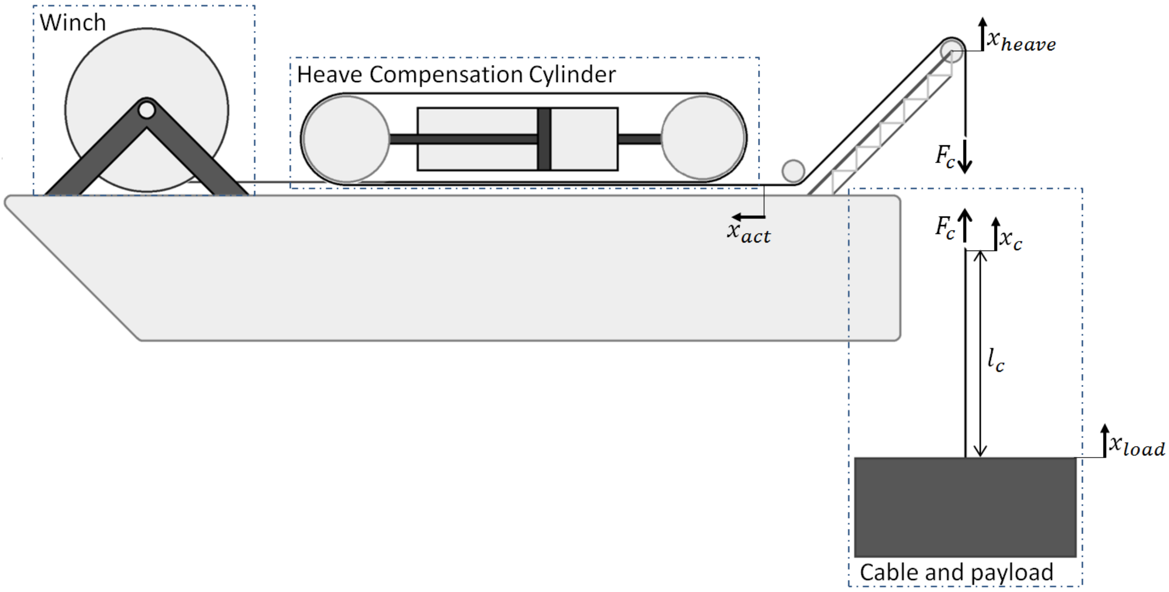

Figure 3-1: Variable definition of the heave compensator on a ship, comprising of a winch, a heave compensation cylinder, a cable and a load. Note that this figure is not drawn to scale.

is considered in this Thesis, the winch is therefore not modelled.
From the definition of the variables in Figure 3-1 it may be clear that:

$$x_c = x_{heave} - x_{act} \tag{3-1}$$

The foregoing equation is valid with proper definition of the cable length between the winch and x_c. The model is constructed such that the variables x_{heave}, x_c and x_{act} are all initialised on 0. In order to test the Heave Compensation (HC) system in a realistic way, a real project of IHC is taken as a guidance for physical system modelling. This provides a realistic combination of maximum cable length, cable properties, payload mass and actuator properties and dimensions.

3-0-1 Input and output definition

The framework in which the total system is modelled is depicted in the block scheme of Figure 3-2 which defines the in- and outputs of the different sub-models. The block scheme of Figure 3-2 is used for both the high fidelity and linearised models. The inputs of the block scheme are divided in control input (blue) and disturbances (red). The outputs are divided in measurements (blue) and performance output (red) as listed in Table 3-1. Instead of the positions as depicted in Figure 3-1, the respective velocities are used (denoted with $\dot{x}$, which is the derivative with respect to time).

3-1 Heave compensation cylinder

A heave compensation cylinder consists of a static and a flying sheave, with a set of hydraulic cylinders in between as depicted in Figure 3-3. When the sheaves are moved further away

Table 3-1: Input and output definition of the System Model

Control input			
v_{cont}	$=$	desired velocity of the actuator ($\dot{x}_{act}$)	[m/s]
Disturbances			
$\dot{x}_{heave}$	$=$	heave elevation velocity	[m/s]
F_{load}	$=$	disturbance force exerted at the payload	[N]
Output measurements			
F_{sens}	$=$	measured force in the cable	[N]
$\dot{x}_{act}$	$=$	velocity of the actuator	[m/s]
(Unmeasured) performance output			
$\dot{x}_{load}$	$=$	payload velocity	[m/s]

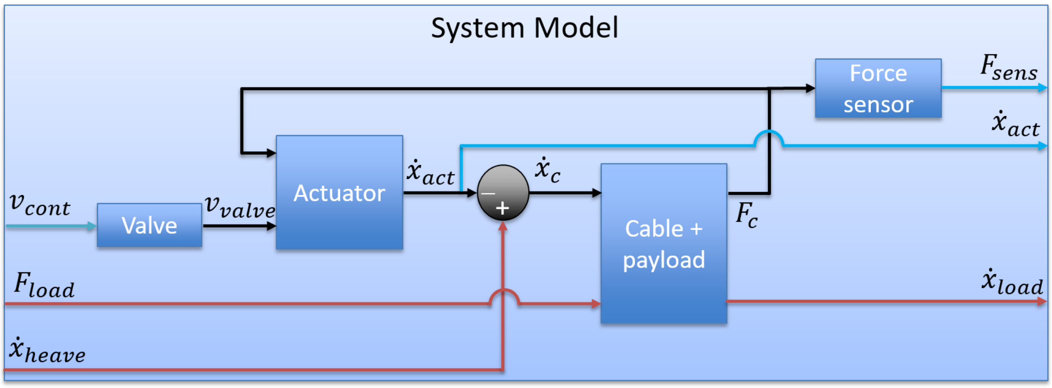

Figure 3-2: Block diagram of the system model with as (blue) controllable input v_{cont} from the controller and the (red) disturbances from a disturbance force F_{load} to the payload and the heave motion of the ship. The measured (blue) outputs of the system are the force at the top of the cable F_{sens} and the velocity of the actuator $\dot{x}_{act}$. In simulations the payload velocity $\dot{x}_{load}$ is available as performance channel, but this is not available for control.

from each other (a positive Δx_{cyl}), the effective length of the cable[1] decreases (which is an increase of x_{act}). Note that the cable can be wound around the heave compensation cylinder several times as in a pulley. For simplicity this possibility is not discussed in this Thesis.
As motivated in Section 2-3, the heave compensation cylinder is implemented as a hybrid actuator. In this set-up, a passive cylinder compensates for the static gravitational forces of the cable and payload while an active cylinder accounts for the movement and control. This is depicted in Figure 3-3, where the top cylinder is passive, and the smaller double sided cylinder on the bottom is the active cylinder.

The following assumptions are used in modelling the heave compensation cylinder:

- The cable's elongation between the sheaves is neglected as the cable length is small with respect to the cable length between the crane and the payload
- The velocity and position measurement of the hydraulic cylinder is ideal and available for control

---

[1] The effective length is the cable length between the winch and the payload

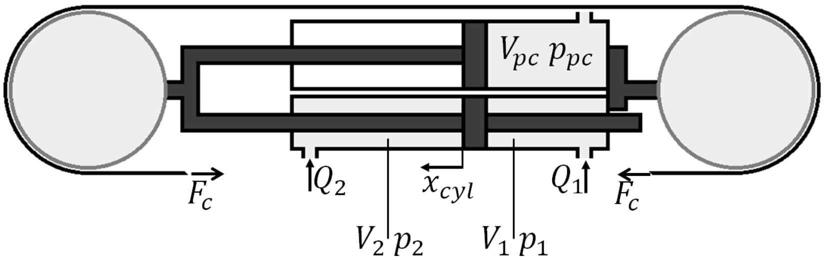

Figure 3-3: A schematic drawing of a heave compensation cylinder, consisting of a passive hydraulic cylinder (top), an active cylinder (bottom), a flying sheave (left) and a static sheave (right). The depicted variables are used in the modelling part of this section.

- Friction occurs only inside the hydraulic cylinder (thus not in the sheaves), containing coulomb and viscose friction.
- There is no (internal) leakage of hydraulic oil

Using these assumptions a model of the heave compensation cylinder is constructed based on Newtonian dynamics and the forces resulting from the pressures in each cylinder chamber as defined in Figure 3-3.

3-1-1 Mathematical Model of the heave compensation cylinder

The heave compensation cylinder model has to be compatible with the block diagram of Figure 3-2, which defines that the inputs are F_c and v_{valve}, and the output is $\dot{x}_{act}$. Therefore the valve is defined first. In Figure 3-4 the forces and displacements are defined with their respective positive directions. F_{cyl} in this figure is the resultant force of internal friction, the active and passive cylinder(not shown separately).

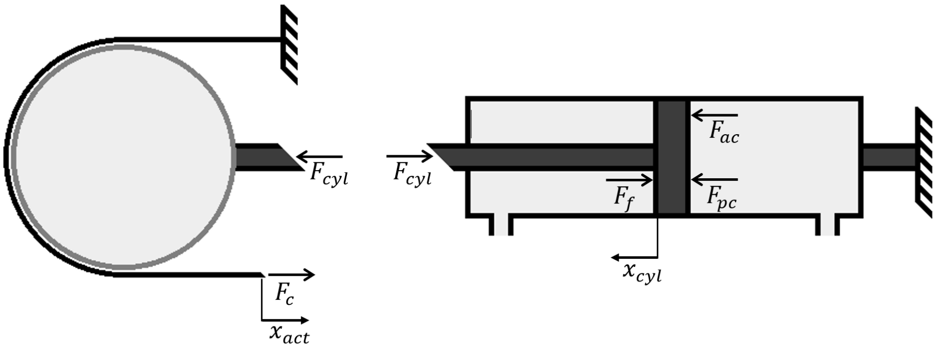

Figure 3-4: Free body diagram of the actuator showing the definition of forces and displacements. The hybrid cylinder combination is depicted as a single cylinder for simplicity.

With use of this free body diagram the forces can be related to each other using basic physics, assuming the actuator's moving mass is concentrated in the piston and that the sheave has no rotary inertia:

$$F_{cyl} = 2F_c \tag{3-2}$$

$$m_{act}\ddot{x}_{cyl} = F_{ac} + F_{pc} - F_f - F_{cyl} \tag{3-3}$$

$$x_{act} = -2x_{cyl} \tag{3-4}$$

With:

F_{ac}	=	active cylinder force	[N]
F_{pc}	=	passive cylinder force	[N]
F_f	=	friction force	[N]
x_{act}	=	actuator's output position	[m]
x_{cyl}	=	cylinder position	[m]
m_{act}	=	total moving mass of the heave compensation cylinder	[kg]

The variable x_{cyl} is taken such that $x_{cyl} = 0$ is located in the middle of the cylinder's stroke, which is also assumed to be the initial condition and coincides with $x_{act} = 0$. The forces of the cylinders are linearly dependent on the pressures inside, which have to be modelled.

3-1-2 Valve

The valve block which regulates the oil flow going in the heave compensation cylinder is modelled as a second order low-pass filter as the valve has some inertia, and consequently has a limited switching speed. v_{cont} is defined as the desired (output) velocity of the heave compensation cylinder ($\dot{x}_{act}$), while v_{valve} is the desired velocity of the hydraulic cylinder. Following from the time-derivative of Equation 3-4, the next relation is required:

- $v_{valve} = -\frac{1}{2}v_{cont}$ for low frequencies
- v_{valve} goes to 0 for high frequencies

This relation is implemented as a critical damped second order low pass filter, with a cut-off frequency of 250 rad/s, based on the specifications of valves in a comparable HC project within IHC.

Passive Cylinder dynamics

The pressure in the passive cylinder as depicted in Figure 3-3 is dominated by the pressure dynamics of the gas in the accumulator. This is due to the large compressibility of gas with respect to hydraulic oil and the typically large volume of the accumulator. The pressure can be calculated using the ideal gas equation, where the process can be considered as adiabatic, as stated in [4]. This leads to the following pressure-equation, followed by the formula for the force of the passive cylinder:

$$p_{pc} = p_{pc_0}\left(\frac{V_0}{V_0 + A_{pc}x_{cyl}}\right)^{\kappa} \tag{3-5}$$

$$F_{pc} = A_{pc}p_{pc} \tag{3-6}$$

With:
p_{pc} = pressure in the passive cylinder [Pa]
p_{pc_0} = static pressure component to hold the load [Pa]
V_0 = initial volume of the gas [m^3]
A_{pc} = passive cylinder area [m^2]
κ = adiabatic gas constant

According to [4], Equation 3-5 can be linearised around the working conditions of the passive cylinder by calculating the maximum and minimum pressure at the ends of the cylinder stroke. Based on this information, a linearised spring constant can be derived which brings the force-equation in the form of:

$$F_{pc-lin} = A_{pc}(p_{pc_0} - k_{pc}x_{cyl}) \tag{3-7}$$

With p_{pc_0} the pressure in the mid-position of the cylinder, which is the pressure which is set by the control operator to hold the static load of the cable and payload due to gravity.

Active Cylinder dynamics

The active cylinder is a double acting actuator with an equal pushing and pulling area as depicted in Figure 3-3. The actuator is controlled by the flow of oil Q into the chambers of the cylinder. The pressures (and coupled: force) inside the active cylinder change according to [5]:

$$\dot{p}_i = \frac{E_{oil}}{V_i}(Q_i - \dot{V}_i) \tag{3-8}$$

$$F_{ac} = A_{ac}(p_1 - p_2) \tag{3-9}$$

With:
p_i = pressure inside active cylinder at side i [Pa]
E_{oil} = Young's modulus of hydraulic oil [N/m^2]
V_i = volume inside cylinder inclusive hosing of side i [m^3]
Q_i = volume flow of hydraulic oil [m^3/s]
A_{ac} = active cylinder area [m^2]

According to [5], E_{oil} is variable with respect to the pressure. In this Thesis E_{oil} is taken as a constant for simplicity, as also done in for example [4]. As both sides of the active cylinder have the same pushing area, the flows are coupled using:

$$Q_1 = -Q_2 \tag{3-10}$$

The values of p_1 and p_2 are in itself not relevant[2] to calculate F_{ac}, but the pressure difference is, as can be seen in Equation 3-9, which motivates to insert a new variable Δp:

$$\begin{aligned} \dot{\Delta p} &= \dot{p}_1 - \dot{p}_2 && \text{(3-11)} \\ &= E_{oil}\left(\frac{\dot{Q}_1 - \dot{V}_1}{V_1} + \frac{\dot{Q}_1 - \dot{V}_1}{V_2}\right) && \text{(3-12)} \end{aligned}$$

---

[2] Note that there are still bounds in physical systems for the pressures p_1 and p_2 such as maximum and minimum pressures, which will be considered in the non-linear simulations

This equation is non-linear due to the division by variables V_1 and V_2. The equation is linearised by taking constant $A_{ac}c_{ac}$ which is representative for the working range of the heave compensation cylinder which replaces both V_1 and V_2. By inserting this constant in Equation 3-12 the formula can be written as:

$$\dot{\Delta p} = 2E_{oil}\frac{\dot{Q}_1 - A_{ac}\dot{x}_{cyl}}{A_{ac}c_{ac}} \tag{3-13}$$

This equation shows that a flow of $Q_1 = A_{ac}v_{valve}$ results in a constant pressure when $v_{valve} = \dot{x}_{cyl}$. It can be shown that a constant oil flow of $A_{ac}v_{valve}$ results in $\dot{x}_{cyl} \approx v_{valve}$, which motivates to use:

$$Q_1 = A_{ac}v_{valve} \tag{3-14}$$

Finally the linearised equation for $\dot{\Delta p}$ is written as:

$$\dot{\Delta p} = 2\frac{E_{oil}}{c_{ac}}(v_{valve} - \dot{x}_{cyl}) \tag{3-15}$$

3-1-3 Friction forces in the heave compensation cylinder

The friction forces in the heave compensation cylinder are assumed to be composed of viscose damping and Coulomb friction. The first is coming from movement of the oil, while the second is generated by the seal of the piston. According to [4], a rule of thumb for this coulomb friction is $1 - 2\%$ of the maximum force of the actuator. With:

$$F_f = d_{visc}\dot{x}_{cyl} + F_{coul}\ \text{sign}(\dot{x}_{cyl}) \tag{3-16}$$

With:

d_{visc}	=	Viscose damping term of the cylinder	[Ns/m]
F_{coul}	=	Static coulomb friction force	[N]

Where sign(x) is: 1 for $x > 0$, 0 for $x = 0$ and -1 for $x < 0$. Note that F_{coul} is static, which results in stick-slip behaviour in simulations. For linear control design, this is linearised in a working range to:

$$F_{f-lin} = d_{cyl}\dot{x}_{cyl} \tag{3-17}$$

With:

d_{cyl}	=	linearised damping constant of the heave compensation cylinder	[Ns/m]

3-1-4 State space of the heave compensation cylinder

The linearised model of the heave compensation cylinder can now be constructed by substitution of the previous equations in Equation 3-3:

$$m_{act}\ddot{x}_{cyl} = A_{ac}\Delta p + A_{pc}(p_{pc_0} - k_{pc}x_{cyl}) - d_{cyl}\dot{x}_{cyl} - 2F_{act} \tag{3-18}$$

Combined with Equation 3-15, the state space system can be set up:

$$\begin{bmatrix}\ddot{x}_{cyl}\\ \dot{x}_{cyl}\\ \dot{\Delta p}\end{bmatrix} = \begin{bmatrix}-\frac{d_{cyl}}{m_{act}} & -\frac{k_{pc}}{m_{act}} & \frac{A_{ac}}{m_{act}}\\ 1 & 0 & 0\\ -2\frac{E_{oil}}{c_{ac}} & 0 & 0\end{bmatrix}\begin{bmatrix}\dot{x}_{cyl}\\ x_{cyl}\\ \Delta p\end{bmatrix} + \begin{bmatrix}-\frac{1}{m_{act}} & 0\\ 0 & 0\\ 0 & -\frac{E_{oil}}{2}\end{bmatrix}\begin{bmatrix}2F_c - A_{pc}p_{pc_0}\\ v_{valve}\end{bmatrix} \tag{3-19}$$

$$\dot{x}_{act} = \begin{bmatrix}-2 & 0 & 0\end{bmatrix}\begin{bmatrix}\dot{x}_{cyl}\\ x_{cyl}\\ \Delta p\end{bmatrix} + \begin{bmatrix}0 & 0\end{bmatrix}\begin{bmatrix}2F_{act} - A_{pc}p_{pc_0}\\ v_{valve}\end{bmatrix} \tag{3-20}$$

$$\tag{3-21}$$

Note that the first input is F_c minus the static force of the passive cylinder ($A_{pc}p_{pc_0}$) which makes the state space system non-linear.This offset cancels out with the gravitational force of the cable, which makes the combination linear again.

3-1-5 Non-linear simulation implementation

The equations as presented in the sections before still allow for unrealistic situations, which require some attention. In order to make the heave compensation cylinder behave realistically, several constraints, inspired by physical systems, are implemented:

- A maximum oil flow entering or leaving the heave compensation cylinder, which is bounded by the flow which can be delivered by the hydraulic pump
- The constraint that the oil can only flow from high pressure to a lower pressure, and that the maximum flow is limited in case of small differential pressures. As a maximum pressure the maximum pressure of the pump is taken, and as a minimum the pressure of the sink
- The piston's position is bounded

3-2 IMU and Force Sensor

The IMU which is modelled in this Thesis is a Kongsberg Seatex MRU H which is specially designed for HC. This IMU has a maximum output data rate of 200 Hz and is able to calculate

the vertical heave velocity of the crane tip[3]. The noise of this sensor is modelled using two noise sources, angular rate noise (0.1 °/s RMS) and acceleration noise (0.01 m/s^2 RMS), which are defined in the data sheet of the IMU. These sources are converted to the vertical movement which is outputted for the crane tip. This point is assumed to be 5 m away from the IMU in order to convert the angular rate noise to a vertical noise.
The output of the IMU is taken with a frequency of 100 Hz, which is fast enough to facilitate control and enables additional filtering in the IMU. In Chapter 5 only the heave velocity $\dot{x}_{IMU}$ is used. This measurement is modelled with:

$$\dot{x}_{IMU}(t) = \dot{x}_{heave}(t) + \int_0^t 0.01 n_1(t)dt + 0.1 \cdot 5\frac{2\pi}{360}n_2(t) \tag{3-22}$$

With:

n_1, n_2	=	independent white noise sources	
$\dot{x}_{IMU}$	=	heave velocity measurement by the IMU	[m/s]

The force is measured by strain gauges on the rod between the sheave and the hydraulic cylinders of the heave compensation cylinder, at the point where F_{cyl} is depicted in Figure 3-4. This force is easily converted to F_c, assuming the inertia and friction of the sheave can be neglected.

3-3 Conclusion on Modelling the Heave Compensation System

The interconnection of the different parts of the heave compensation system is defined in this Chapter, as well as the heave compensation cylinder, valve, IMU and force sensor models. The pressure dynamics of the active and passive hydraulic cylinders of the heave compensation cylinder and how this relates to the control signal is modelled. Combined with the external force from the cable and friction forces the heave compensation cylinder model is constructed. A high fidelity non-linear simulation model is defined first and, after which the model is linearised for control design in the frequency domain. Additionally the sensor noise of the IMU and force measurements are defined which will be used in simulations.

---

[3] As well as other variables, but the velocity is most important in this Thesis (see Chapter 5)

Chapter 4

Modelling of the Cable and Payload

The cable length required for deep sea operations is inevitably long, which makes the cable heavy with respect to the payload. As mentioned in the Literature Survey [1], conducted as initialisation of this Thesis, it is doubted that modelling the cable using a single mass-spring-damper interconnection is sufficient as done in most of the papers about Heave Compensation (HC), like [6, 7]. In such systems, only the first resonance mode of the cable and load combination is evaluated. By increasing the length of the cable, all resonant modes get lower frequencies, which imply for these cables that more resonant frequencies are in the range of the disturbances on the cable. Based on simulations with the cable model which is described in this chapter, the inclusion of multiple resonant frequencies is important. This follows from the fact that these resonant frequencies can be identified in the payload motion during simulations with and without controller.
In order to model the cable and payload with multiple modes, two techniques are elaborated:

- division of the cable in multiple sections connected with springs and dampers
- modelling the cable using Partial Differential Equation (PDE)

Both of these methods are used to model the same cable and payload in this Chapter, which are compared afterwards. Out of these, the best method is used to simulate the cable-payload combination. The other cable model is used as validation that the order of magnitude is correct for both models. This is in order to guarantee that the cable dynamics are realistic, as there are no measurements available to compare with.

Both models are built using the following assumptions:

- Only longitudinal vibrations are significant, transverse vibrations are neglected
- The cross-section of the cable is constant, and is independent of deformations[1]

---

[1] For example the deformations as described by Poisson which describe that when a cross-section is under pressure in one direction, the material deforms outward in the other directions.

- The gravitational forces are large enough to maintain a positive tension in the cable as a cable cannot 'push'. In the models this constraint is not implemented, which means that effectively the cable can 'push'. Later on a check will be done whether or not the tension remains positive.

Both of these models are constructed with the input and outputs as defined in Figure 4-1. These variables are defined as:

$\dot{x}_c$	=	vertical velocity of the top of the cable model in the earth frame	[m/s]
$\dot{x}_{load}$	=	vertical velocity of the payload in the earth frame	[m/s]
F_c	=	force exerted on the cable	[N]

Note that the payload's motion is not measured in practice, so this cannot be used for control purposes. As this motion is desired to be minimized, this variable is taken as a performance output.

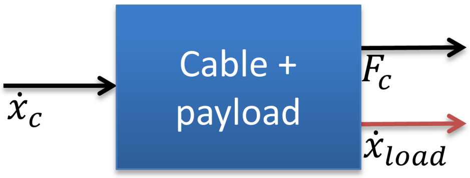

Figure 4-1: Block representation of the cable model, as defined in Figure 3-2. The input to the cable is $\dot{x}_c$, and the measurable output is F_c. The model also provides the unmeasured $\dot{x}_{load}$.

First the cable and payload are modelled using division in sections (Section 4-1), secondly the model using PDE is constructed (Section 4-2), followed by the damping forces and added-mass in Section 4-3.

4-1 Modelling using multiple cable sections

The cable's continuous distributed mass can be approximated by dividing the cable in multiple equal cable sections. These sections itself are modelled using a point-masses, which are connected to other sections using springs and dampers as depicted in Figure 4-2. Note that the schematic has to be rotated clockwise to obtain the vertical cable with payload. When the cable is divided in n equal sections, the distributed parameters are:

$$m_{sect} = \rho_c A_c l_{sect} \tag{4-1}$$

$$l_{sect} = \frac{l_c}{n} \tag{4-2}$$

$$k = \frac{E_c A_c}{l_{sect}} \tag{4-3}$$

With:

m_{sect} = mass of one cable element [kg]
ρ_c = the cable's specific density [kg/m^3]
A_c = cross-sectional area of the cable [m^2]
l_{sect} = length of each section(un-stretched) [m]
l_c = length of the cable (un-stretched) [m]
n = number of sections
k = spring constant [N/m]
E_c = Young's modulus [N/m^2]

The damping factor d as depicted in Figure 4-2 is defined in Section 4-3. The dynamical equations are constructed using $F = m\ddot{x}$ where the force F is a combination of forces from the springs, dampers, gravity and interactions with water which are defined in Section 4-3. $\dot{x}_c$ is the input to the cable, F_c and x_{n+1} are respectively the available output and the unmeasured position of the payload. F_c is a combination of only the spring and damper forces at the left side of m_1.

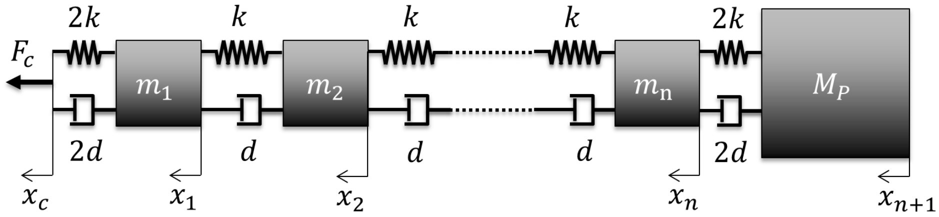

Figure 4-2: Schematic of a cascade of mass-spring-damper systems which can be used for modelling the cable. In this figure x_i denotes the displacement, m_i a point mass for modelling the cables weight, M_P is the payload's mass, k denotes the spring stiffness, d the damping factor and F_c is the force at the top of the cable. Note that the scheme has to be rotated clockwise to obtain the vertical cable with payload.

4-2 Modelling using a Partial Differential Equation

The longitudinal cable dynamics can also be described using a PDE. In [8] a model can be found of longitudinal vibrations of a solid bar under various boundary conditions, including a mass at one end. A schematic drawing of this model used in the book can be seen in Figure 4-3. The governing equation for longitudinal vibrations the cable is [8]:

$$E_c A_c \frac{\partial^2 u}{\partial x^2}(x,t) + f(x,t) = \rho_c A_c \frac{\partial^2 u}{\partial t^2}(x,t) \tag{4-4}$$

With:
x = position on the cable relative to the top [m]
t = time [s]
$u(x,t)$ = axial displacement of the cable due to stretch [m]
$f(x,t)$ = external force exerted on the cable at point x [N]

The position x refers to the position of a point of the un-stretched cable. When the cable stretches, the distance between the points $x = 0$ and $x = l_c$ is therefore not equal to l_c.

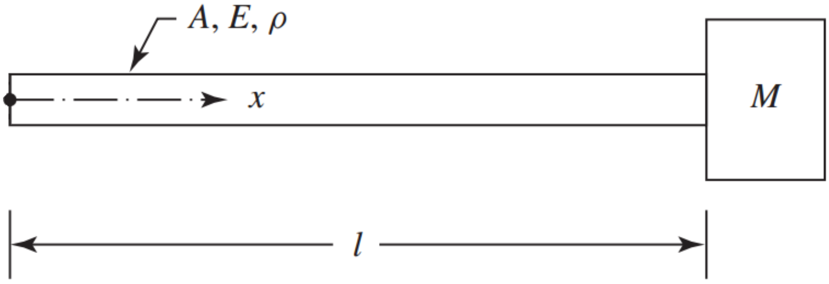

Figure 4-3: Model definition of a mass (payload) attached to a bar (cable). When the model is rotated clockwise, serves as a model for the cable, assuming that gravitational forces are large enough to maintain a positive tension in the cable. In this figure, $M \equiv M_p$ and $l \equiv l_c$ as used in this Thesis. Figure taken and edited from [8]

4-2-1 PDE: mode shapes and natural frequencies under free vibration

The free vibration mode shapes and natural frequencies as a solution to Equation 4-2 have to be found. This implies that no external force is exerted on the cable, so $f(x,t) = 0 \; \forall x, t$. These solutions are determined in the following way, inspired by the method presented in [8]:

Define the constant c in order to simplify Equation 4-2[2]:

$$c = \sqrt{\frac{E_c}{\rho_c}} \tag{4-5}$$

Equation 4-2 can now be written as:

$$c^2 \frac{\partial^2 u}{\partial x^2}(x,t) = \frac{\partial^2 u}{\partial t^2}(x,t) \tag{4-6}$$

This equation is solved using the technique of separation of variables resulting in (see Appendix A-1):

$$u(x,t) = \sum_{i=1}^{\infty} U_i(x) T_i(t) \tag{4-7}$$

$$U_i(x) = \alpha_{1_i} \cos\left(\frac{\omega_i x}{c}\right) + \alpha_{2_i} \sin\left(\frac{\omega_i x}{c}\right) \tag{4-8}$$

$$T_i(t) = \alpha_{3_i} \cos(\omega_i t) + \alpha_{4_i} \sin(\omega_i t) \tag{4-9}$$

With:

$U(x)$	=	mode shape of the cable	[m]
$T(t)$	=	homogeneous evolution over time	
α_i	=	scaling factor	
ω	=	frequency of vibration	[rad/s]

In order to solve the PDE for ω, the boundary conditions have to be defined:

---

[2] The constant c is actually the speed of sound in a solid, which shows how fast vibrations travel the cable

- The top of the cable is free. Later on this position will be coupled to the actuator[3]
- The payload with mass M_p is connected to the bottom end of the cable

When defining the top of the cable as $x = 0$ and the bottom of the cable as $x = l_c$ as in Figure 4-3, the boundary conditions are set up. As the top of the cable is free, the exerted force on the boundary is zero[4]. A force of zero implies a local stretch of zero, therefore the boundary condition at the top is defined as:

$$\frac{\partial u}{\partial x}(x=0,t) = 0 \tag{4-10}$$

On the bottom, the payload is connected, as shown in Figure 4-4. The force balance is derived as:

$$\underbrace{E_c A_c \frac{\partial u}{\partial x}(x=l_c,t)}_{\text{Force in cable at } (x=l_c)} = -\underbrace{M_p \frac{\partial^2 u}{\partial t^2}(x=l_c,t)}_{\text{Inertial Force Payload}} \tag{4-11}$$

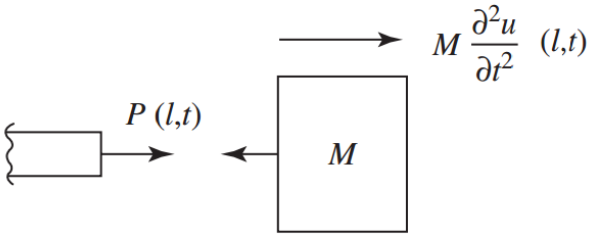

Figure 4-4: Model definition of a mass (payload) attached to the cable, showing the cable and inertial force. $P(l,t)$ in the figure is equal to $E_c A_c \frac{\partial u}{\partial x}(x = l_c, t)$ in Equation 4-11. In this figure, $M \equiv M_p$ as used in this thesis. Figure taken and modified from [8]

As $\frac{\partial u}{\partial x}(x=0,t) \equiv 0$, it follows that:

$$\frac{\partial U}{\partial x}(x=0)\cdot T(t) \equiv 0 \tag{4-12}$$

As $T(t) = 0$ means that the cable does not stretch for any t at any position[5], it follows that $\frac{\partial U}{\partial x}(x=0) = 0$. Hence $\alpha_2 = 0$ as derived from Equation 4-8. Next $u(x,t)$ is substituted in Equation 4-11. By neglecting the trivial solution $T(t) \equiv 0$, the equation is rewritten to:

$$\tan(\psi_i) = -\psi_i \frac{M_p}{\rho_c A_c l_c} \tag{4-13}$$

---

[3] An other approach would be to set the boundary as 'fixed', but this ends up in having the double derivative of x_c as input instead of a force, which is hard to robustly interconnect in simulations, which motivates the use of this.

[4] This is only in the case of the homogeneous solution and this does not imply that no forces can be applied at this point

[5] This is the trivial solution in which the cable does not move at all

With $\psi_i = \frac{\omega_i l_c}{c_c}$. This equality can be solved for all eigen-frequencies ω_i, which results in an infinite number of solutions ω_n. Out of these, only the first number of non-negative eigen-frequencies are in the frequency range of interest of the cable model. How much modes are required depends on various factors, like the cable length and the damping factors and is elaborated in Section 4-4.

It can be proven that the eigen-frequencies ω_i result in orthogonal mode shapes, with:

$$\rho_c A_c \int_0^{l_c} U_i(x)U_j(x)dx + M_p U_i(x = l_c)U_j(x = l_c) = 0 \tag{4-14}$$

for any $i \neq j$. For a derivation of this, see Appendix A-2. This orthogonality makes it possible to investigate each mode separately, as different modes do not affect each other [8]. As a result, the free vibration result can be written as a sum of the different modes. Without loss of generality, $\alpha_1 = 1$ and the $\alpha_{3,4}$'s depend on the initial conditions of the cable:

$$u(x,t) = \sum_{i=1}^{\text{inf}} \underbrace{\cos\left(\frac{\omega_i x}{c}\right)}_{\text{Mode Shape}} \underbrace{\left(\alpha_{3_i}\cos(\omega_i t) + \alpha_{4_i}\sin(\omega_i t)\right)}_{\text{Harmonic evolution over time}} \tag{4-15}$$

4-2-2 PDE: Forced Response

The purpose of the cable model is to create a mapping between the forces acting on the cable and the displacements at specific points on the cable, or the other way around. This can be done by calculating the effect of any force, on any part of the cable. In this Thesis, the important forces which have to be modelled are:

F_{top} The force at the top of the cable, due to the connection to the ship and the actuator.

F_{bot} The force at the bottom of the cable, due to for example damping forces at the payload and external disturbances.

F_{grav} Gravity force, acting at every single point of the cable.

The forced response of the combined cable and payload is derived in Appendix A-3 and can be denoted as:

$$\ddot{\eta}_i(t) = -\omega_i^2 \eta_i(t) + \frac{\int_0^{l_c} f(x,t)U_i(x)dx}{M_i} \tag{4-16}$$

$$M_i = \rho_c A_c \int_0^{l_c} U_i^2(x)dx + M_p U_i^2(x = l_c) \tag{4-17}$$

With:
η_i = modal coordinate of mode shape i
M_i = generalized inertia of mode i

Note that $\eta_i = T_i(t)$ when $f(x,t) \equiv 0$. Equation 4-16 can be simplified for the case of concentrated forces (like F_c, F_{bot}) or gravitational forces. Following the methods described in [8], the response from a concentrated force can be written as:

$$\ddot{\eta}_i(t) = -\omega_i^2 \eta_i(t) + \frac{U_i(x = x_F)}{M_i} F_{x_F}(t) \tag{4-18}$$

Where x_F is the point where the force acts on, and $F_{x_F}(t)$ is the force acting on x_F. The gravitational force has to be divided in a distributed force on the cable and a concentrated force for the payload. Note that the cable and payload are submerged, which imply that a buoyancy force is also present, which partly counteracts the effect of gravity. To account for this phenomena, the specific density of water (ρ_w) is subtracted from that of the cable in the gravity calculations. Furthermore, the submerged weight of the payload is used, denoted as M_{wet} [kg]:

$$\ddot{\eta}_i(t) = -\omega_i^2 \eta_i(t) + \frac{(\rho_c - \rho_w) A_c \int_0^{l_c} U_i(x) dx + M_{wet} U_i(x = l_c)}{M_i} g \tag{4-19}$$

With:

g	=	gravitational acceleration	[m/s^2]
ρ_w	=	specific density of water	[kg/m^3]
M_{wet}	=	submerged weight of the payload	[kg]

These equations are rewritten in State-Space form:

$$\dot{x}_i(t) = A_i x_i(t) + B_i u(t) \tag{4-20}$$

$$y_i(t) = C_i x(t) + D_i u(t) \tag{4-21}$$

With:

$$x_i(t) = \begin{bmatrix} \dot{\eta}_i(t) \\ \eta_i(t) \end{bmatrix} \tag{4-22}$$

$$A_i = \begin{bmatrix} 1 & 0 \\ 0 & -w_i^2 \end{bmatrix} \tag{4-23}$$

The input matrix B_i is a combination of the different forces. When the only forces acting on the system (which are contained in $u(t)$) are defined as, where F_{grav} is basically the gravitational constant:

$$u(t) = \begin{bmatrix} F_{top}(t) \\ F_{bot}(t) \\ F_{grav} \end{bmatrix} \tag{4-24}$$

Then B_i is defined as:

$$B_i = \frac{1}{M_i} \begin{bmatrix} U_i(x=0) & U_i(x=l_c) & (\rho_c - \rho_w)A_c \int_0^{l_c} U_i(x)dx + M_{wet}U_i(x=l_c) \\ 0 & 0 & 0 \end{bmatrix} \tag{4-25}$$

This B_i can be extended when other inputs are defined. The output matrices C_i and D_i have to be defined using the desired outputs. The deflection of mode i on point x_y at time t with respect to the un-stretched cable is calculated by multiplying $\eta_i(t)$ with $U_i(x_y)$. The velocity at this point can be calculated by multiplying $\dot{\eta}_i(t)$ with $U_i(x_y)$. Equation 4-7 is used to obtain these entities for all mode shapes together, when $T_i(t)$ of the homogeneous solution is replaced by $\eta_i(t)$.

4-2-3 Input-output connection of the PDE

As for example shown in Figure 4-1, the input to the model has to be $\dot{x}_c$, while the outputs are F_c and the unmeasured x_{load}. This convention has to do with the actuator model, such that an extra part has to be added to the PDE model. This extra part is a tiny piece of cable that is placed between the top of the cable model and the cable connected to the actuator as depicted in Figure 4-5.

The piece of cable in between is taken very small, such that it's stiffness is very high and it's mass can be neglected. Because of this, $F_c \approx F_{top}$, which is motivated by the relatively small accelerations which are expected at this point due to the inertia of the actuator. When this piece of cable is properly damped, x_{top} approaches x_c, where x_{top} coincides with $x = 0$. Note that this piece of cable adds an extra resonant mode to the system, but when it's damping is adequate and the stiffness is sufficiently high, this mode is out of the frequency band of interest. The block-implementation of this is depicted in Figure 4-6, where the in- and outputs indeed match the desired ones as in Figure 4-1.

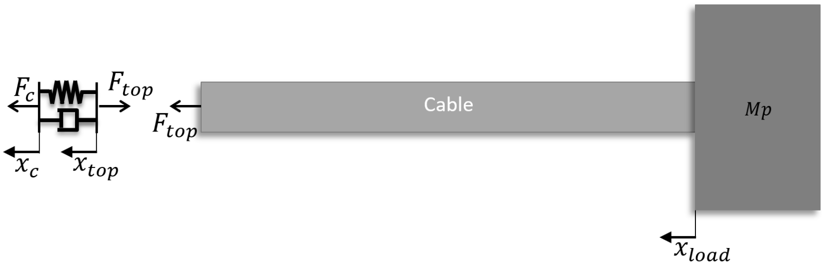

Figure 4-5: Connection between the PDE cable model and the ship using a tiny piece of cable, modelled as a stiff massless spring and damper. F_{top} and x_{top} are respectively the force and position at $x = 0$, while F_c and x_c are the force respectively the position of the top of the cable model.

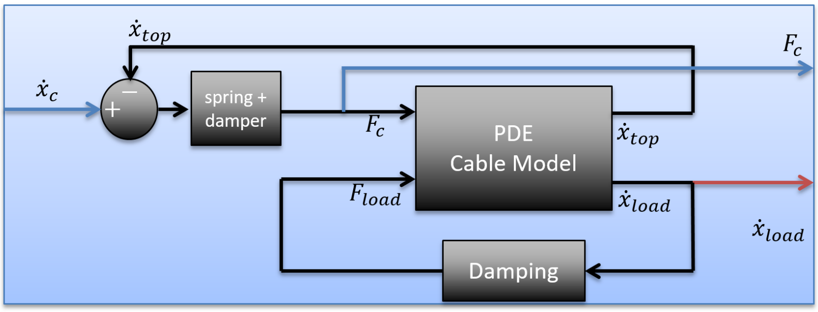

Figure 4-6: Block Scheme of the PDE model implemented such that the inputs and outputs match the desired ones by use of a spring and damper. The implementation of the linear or non-linear payload damping is also shown, as well as the unmeasured payload velocity $\dot{x}_{load}$.

4-3 Additional forces acting on the cable-payload

There are two major types of damping which affect the motion of the cable and the payload. The first is internal friction of the cable and the second is by hydrodynamic forces caused by movement of the cable with respect to the surrounding water. Additionally the so-called 'added mass' is implemented.

Internal damping in the cable

The internal damping is hard to determine, so a general 'material damping term' of $\zeta = 0.01$ is used as an order of magnitude for steel, with ζ the damping factor. In case of the PDE the damping force on mode i is equal to $-2\zeta\dot{\eta}_i$, which is directly inserted in the PDE Model.

The material damping for the Section Model has to be tuned for a specific resonant frequency. This is taken as the first natural frequency ω, which is the closest to (or in) the frequency range of the heaves for each evaluated case. The damping d for use in the Section Model is calculated as:

$$d = 2n\zeta\omega\rho_c A_c l_c \tag{4-26}$$

Where $\rho_c A_c l_c$ is the total mass of the cable and the n term (the number of sections in the Section Model) is caused by the smaller relative velocities between x_i and x_{i+1} for a sectioned cable.

Hydrodynamic damping of the cable and payload

The hydrodynamic forces are determined using [9] which states that:

$$f_{c-w}(x,t) = \frac{1}{2}\rho_w d_{c-w}\pi D_c \left|\dot{u}(x,t)\right| \dot{u}(x,t) \tag{4-27}$$

$$F_{p-w}(t) = \frac{1}{2}\rho_w d_{p-w} A_p \left|\dot{u}(x=l_c,t)\right| \dot{u}(x=l_c,t) \tag{4-28}$$

With:
f_{c-w} = hydrodynamic damping force of the cable [Ns/m]
F_{p-w} = hydrodynamic damping force of the payload [Ns/m]
ρ_w = specific density of water [kg/m^3]
d_{c-w} = hydrodynamic damping term of cable due to water
d_{p-w} = hydrodynamic damping term of payload due to water
D_c = diameter of the cable [m]
A_p = (vertical) projected area of the payload [m^2]
u = vertical deflection of the cable at point x [m]

Where d_{c-w} has an order of magnitude of 0.02 and d_{p-w} is around 1 according to [9][6]. Note that the damping force in Formula 4-27 is per unit length of the cable. In case of the Section Model, the hydrodynamic damping force is approximated as:

$$F_{d_{sect-h}} = \frac{1}{2}\rho_w d_{c-w} \pi D_c l_{sect} \left|\dot{x}_i(t)\right| \dot{x}_i(t) \tag{4-29}$$

The hydrodynamic damping force in the PDE model is calculated by inserting the speed of the cable in each mode as function of $\eta(t)$:

$$f_i(x,t) = \frac{1}{2}\rho_w d_{c-w} \pi D_c U_i(x)\dot{\eta}_i(t) \left|U_i(x)\dot{\eta}_i(t)\right| \tag{4-30}$$

Using Equation 4-16 the effect of this damping force on $\ddot{\eta}_i$ is calculated. Note that this results in a constant multiplied with $\dot{\eta}\left|\dot{\eta}\right|$, which can be linearised. This is done by replacing the latter part with $\dot{\eta}_{i-lin}$[7], the velocity around which it is linearised. The same procedure is used for the hydrodynamic damping at the payload in both the PDE and section model. Note that this is a concentrated force, such that the special case of Equation 4-18 is used.

Added Mass

When the payload moves, a certain amount of water is moving along with the payload, which gives similar behaviour as a larger inertia of the payload itself. This phenomenon is modelled by literally adding inertia to the payload, the so called 'added mass' as in for example [6, 9]. The magnitude of this added mass has a strong dependency on the shape and vertical projected area of the payload. For some simple shapes the added mass factor is given in [9]. This added mass has to be added to the payload's inertia in both cable models, which will change it's natural frequencies. Note that the added mass does not affect the gravitational and buoyancy forces acting on the payload.

4-4 Comparison between the PDE and Section Model

Both cable models are compared to determine whether or not the models result in comparable dynamics and which one is the best to use for simulations and control design. Both models

---

[6] Note that this formula depends on the Reynolds number of the fluid. The given formula assumes a turbulent flow

[7] This linearised $\dot{\eta}$ should be the average absolute value of $\dot{\eta}(t)$ in a (preferably non-linear) simulation to get a realistic linearising point.

have the same inputs and outputs, and are implemented in the 'System Model' as presented in Figure 3-2. The frequency response from v_{cont} to F_c is depicted in Figure 4-7. This transfer function is chosen as the resonant frequencies are clearly visible in phase and magnitude, and this transfer is also used in control. As can be seen, the first resonant frequency (the peak in magnitude on the left) is predicted equally by both models, both in magnitude and phase. The other natural frequencies are a lot more damped by the Section Model than the PDE as can be seen by the decreasing peakedness of the magnitude and levelling out of the phase at high frequencies.

This difference in damping of higher frequencies is caused by the material damping term ζ. When $\zeta = 0$, the magnitude and phase of the calculated natural frequencies are very similar for both models. The only large difference is that the highest natural frequencies itself are calculated to be lower by the Section Model. The first and most significant[8] natural frequencies are however practically identical.
When the material damping is neglected, both hydrodynamic damping sources have the same effect on the frequency response resulting from both models. This emphasises that the hydrodynamic damping implementation can be trusted for both models[9].

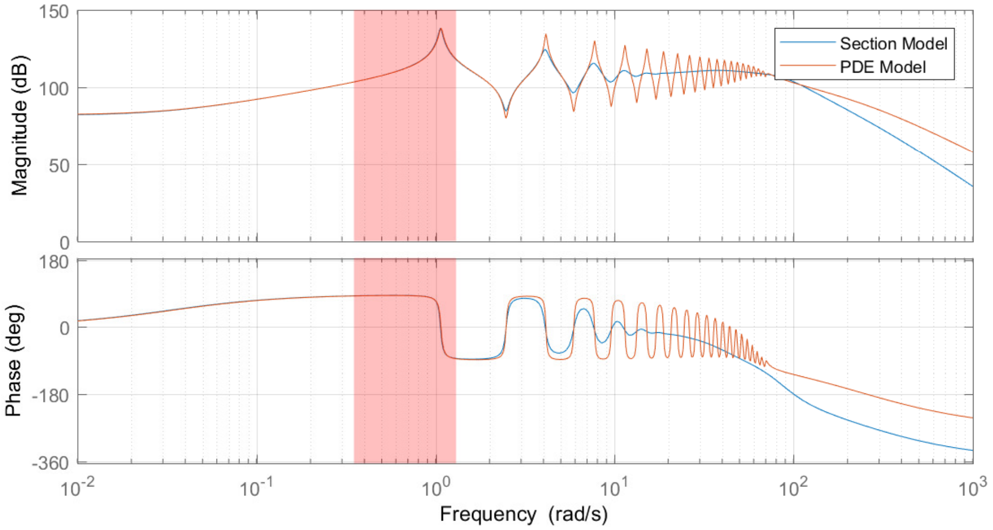

Figure 4-7: Bode of the System Model with the Section and PDE cable model from v_{cont} to F_c. The section model in this plot is composed of 20 cable sections and the PDE model has 20 modes such both models are comparable. Both cables are $3000\,\mathrm{m}$ long and the payloads mass is $175\,000\,\mathrm{kg}$. It can be seen that the first eigenfrequency is the same for both models, for higher frequencies the section model is significantly more dampened than the PDE model. This bode is a result with all damping sources, namely material damping and (linearised) hydrodynamic damping

The large damping in the Section Model by ζ at high frequencies is caused by the calculation

---

[8] The lowest resonant frequencies are the most significant ones as these are the closest to the frequencies contained in the heaves.

[9] Although it verifies that hydrodynamic damping has coherent influence on these models, the damping coefficients d_{c-w} and d_{p-w} can not be verified by this method.

of the damping at the most significant resonant frequency as described in Section 4-3. Each frequency which is higher than the first natural frequency is dampened more than the selected ζ. When any higher frequency would be taken to calculate the damping with, the first natural frequency is less dampened than required such that the material damping cannot be implemented realistically in the Section Model.
When adding sections or equivalently modes to the models, the predicted resonant frequencies shift a little, especially the highest frequencies[10]. For the PDE Model, the eigenfrequencies become lower when more modes are added, while for Section Model the predicts higher natural frequencies when more sections are added. This explains why the Section Model predicts lower eigenfrequencies than the PDE Model. This shift in eigenfrequencies is the smallest for the PDE Model, such that these frequencies are assumed to be the most reliable.

Concluding, the PDE and Section Model are coherent in the first eigenfrequency, but have differences in the material damping and the higher frequencies. With both differences, the PDE Model is chosen as the most reliable, which favours the use of this model. Furthermore, due to the smaller damping of the PDE with respect to the Section Model, the PDE Model is the 'worst case scenario' of these two when it comes to control the cable, such that this model is also the safest choice to use.

The required amount of modes is based on the use of the PDE Model. In Figure 4-7 it can be seen that the magnitude and phase drops at around 60 rad/s, which is caused by the actuator. For each cable length and payload mass this frequency is the same. When the number of modes is too small, the last natural frequency is below this value, which causes an parasitic peak in the magnitude. When for example only 5 modes are incorporated, this peak has about the same magnitude of the first eigenfrequency for a cable of 3000 m and a 175×10^3 kg payload. About 20 modes are required with this mass and length, such that this phenomenon does not occur.
When the cable is shorter and/or the payload is lighter, the eigenfrequencies become higher, such that less modes are required to get past the 60 rad/s. Shorter cables could therefore use less modes, although the modes above this frequency are more significant with short cables than with long cables (which can be seen in Figure 6-5), such that especially the phase influences what can be achieved with control. Therefore it is not recommended to use less modes for the cable model.

4-5 Conclusion on Modelling of the Cable and Payload

The cable dynamics are very important in HC in deep sea, as the cable and payload may oscillate in multiple resonant frequencies. This can be seen in the frequency response depicted in Figure 4-7 which shows that in the force measurement a lot of resonant frequencies have significant amplitudes. In non-linear simulations which are depicted later on in this Thesis, indeed multiple natural frequencies can be seen in for example the payload motion. As

---

[10] For example, the tenth natural frequency is predicted slightly different when the PDE or Section Model contain for example 20 or 30 modes/sections

multiple natural frequencies affect the payload motion and for example force measurements, the cable model cannot do without, which validates the need for an elaborated cable model. This is in contrast to cable models found in literature on HC, which usually models the cable with only one spring and damper, which turns out not to be adequate to model the cable realistically.

The cable model is elaborated in this Chapter by comparing two modelling techniques, namely dividing the continuous cable in small sections and modelling using the PDE framework. As the cable is this important and no measurement data is available to compare the cable dynamics with, the two separate cable models are constructed such that they validate each others order of magnitude of the to be expected payload motion. Both models are compared with the same damping sources while being connected to the System Model as introduced in Chapter 3. It follows that the Section Model is over-damped at high frequencies due to the material damping, while hydrodynamic damping of the cable and the payload affect the frequency response similarly for both models. Together with a minor mismatch in the exact frequency at which the resonances are calculated for both models, the PDE is chosen as the most accurate and realistic model.

Chapter 5

Control Design and Test Case

The controller has to steer the heave compensation cylinder such that the payload motion and force variations are minimised. Without control, the payload's motion is larger than the heaving ship with a cable length of 3000 m and a payload mass of 175×10^3 kg as elaborated in Section 5-2.
In this Chapter, controllers are designed for use with the cable length of 3000 m and a payload mass of 175×10^3 kg. These controllers are compared under the same test cases using the performance indicators as described in Section 5-1. A benchmark controller is defined in Section 5-2, which is compared to the case of no control under the specified test cases. All other controllers designed in this Chapter are compared to this benchmark controller.
In this Chapter, the controllers are designed and simulated for one test case, with ideal measurements without noise and delays. In Chapter 6 the best controllers are evaluated with other cable lengths, payload masses, noise and delays.

5-1 Test Case and Performance Indicators

The controllers have to be compared under the same conditions, which are the test cases. Furthermore, a performance indicator is set up to compare different controllers with each other. First the test cases are defined, which involves two types of disturbances:

- heave motion of the ship
- impulse-like force on the payload (F_{load})

The heave motion is trivial, as the main purpose of a Heave Compensation (HC) system is to compensate the heave motion. This disturbance is measured by the Inertial Measurement Unit (IMU) and is available for control. The force on the payload is used to simulate un-modelled and un-measured disturbances. This disturbance on F_{load} is modelled as a force as large as the payload's inertia, which is suddenly applied, and lasts for 1 second[1]. Due to the sudden start and end, a wide range of frequencies is contained in this disturbance, comparable with an impulse response[2]. As can be seen in this Thesis, the resulting motion of the payload due to this force depends largely on the controller.

The heave motion used for simulation is generated with the MATLAB-toolbox Marine Systems Simulator (MSS) from [10]. Using this toolbox, the movement of a benchmark-ship is simulated as a result from a range of sea states using the JONSWAP spectrum. The ship is a supply vessel of 82.80 m and 6.4×10^6 kg, which can be found in the documentation of MSS. The crane tip is assumed to be located all the way at the back of the ship on starboard side. Using the translations and rotations from this simulation, the vertical motion of the crane tip is calculated and used as heave motion in simulations. For a Significant Wave Height (SWH)[3] of 1, 4 and 7 m, the frequencies contained in this motion is visualised.
Note that this ship is relatively small and light with respect to the cable length of 3000 m and a payload mass of 175×10^3 kg, but as the small weight should result in larger heave motion, this could be seen as a 'worst case scenario'.

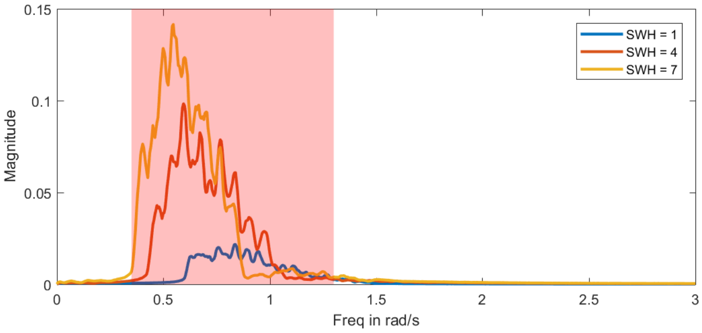

Figure 5-1: Frequencies contained in the heave sequences with SWH's of 1, 4 and 7 m, as generated using MSS [10]. The red band visualises the most significant frequencies and is also shown in other bode plots.

In order to be able to compare the different controllers under the same conditions, the parameters used for bode plots and simulations are presented in Table 5-1. These parameters are used in the simulation, unless specified otherwise. Furthermore, each simulation is performed with the same disturbances, namely a SWH of 4 m and a force-disturbance on the payload, applied at time $t = 5$ s.

The performance of the controller has to be quantised using a performance indicator in order to compare different control strategies or tuning parameters. Historically the main purpose of HC was to avoid slack wire, and thus reduce force variations in the cable. It is however also desired to minimize the payload motion, so in a lot of papers the deviation of the payload's

---

[1] Neglecting the inertia of the cable and (hydrodynamic) damping, this would result in a payload velocity of 1 m/s

[2] A real impulse response results in numerical issues in simulations.

[3] The SWH is the average vertical distance between peak to peak (=crest to through) of the highest third of the waves

Table 5-1: Standard parameters used for bode plots and simulations

Parameter	**Description**	**Value**	**Unit**
l_c	cable length (un-stretched)	3000	[m]
M_P	dry mass of the payload	175×10^3	[kg]
SWH	Significant Wave Height	4	[m]
n	number of modes in the cable model	20	

position is taken as a measure of performance as for instance in [6]. In light of softly landing a payload on the seabed, it is however more important to minimize the variation in the payload's velocity. In light of these different visions, the indicator is desired to increase for the following cases, where a larger value is considered as 'worse':

- velocity of the payload
- position deviations of the payload
- force variations (performance point at the top of the cable)

The velocity has to be minimized in order to keep the payload as stationary as possible[4]. The position deviation measure has a larger penalty for low frequency movement, like heave motion, and it has a large penalty on position drifting, which cannot be handled by a heave compensation cylinder[5]. The force variation has to be minimized to increase the lifetime of the cable, along with decreasing the chance of slack wire and snap loading.

The performance indicator is set up using *rms* values of the velocities, positions and forces from simulations, using the following formulas:

$$rms_{\dot{x}_{load}} = \sqrt{1/N \sum_{n=1}^{N} |\dot{x}_{load} - \text{mean}(\dot{x}_{load})|^2} \tag{5-1}$$

$$rms_{x_{load}} = \sqrt{1/N \sum_{n=1}^{N} |x_{load} - \text{mean}(x_{load})|^2} \tag{5-2}$$

$$rms_{F_c} = \sqrt{1/N \sum_{n=1}^{N} |F_c - -\text{mean}(F_c)|^2} \tag{5-3}$$

With:

x_{load}	=	position of the payload	[m]
F_c	=	force at the top of the cable	[N]
F_{mean}	=	the mean of F_c	[N]
N	=	number of measurements of the variable	

---

[4] Minimising the payload velocity is important for e.g. minimizing fluctuating hydrodynamic forces for fragile payload or minimising the impact when lowering the payload on the sea bed

[5] The heave compensation cylinder cannot handle drifting as it woudl drive the cylinder to the end of their maximum stroke.

These different rms-values could be combined in a single performance indicator using a weighted sum, which is not done in this Thesis such that the specific benefits of different control strategies can be indicated. In addition to the rms-values, visual inspection of the simulation results is an important way to indicate how well the controller performs.

5-2 Control Structure and Benchmark

As defined in Figure 3-2, there is only one controllable input (v_{cont}). This variable controls the oil flow to and from the heave compensation cylinder as modelled in Section 3-1. As outputs, the measurements of F_c, $\dot{x}_{act}$ and $\dot{x}_{IMU}$ are available, along with x_{act} and x_{IMU}. In this Chapter these variables are assumed to be perfectly measured.

Minimal (linear) stability margins are defined to enforce a minimum level of robustness on all controllers. This is the Gain Margin (GM) and Phase Margin (PM) which are determined from Nyquist plots. Additionally a maximum bandwidth is defined such that the designed controllers should be able to be implemented in real world HC systems. These limits are defined as:

minimum GM	6 dB
minimum PM	45°
maximum bandwidth	20 rad/s

These GM and PM are known to generate a medium level of robustness for most control purposes. The maximum bandwidth is an educated guess of the maximum bandwidth of HC systems.

In order to not violate this bandwidth requirement without deteriorating the performance too much, $\dot{x}_{act}$, $\dot{x}_{IMU}$ and F_{sens} are filtered by low pass-filters. The signals $\dot{x}_{act}$ and $\dot{x}_{IMU}$ are filtered by a second order low pass-filter with a cut-off frequency of 100 rad/s, F_{sens} with two low pass-filters in series with cut-off frequencies of 10 and 100 rad/s[6]. In formula these low pass filters are denoted as:

$$lp_v = \frac{1}{\frac{s^2}{100^2} + 2\frac{s}{100} + 1} \tag{5-4}$$

$$lp_F = \frac{1}{\left(\frac{s}{10} + 1\right)\left(\frac{s}{100} + 1\right)} \tag{5-5}$$

With:

lp_v = low pass-filter on $\dot{x}_{act}$ and $\dot{x}_{IMU}$

lp_F = low pass-filter on F_{sens}

---

[6] The low pass-filter on $\dot{x}_{IMU}$ is primarily used to reject noise in the to be designed feedforward law, and the second low pass-filter on F_{sens} is used to further reject noise. Therefore the cut-off frequency is higher than the maximum bandwidth.

The control type is chosen to be PID as this is not model based, which would be cumbersome with the required amount of modes in the cable as the linearised model comprises of 46 states. Additionally, model based control would require detailed knowledge of the system, like the submerged mass and dimensions of the payload (added mass and damping). This is not desired in practice such that a PID is more convenient.

In this Thesis only P and PI controllers are used (with or without additional filters), but for generality the controllers are also called PID as a general term. The used PID formula is written in the parallel form:

$$K_P\left(1+\frac{1}{\tau_I s}\right) \tag{5-6}$$

With:
K_P = proportional PID gain
τ_I = integral time constant [s]

The standard K_I is calculated as $\frac{K_P}{\tau_I}$. This form is chosen as it makes clear at which frequency the pole of the integral action is located, namely at $\omega = \frac{1}{\tau_I}$ [rad/s]. For each controller the K_P and τ_I will be given.

All controllers which are discussed in this Thesis are assisted by a feedforward part to directly counteract the heave motion. From Equation 3-1 it follows that $\dot{x}_{act} = \dot{x}_{heave}$ is required to achieve this. This results in the following feedforward law with low pass-filter:

$$v_{cont_{FF}} = 1 \cdot \dot{x}_{IMU} \cdot lp_v \tag{5-7}$$

With:
x_c = Position of the top of the cable model in the earth frame [m]
x_{act} = position of the actuator [m]
x_{IMU} = measurement of the heave motion by the IMU [m]
$v_{cont_{FF}}$ = feedforward control signal [m/s]

This feedforward law is often used in HC to assist the feedback controller, or it can even be the only control form which is utilized. Therefore the benchmark controller is taken as a pure feedforward on the measured heave velocity. Simulations without control and with the benchmark controller is depicted in Figure 5-2. It can be seen that the feedforward achieves a large improvement with respect to no control. It can be seen in this simulation that x_c has larger amplitudes than x_{heave}, which can be explained by the limited stiffness of the actuator. The performance indicators for both simulations are:

Perfomance indicator: benchmark		
$rms_{\dot{x}_{load}}$	0.242	[m/s]
$rms_{x_{load}}$	0.27	[m]
rms_{F_c}	7.09×10^4	[N]
$\dot{x}_{load-max}$	0.52	[m/s]

Perfomance indicator: no control		
$rms_{\dot{x}_{load}}$	1.73	[m/s]
$rms_{x_{load}}$	2.88	[m]
rms_{F_c}	4.81×10^5	[N]
$\dot{x}_{load-max}$	3.6	[m/s]

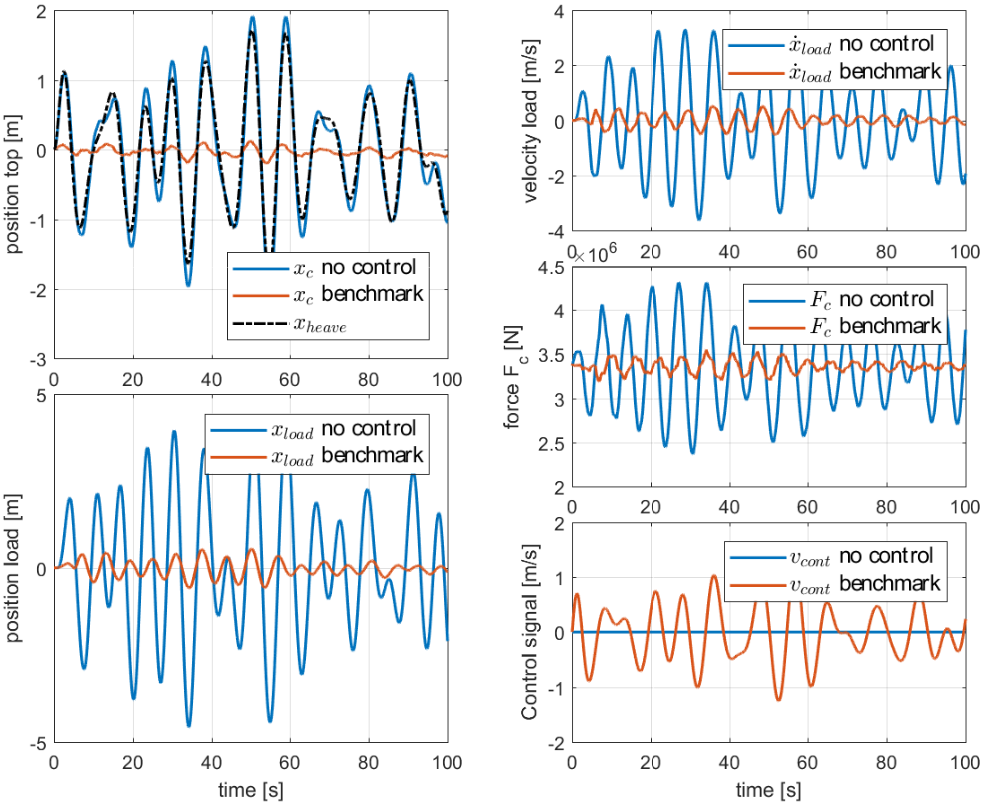

Figure 5-2: Simulation results without control and with benchmark control under disturbances from F_{load} and heave. As can be seen, the benchmark controller clearly results in better performance with respect to no control. Without controller, x_c has even higher amplitudes than x_{heave} itself.

5-3 PID on the top velocity of the cable

PID control on the velocity of the top of the cable, of which the control structure is shown in Figure 5-3, is a common control strategy for HC [2]. It directly aims to minimise motion of the top of the cable (as $x_c = x_{heave} - x_{act}$), which should result in an as small as possible payload motion. To be specific, this PID controller aims to make $\dot{x}_{act}$ follow $\dot{x}_{IMU}$ such that $\dot{x}_c$ is minimised.

What can be achieved with a PID on $\dot{x}_c$ is investigated using the frequency response from v_{cont} to $\dot{x}_{act}$, which is called the 'Plant' for the PID on the top velocity. The bode plot of the Plant is depicted in Figure 5-4 using the parameters from Table 5-1. The bode plot reveals several properties of the plant, of which the most important are elaborated here. The pole pairs (peaks in magnitude) are very close with their accompanying zero pairs (dips in magnitude), which is why the phase does not converge to $-180°$ after each pole pair. This is caused by the active cylinder, which is relatively stiff as the oil is 'trapped' in this cylinder. As a result, the poles are practically cancelled by the zeros such that $\dot{x}_c$ is barely affected by a resonating cable and payload. This is convenient when trying to keep the top of the cable x_c as static

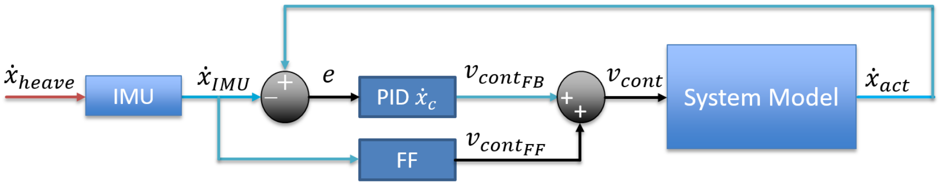

Figure 5-3: Block scheme of a PID acting on the top velocity of the cable. The blue signal $v_{cont_{FB}}$ is the control signal of the controller. The blue signals $\dot{x}_{act}$ and $\dot{x}_{IMU}$ are measurements. Note that $\dot{x}_{heave}$ and F_{load} also enter the System Model, which is not depicted here.

as possible, but it is limiting when trying to damp out resonances.

In frequency domain the PI is tuned to reject the heave at $\dot{x}_c$, which boils down to having a gain of > 0 dB in the heave frequency range. This is exactly what is done in the 'PI OL large I' tuning in Figure 5-4. This results in a GM of 12 dB and a PM of 50°, which satisfies the required stability margins. In simulations this controller is however not stable due to differences between the linearised and non-linear model. In order to get the controller also stable in simulations, τ_I is increased until the simulation is stable. This results in the open loop 'PI OL' in Figure 5-4. This stable controller has the following specifications:

PI parameters		*PI specifications*	
K_P	0.1	gain margin	14 dB
τ_I	0.2	phase margin	95°

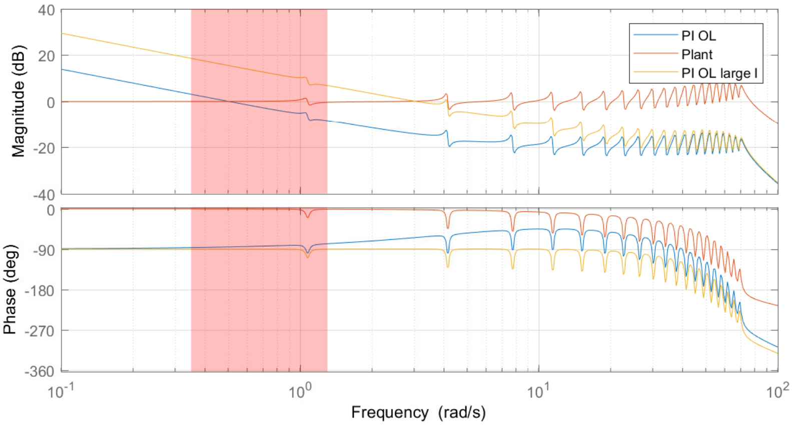

Figure 5-4: Bode plot of the Plant (v_{cont} to $\dot{x}_c$) and open loop with the PID on the top velocity of the cable (e to $\dot{x}_c$). The 'PI OL large I' is tuned better in frequency domain, but is unstable in simulations. The red shaded area is the frequency region where the heave motion is significant.

Simulation results with the stable PI on $\dot{x}_c$ compared to the benchmark is shown in Figure 5-5. Although the the magnitude of $\dot{x}_c$ is comparable to the benchmark controller, x_{load}, $\dot{x}_{load}$ and F_c show that the performance of this controller is significantly worse than with only feedforward (benchmark). This is also visible in the performance indicator, where all indicators have a higher value for the PI than the benchmark. Power Spectral Density (PSD) analysis shows that the cables first (and somewhat less the second) resonant frequency is responsible for this bad performance. A PSD analysis of the 'high I' tuned PI which turned out to be unstable shows that the first eigenfrequency contains somewhat less energy than with the stable PI, but in this case the second mode is dominant. The third and fourth resonant frequencies are also exited in this case. The underlying problem why the PI on $\dot{x}_c$ has such a large payload motion is evaluated in Subsection 5-4-1.

Perfomance indicator: PI on $\dot{x}_c$

$rms_{\dot{x}_{load}}$	0.458	[m/s]
$rms_{x_{load}}$	0.441	[m]
rms_{F_c}	1.38×10^5	[N]
$\dot{x}_{load-max}$	0.82	[m/s]

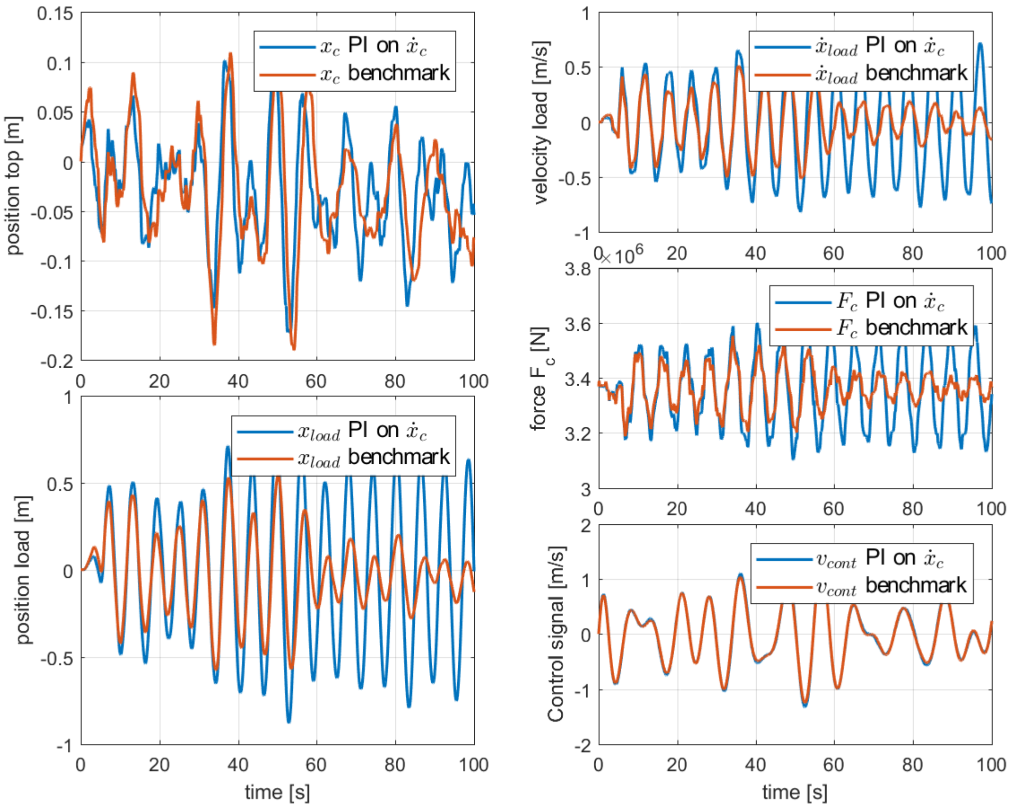

Figure 5-5: Simulation of the PI (with feedforward) on $\dot{x}_c$ and the benchmark controller. The disturbances are heave motion and the disturbance on F_{load}, the simulation parameters are to be found in Table 5-1. No noise.

5-4 PID on the top force of the cable

The second PID which is evaluated is a PID which regulates on F_{sens}, the (in this chapter perfect) measurement of F_c. In industry, this method is sometimes called 'constant tension control', which is also used for lifting a payload through the splash zone. By reducing the tension variations, there is a smaller chance of slack wire, which could cause cable breakage. Furthermore, when F_c is more constant, the cable's tension will also be more smooth at the bottom of the cable, such that the payload receives less force variations. This results in lower accelerations, which is desired when stabilising the payload.

The control structure of the PID on F_c (or equivalently F_{sens}) is depicted in Figure 5-6. F_{des} is the desired force, which has to be equal to the static force due to gravity. In Figure 5-7 the bode plot of the Plant and the chosen PID is depicted. The plant of this controller is defined as the response from v_{cont} to F_{sens}. It can be seen that the peaks in magnitude are significantly higher than the peaks of the PID on $\dot{x}_c$ in Figure 5-4. This implies that these modes can be rejected better than with the PID on $\dot{x}_c$. These resonant frequencies are dampened/rejected best when their peaks are as far as possible above 0 dB in open loop, while care has to be taken that the system has a sufficient GM and PM. Additionally the bandwidth should not exceed 20 rad/s as defined. Furthermore it is desirable to have an as large as possible gain in the frequency band where the heave disturbance is expected to complement the feedforward controller on heave rejection. Based on these requirements, the PID is designed as depicted in Figure 5-7, which is in fact only a P controller with the following specifications:

P on F_{sens} specifications	
gain margin	20 dB
phase margin	95°

P on F_{sens} parameters	
K_P	1.1×10^{-6}
τ_I	∞

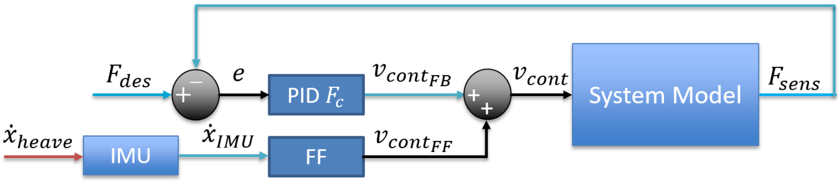

Figure 5-6: Block scheme of a PID controller acting on the measured force at the top of the cable F_{sens} (measurement of F_c). The blue signals F_{des} and v_{cont} are respectively the desired velocity and the control signal of the controller. The blue signals F_{sens} and $\dot{x}_{IMU}$ are measurements.

Simulations of the P on F_{sens} controller compared to the benchmark is depicted in Figure 5-8. The most eye-catching difference is the offset in both x_c and x_{load} for the force feedback controller. This offset is caused by the impulse-like disturbance on F_{load}. When this disturbance force would last, x_{act} drifts away until the actuator's limit is reached such that the heave cannot be compensated any more.

When this offset is neglected, it is clear that the controller on F_{sens} improves the performance a lot with respect to the benchmark controller in both payload motion and force. This is also visible in the performance indicator, which is more than twice as small as with the benchmark, except the maximum value for $\dot{x}_{load}$, which is a result from the disturbance on F_{load}.

Perfomance indicator: P on F_{sens}		
$rms_{\dot{x}_{load}}$	0.0983	[m/s]
$rms_{x_{load}}$	0.124	[m]
rms_{F_c}	2.55×10^4	[N]
$\dot{x}_{load-max}$	0.46	[m/s]

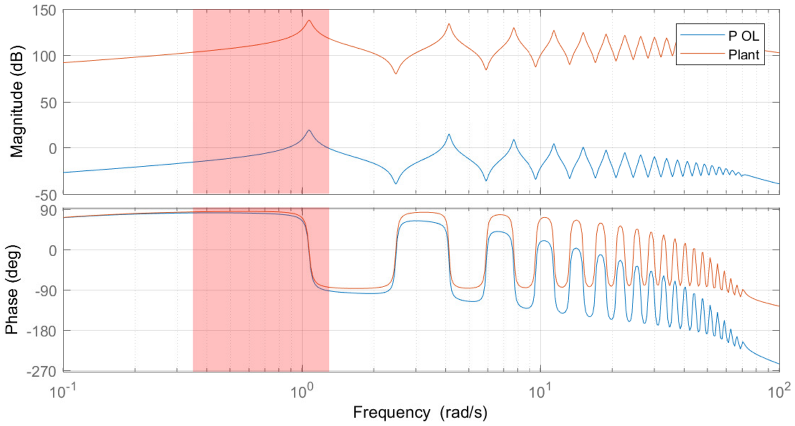

Figure 5-7: Bode of the P (with feedforward) on F_{sens} and the benchmark controller.

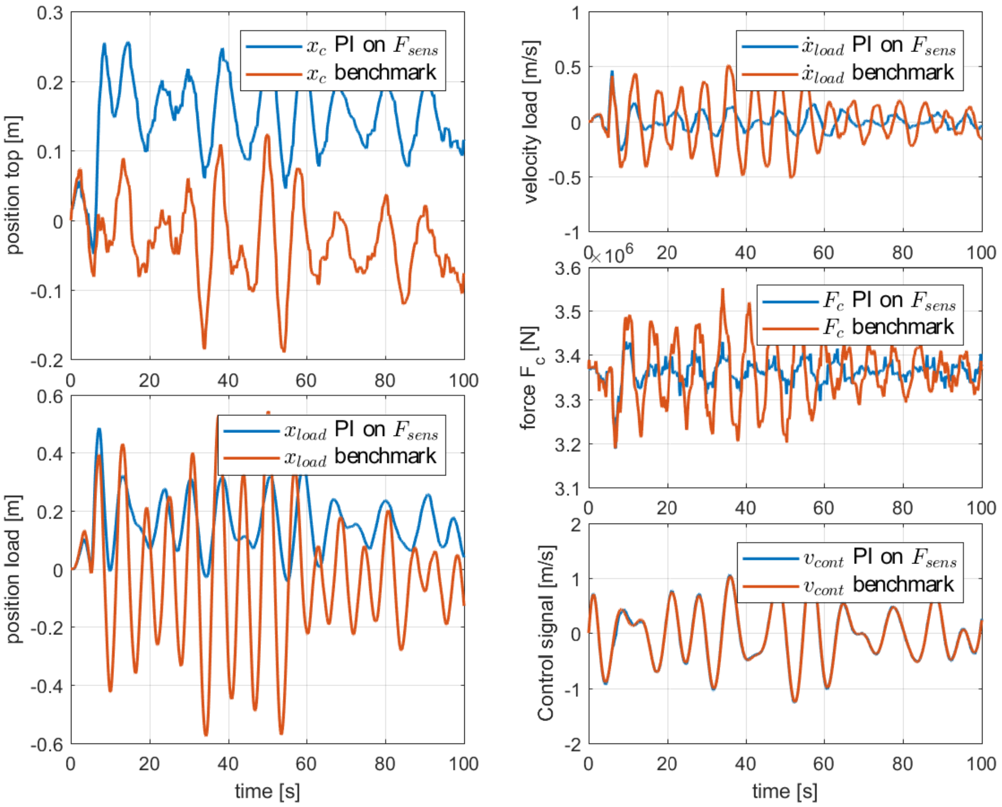

Figure 5-8: Simulation of the PI (with feedforward) on F_{sens} and the benchmark controller. The disturbances are heave motion and the disturbance on F_{load}, the simulation parameters are to be found in Table 5-1

5-4-1 Problems with both the PI on the top velocity and cable force

As can be seen from Figures 5-5 and 5-8, the PI on F_{sens} is superior to the PI on $\dot{x}_c$ when it comes to rejection of the heave. However this P on F_{sens} allows the actuator to drift away when a disturbance on F_{load} is applied, which also happens when F_{des} is not equal to the static load.
The PI on $\dot{x}_c$ on the other hand has less performance than the benchmark controller, but the PI will be more robust in the long term to for example non-linear input relations of the heave compensation cylinder.

In light of the disturbance F_{load}, which is unmeasured, another important aspect is visualised in Figure 5-9. In this figure the response with both PIDs to F_{load} is shown without heave disturbance. The payload dampened is a lot better with the feedback on F_{sens}, as can be seen by the limited oscillation in $\dot{x}_{load}$. This shows that feedback on F_{sens} is effective to damp the payload. It can further be seen that the PI on $\dot{x}_c$ dampens the cable and payload even less than the benchmark (which is equal to no control without heave). This causes the large oscillations such that this PID becomes unstable when the I-action is too large as visualised with the 'high I' simulation. This PI causes negative damping, such that the system becomes unstable.

It is clear to see that drifting problem feedback control on F_{sens} is solved with a low bandwidth position/velocity feedback, like PI on $\dot{x}_c$. When this controller is only active outside the frequency band in which the P on F_{sens} is active, a parallel controller on the velocity can be added without deteriorating the first PID's performance too much.
The problem of the decreased dampening of the payload's motion with the PI on $\dot{x}_c$ is improved by adding damping on the cable and payload's resonant frequencies with a force feedback loop. This is motivated by the high energy of these modes in PSD analysis of the PI on $\dot{x}_c$ and the low amount of damping as in Figure 5-9

5-5 Parallel force-velocity PID

Both proposed solutions in the foregoing section are implemented by use of two separate PIDs in parallel, one acting on F_{sens}, the other on $\dot{x}_c$. The only difference is the tuning, which depends on the philosophy used to tune. To make clear which philosophy is used, the controllers are named as following:

P-PI F_{sens}; Parallel controller with the focus on F_{sens} (P), with added tracking from $\dot{x}_c$ (PI)

PI-P $\dot{x}_c$; Parallel controller with the focus on $\dot{x}_c$ (PI), with added damping from F_{sens} (P)

The first implementation is basically a force feedback controller with added low frequency tracking as described in Subsection 5-5-1. The second is a velocity feedback loop, with added damping on the cable and payload as described in Subsection 5-5-2.
Both of these are implemented in the structure of Figure 5-10.

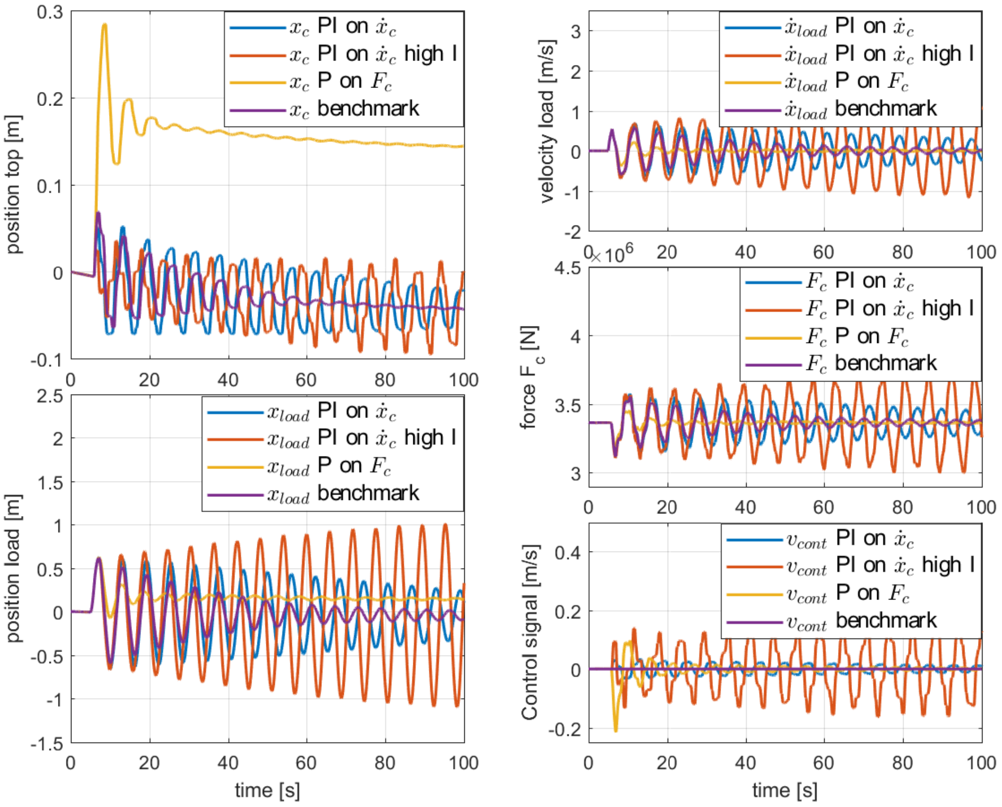

Figure 5-9: Simulation of the PI (with feedforward) on $\dot{x}_c$ with the stable and unstable controller, P control on F_{sens} and the benchmark controller. As disturbance only the disturbance on F_{load} is taken. It can clearly be seen that the P on F_{sens} dampens the payload the fastest, followed by the benchmark controller. The PI on $\dot{x}_c$ is less dampened than the benchmark, especially for the 'high I' tuning, which is unstable.

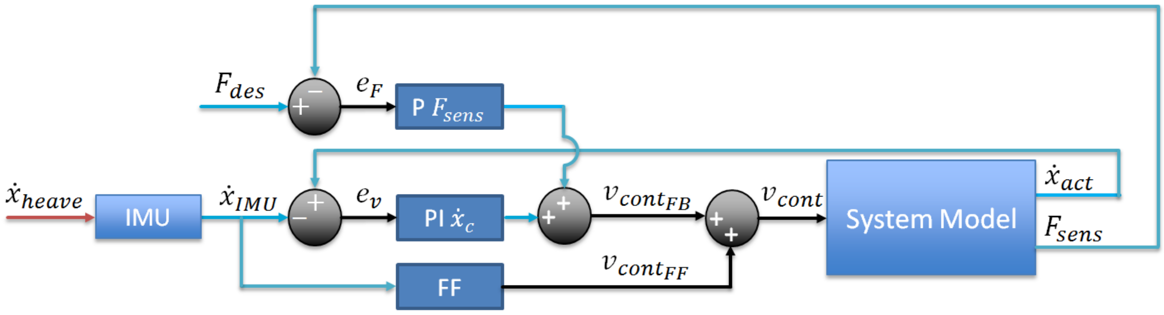

Figure 5-10: Block scheme of a parallel PID on the top position and force of the cable. The blue lines indicate either controllable entities or measurements. Note that $\dot{x}_{heave}$ and F_{load} also enter the System Model, which is not depicted here.

The resulting parallel framework is similar to the one presented in [11], which includes a combination of position control with added force control. In this paper, non-linear model-

based control is utilized to control a winch (instead of the heave compensation cylinder) using ideal measurements from the winch and heave to decouple the cable from the ship's heave motion. Parallel to this controller is an 'Integral Force Feedback control law' added, which is similar to the P controller on F_c as used in this Thesis[7]. In this paper an unknown disturbance is applied which shows very comparable results as the disturbance on F_{load}.
Following from the simulations, the payload's position stays within a band of 0.02 m while the ship heaves as much as 4 m. The cable model is however a single spring, of which the mass is partially included in the payload and therefore only models the first resonance mode. This allows for very fast control, which results in the aforementioned performance. Also no coulomb friction is inserted which simplifies control also a lot.

5-5-1 Parallel PID with a focus on Force control (P-PI F_{sens})

As starting point for the P-PI F_{sens}, the single controller on F_{sens} is taken. The low bandwidth velocity feedback is constructed with a bandwidth of 0.05 rad/s such that it does not influence the performance of the force loop. As the controller is not active (i.e. a gain of $>$ 0 dB) in the entire heave frequency band, the gain is locally increased where the plant has low gain. This is done with an inverted notch filter, acting on the lower frequencies of the heave frequency band. This is tuned such that it adds enough gain to get the open loop gain above 0 dB, but takes care that the phase lead before, and lag after the inverted notch is not too large. This results in the 'PI OL' bode as depicted in Figure 5-11. Comparison of the 'Plant OL' and 'PI OL' in the red shaded band clearly shows the effect of the inverted notch, it adds gain around 0.4 rad/s. It also adds phase below this frequency, such that the phase approaches 180° which limits due to the PM requirement. The design of this controller is limited by the maximum bandwidth specification and the GM at the leftmost 0 dB crossing.

A second controller is constructed which has a higher gain in the heave frequency band, denoted as 'PI OL notch' in Figure 5-11. This controller uses two notch filters[8] to filter away the second and third natural frequencies. Additionally a low pass-filter is used to suppress higher modes such that the phase lag of the notches and low pass-filter does not render the system unstable. This allows the controller to have a higher K_P gain based on the maximum bandwidth. The resulting PM of this tuning is however only 40°, which violates the demand on PM. As the PM is still close to 45° and it is in low frequency[9], this is allowed for now.
The effect of the force feedback is clearly visible in Figure 5-12 by comparing the magnitude in the heave frequency region of 'Plant OL' with the original plant. The low gain of the plant indicates that the force feedback is active at these frequencies, which practically means that these are dampened. The controllers specifications are as follows:

---

[7] The reason that integral force feedback is similar to a proportional force feedback is due to a difference in control variable (position in [11], velocity in this Thesis)

[8] also known as 'band stop filters'

[9] A PM of 40° at low frequencies is more robust to control delays than the same PM at a high frequency

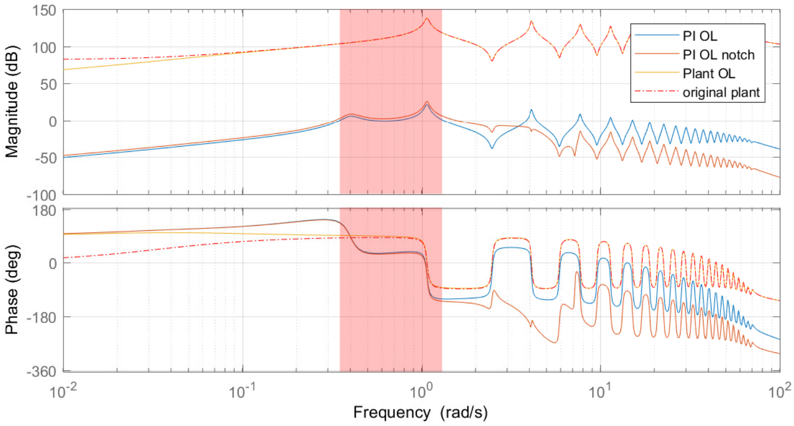

Figure 5-11: Bode force loop parallel controller with focus on force (P-PI F_{sens}) from e_F to F_{sens}, along with the plants from v_{cont} to F_{sens} with ('PI OL') and without ('original plant') the velocity feedback in the loop.

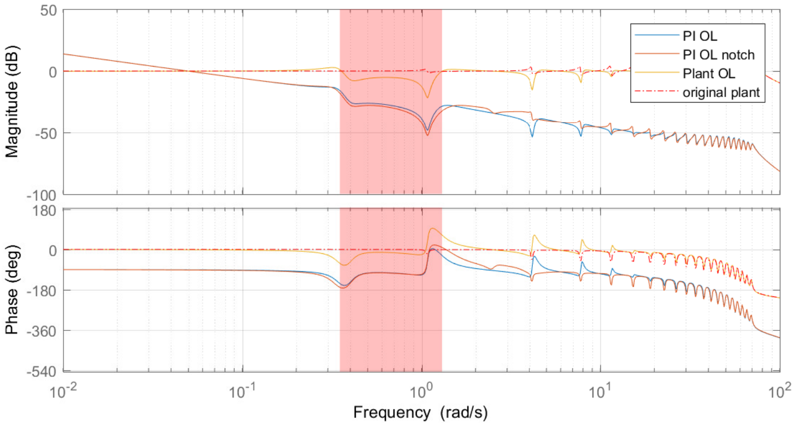

Figure 5-12: Bode velocity loop of the parallel controller with focus on force (PI-P $\dot{x}_c$) from e_v to $\dot{x}_c$, along with the plants from v_{cont} to $\dot{x}_c$ with ('PI OL') and without ('original plant') the force feedback (without notch) in the loop.

P-PI F_{sens}

force loop parameters

K_P	1.1×10^{-6}
τ_I	∞

velocity loop parameters

K_P	1×10^{-5}
τ_I	2×10^{-4}

force loop specifications

gain margin	20 dB
phase margin	45°

velocity loop specifications

gain margin	51 dB
phase margin	88°

P-PI F_{sens} with notch

force loop parameters

K_P	1.5×10^{-6}
τ_I	∞

velocity loop parameters

K_P	1×10^{-5}
τ_I	2×10^{-4}

force loop specifications

gain margin	9 dB
phase margin	40°

velocity loop specifications

gain margin	49 dB
phase margin	88°

Simulation results of both controllers compared to the benchmark can be seen in Figure 5-13. The initial offset of x_c due to the disturbance on F_{load} is larger for the P-PI F_{sens} controllers compared with the P on F_{sens} in Figure 5-8. This is caused by the additional gain from the inverted notch in the force feedback loop, but as the velocity feedback steers the system back to $x_c \approx 0$, this causes no harm. The offset however does influence the rms-performance indicator of especially x_{load}.

The PID without notch performs best on each performance indicator. This performance is comparable to the standalone PID on F_{sens}, with a better performance on $\dot{x}_{load}$ and F_c, but a slight decrease on x_{load}. This last difference is caused by the calculation method of the rms-value by subtracting the mean of the signal (Equation 5-2). The P-PI F_{sens} with notch has a worse performance indicator than without notch, but simulations without the force disturbance and only heave show that this controller performs better on x_{load}, but this suffers from a low damping on higher frequencies, causing a decreased performance on both $\dot{x}_{load}$ and F_c. PSD analysis shows that this is mainly due to the second resonant frequency, which is one the frequencies which is notched away. When comparing both P-PI F_{sens}'s on $\dot{x}_{load}$ and x_{load} in time domain with the P on F_{sens}, the payload moves less with the P-PI F_{sens}'s with inverted notch.

Perfomance indicator:	*P-PI F_{sens}*	
$rms_{\dot{x}_{load}}$	0.093	[m/s]
$rms_{x_{load}}$	0.137	[m]
rms_{F_c}	2.22×10^4	[N]
$\dot{x}_{load-max}$	0.51	[m/s]

Perfomance indicator:	*P-PI F_{sens} with notch*	
$rms_{\dot{x}_{load}}$	0.11	[m/s]
$rms_{x_{load}}$	0.153	[m]
rms_{F_c}	3.01×10^4	[N]
$\dot{x}_{load-max}$	0.53	[m/s]

Concluding, the parallel controllers with a focus on force feedback are more successful in minimising the payload's motion with respect to the standalone force feedback. Out of these two, the controller without notch filters has better performance compared to the other. As this is also the most simple controller (it does not require the frequency of the second and third resonant frequency to notch away), the P-PI F_{sens} without notch is preferred.

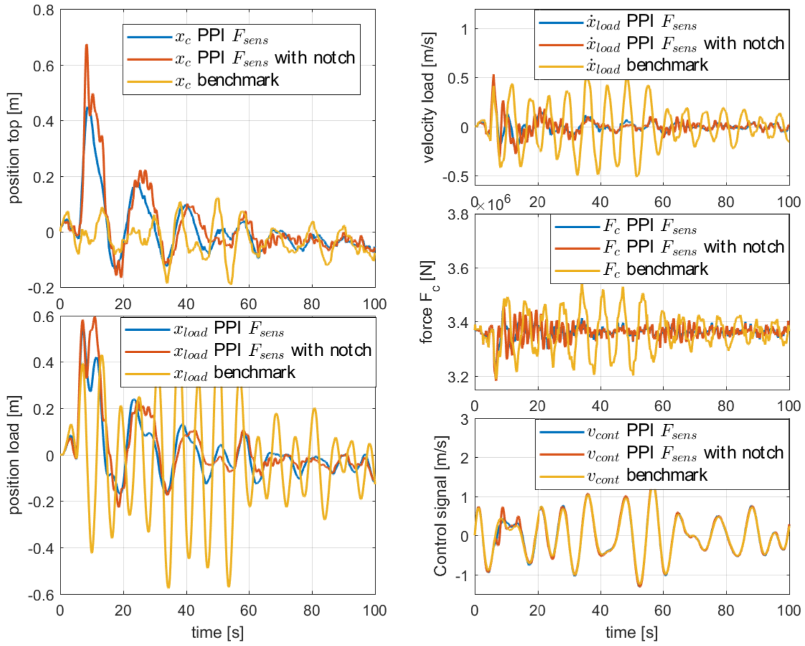

Figure 5-13: Simulation P-PI F_{sens} with and without notch filter, compared to the benchmark controller under the influence of heave and disturbance on F_{load}. Both P-PI F_{sens}'s are very similar and are able to damp out the payload's motion due to the disturbance on F_{load}.

5-5-2 Parallel PID with a focus on velocity control (PI-P $\dot{x}_c$)

The P-PI F_{sens} is designed as a velocity-based controller with added damping from the force feedback. As described in Section 5-3, the PID on $\dot{x}_c$ on itself is unable to decrease the payload motion compared to the benchmark controller. This because of the decreased damping on the cable's resonance frequencies by this controller as visible in Figure 5-9.

The force feedback is taken equal as the P controller designed in Section 5-4, as it has maximum gain on the resonant frequencies, while respecting the limits of the maximum bandwidth. Note that this has the same gain as the P-PI F_{sens}, but without the inverted notch. The velocity feedback is designed with a bandwidth of $\approx 3\,\text{rad/s}$ such that the entire heave region is covered. In Figure 5-14 it can be seen that the positive gain of the force feedback (Figure 5-15) creates a dip in magnitude of the 'Plant OL' at the first resonance frequency, such that the velocity feedback is not active here. This leaves room for the force feedback to damp the cable at this frequency. The phase of 'P OL' at $\approx 1\,\text{rad/s}$ is however close to 180°, which results in a too low PM on both the force and velocity feedback. By adding phase around the heave frequency band with a lead-lag filter, the PM is well within the limits as visible in Figure 5-14 ('PI OL lead lag'). The lead-lag filter has a pole at $1.3\,\text{rad/s}$ (the highest frequency in the heave band) and a zero at $0.1\,\text{rad/s}$:

$$filter = \frac{s + 0.1}{s + 1.3} \tag{5-8}$$

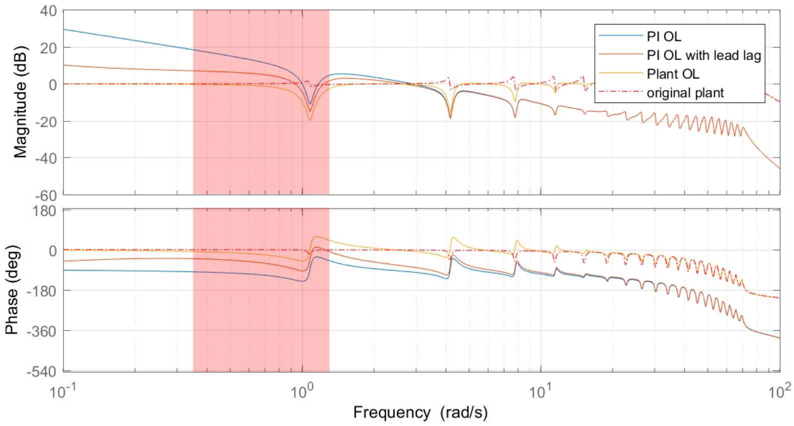

Figure 5-14: Bode velocity loop parallel controller with focus on velocity (PI-P $\dot{x}_c$) from e_v to $\dot{x}_c$ with and without lead lag filter, along with the plants from v_{cont} to $\dot{x}_c$ with ('PI OL') and without ('original plant') the force feedback (without lead lag filter) in the loop.

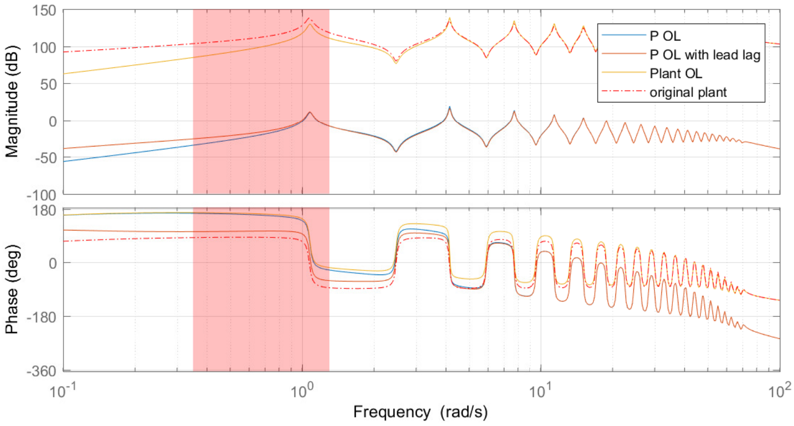

Figure 5-15: Bode force loop parallel controller with focus on velocity (PI-P $\dot{x}_c$) from e_F to F_{sens} with and without lead lag filter, along with the plants from v_{cont} to F_{sens} with ('PI OL') and without ('original plant') the velocity feedback (without lead lag filter) in the loop.

As this filter has gain = 1 for high frequencies, the crossover frequency is approximately the same with and without the lead-lag filter. The final specifications of the PIDs are as follows:

PI-P $\dot{x}_c$		**PI-P $\dot{x}_c$ with lead-lag**	
force loop parameters		*force loop parameters*	
K_P	1.1×10^{-6}	K_P	1.1×10^{-6}
τ_I	∞	τ_I	∞
velocity loop parameters		*velocity loop parameters*	
K_P	6×10^{-4}	K_P	6×10^{-4}
τ_I	2×10^{-4}	τ_I	2×10^{-4}
force loop specifications		*force loop specifications*	
gain margin	19 dB	gain margin	19 dB
phase margin	43°	phase margin	85°
velocity loop specifications		*velocity loop specifications*	
gain margin	16 dB	gain margin	16 dB
phase margin	38°	phase margin	92°

Simulations with both controllers show that the PI-P $\dot{x}_c$ with lead-lag filter outperforms the one without filter when it comes to damping of the payload's motion as shown in Figure 5-16. This is verified with a simulation without heave, but this also points out that the payload is damped second best by the benchmark controller. This is already a significant improvement to the single PI on $\dot{x}_c$, which is unstable at such a bandwidth.

It may be clear that the PI-P $\dot{x}_c$ version with lead-lag performs best. This is also the result of the performance indicator as the performance on $\dot{x}_{load}$, x_{load} and F_c is approximately twice as small as those of the benchmark controller. Only the maximum value of $\dot{x}_{load}$ is a little lower for the benchmark, but as this is only a single peak (see Figure 5-16), this indicator is misleading.

Perfomance indicator: PI-P $\dot{x}_c$			*Perfomance indicator: PI-P $\dot{x}_c$ with lead-lag*		
$rms_{\dot{x}_{load}}$	0.227	[m/s]	$rms_{\dot{x}_{load}}$	0.124	[m/s]
$rms_{x_{load}}$	0.224	[m]	$rms_{x_{load}}$	0.126	[m]
rms_{F_c}	6.94×10^4	[N]	rms_{F_c}	3.84×10^4	[N]
$\dot{x}_{load-max}$	0.59	[m/s]	$\dot{x}_{load-max}$	0.53	[m/s]

5-6 Conclusion on Control Design on one working point and ideal conditions

In this Chapter, controllers are designed with the conditions as defined in Table 5-1, like a cable length of 3000 m and a payload mass of 175×10^3 kg. Even though the non-linear simulations are performed without noise and delays, some controllers which are designed in frequency domain turn out to be unstable, as can be seen with the PI on $\dot{x}_c$.

The controllers are compared in time domain, *rms*-values calculated from simulations and in some cases PSD analysis. In some cases the performance indicator is misleading, such that a lower *rms*-value is not necessarily an improvement. The tuning of the controllers is also a

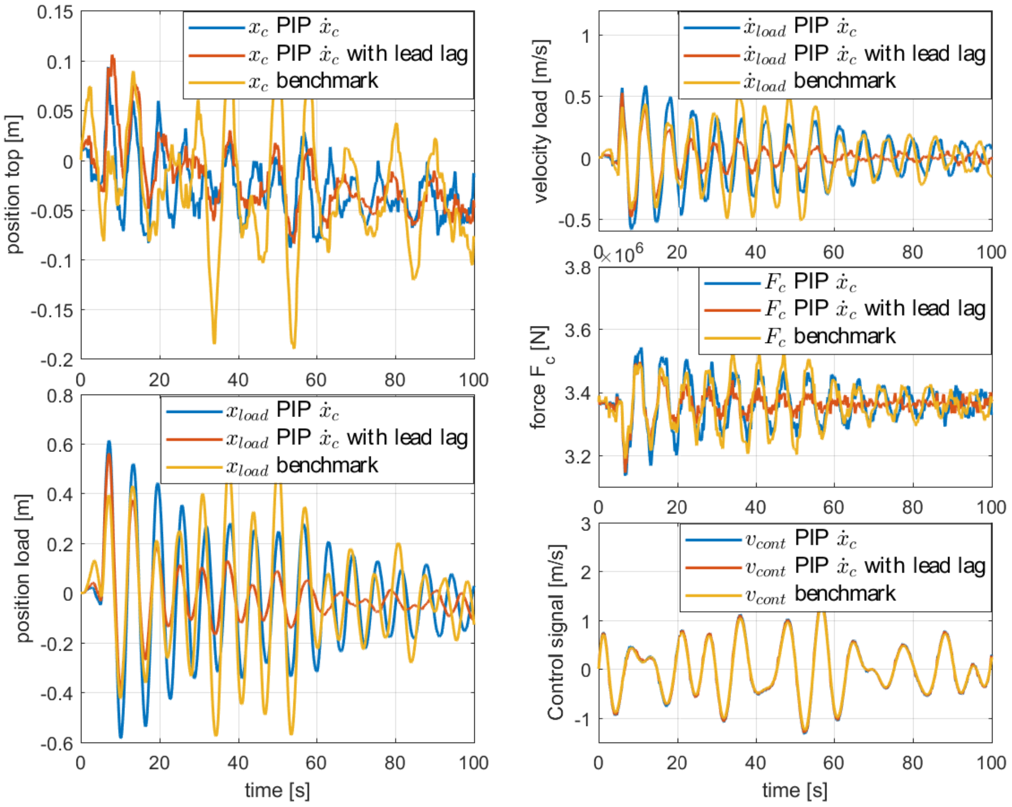

Figure 5-16: Simulation results of parallel controller with focus on velocity (PI-P $\dot{x}_c$) along with the benchmark controller. As can be seen, the PI-P $\dot{x}_c$ with lead lag dampens the payload best after the disturbance on F_{load} while rejecting the heave.

trade-off between rejection of the heave and damping of the payload, which are both important. Therefore the controller's parameters are not optimised using optimisation algorithms, but rather by inspection of time domain and PSD analysis of simulations.

The two best performing controllers, P-PI F_{sens} and PI-P $\dot{x}_c$ with lead lag, are compared to each other using simulation results in Figure 5-17 and PSD analysis in Figure 5-18. The simulation clearly shows that the P-PI F_{sens} adds the most damping to the payload's motion (best visible in $\dot{x}_{load}$), while at the end of the simulation when the disturbance on F_{load} is dampened out, the payload's motion is comparable. PSD analysis shows a large peak in F_c and $\dot{x}_{load}$ at $\approx 1\,\text{rad/s}$ for the PI-P $\dot{x}_c$ which indicates that the controller has a low performance on this frequency. This oscillation is also visible in the time domain. The P-PI F_{sens} on the other hand has a lower performance on $\dot{x}_{load}$ at low frequencies.
Simulations without heave disturbance (not depicted in this Thesis) show that the P-PI F_{sens} performs better at the resonance frequencies of the cable-payload combination. The difference is especially large for the second to fifth resonance frequency, which shows about 2 times lower peaks at those frequencies for F_c and $\dot{x}_{load}$. Especially the force variation is effected at these frequencies. This may not be surprising, as the P-PI F_{sens} is in fact an extension on the force

feedback controller. The P-PI F_{sens} and PI-P $\dot{x}_c$ have the same force feedback law and the effect of the velocity feedback should be diminished at high frequencies, but nevertheless the P-PI F_{sens} has significantly higher performance at these frequencies.

The P-PI F_{sens} is the best performing controller due to it's large damping of the cable and payload, also for higher modes, resulting in the smoothest behaviour of the system. Also the rms-values indicate that this controller has the best performance, except for x_{load}, although visually x_{load} is better. The only drawback of the P-PI F_{sens} with respect to the PI-P $\dot{x}_c$ is that the movement at the top is larger, increasing the chance of reaching the actuator's limits. The feedback signal coming from P-PI F_{sens} is also larger around the disturbance on F_{load}, but this is not significant as the magnitude is smaller than the feedforward signal, such that the energy demand will not be very different for both controllers. Whether or not the P-PI F_{sens} is still considered the best controller with parameter variations is evaluated in Chapter 6.

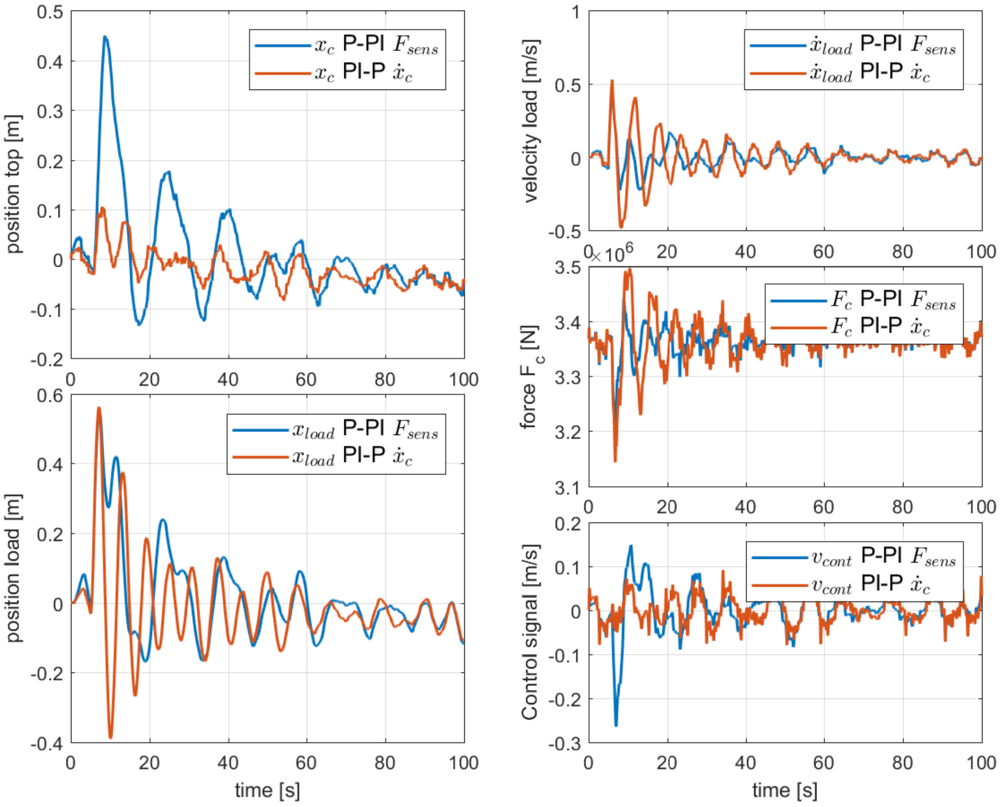

Figure 5-17: Simulation results of the PI-P $\dot{x}_c$ (with lead lag) and P-PI F_{sens} under influence of heave and . It can be seen that the large top motion of the P-PI F_{sens} results in comparable payload positions, but with a lower $\dot{x}_{load}$. Note that the depicted v_{cont} is the feedback signal only.

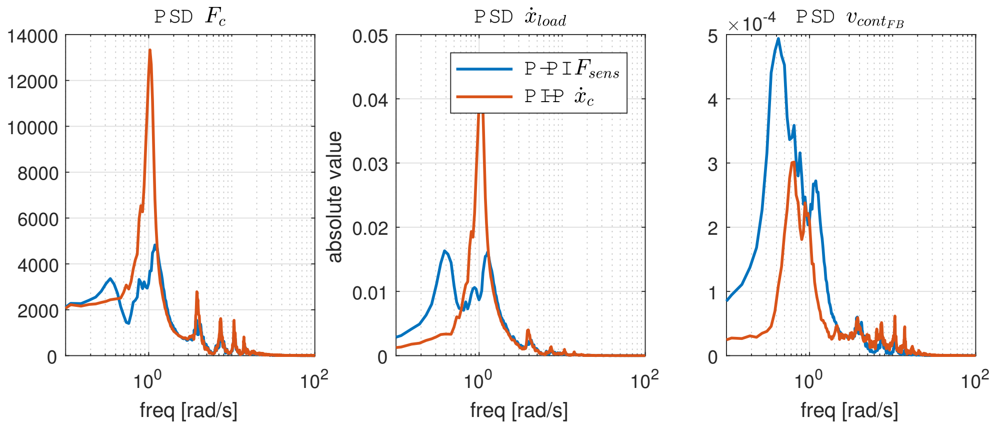

Figure 5-18: PSD of simulation results of the PI-P $\dot{x}_c$ (with lead lag) and P-PI F_{sens} for the signals F_c, $\dot{x}_{load}$ and $v_{cont_{FB}}$. This figure shows how much each frequency is represented in the respective signals.

Chapter 6

Controller Simulation and Parameter Variation

In Chapter 5 controllers are designed and simulated without sensor noise, control delays and parameter variations like the length and payload mass. The controllers are tuned on the specific length of 3000 m and 175×10^3 kg which might work only for this combination only. Therefore in this Chapter, it is investigated whether or not the controller is robust for changes in parameters.

As concluded in Chapter 5, only the parallel PIDs perform better with respect to the benchmark, while being robust to disturbances on F_{load}. Therefore only the benchmark, P-PI F_{sens} and PI-P $\dot{x}_c$ (with lead lag filter) are investigated in this Chapter.

6-1 Sensor Noise

Noise often limits the performance of real life applications, which is also the case for the controllers as designed in Chapter 5. The expected noise levels in the heave measurement and F_{sens} are evaluated in Section 3-2. Simulation results with this noise are depicted in Figure 6-1 for the time domain and Figure 6-2 for Power Spectral Density (PSD) analysis. Note that the order in which the PI-P $\dot{x}_c$ and P-PI F_{sens} are depicted is the opposite from Chapter 5. For both the P-PI F_{sens} and PI-P $\dot{x}_c$, the dampening of the payload is a little smaller compared to simulations without noise, especially for the P-PI F_{sens}. The noise does however not influence the performance too much as can be seen in the performance indicator, except for the force variations.

By inspection of the time domain, the *rms* performance indicator is misleading in the case of $\dot{x}_{load}$ and x_{load}. Comparison of a controller with and without noise (Figure C-1 in Appendix C) shows that the payload position and velocity are less desirable when simulated with noise, although the performance indicator states that for example the P-PI F_{sens} performs better on $\dot{x}_{load}$ *with* noise. The positions and velocities are less desirable as the position deviations of the payload are larger and contain on top of this high frequency oscillations, based on visual

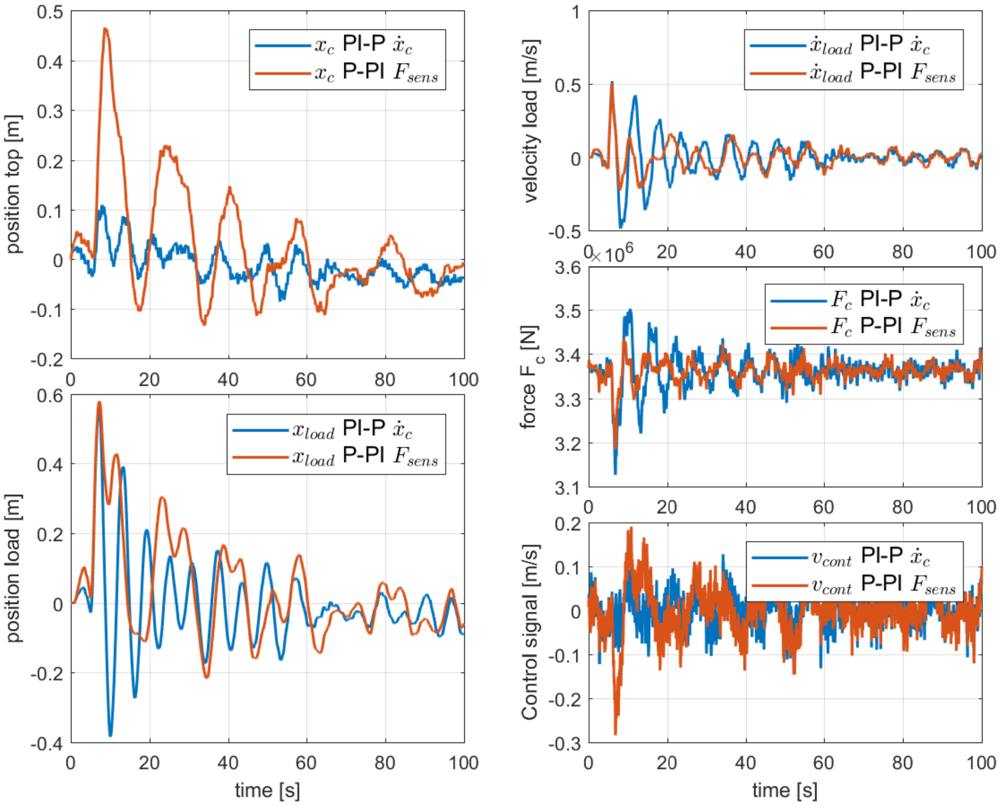

Figure 6-1: Simulation of P-PI F_{sens} and PI-P $\dot{x}_c$ with noise on $\dot{x}_{IMU}$ and F_{sens} with heave and disturbance on F_{load}.

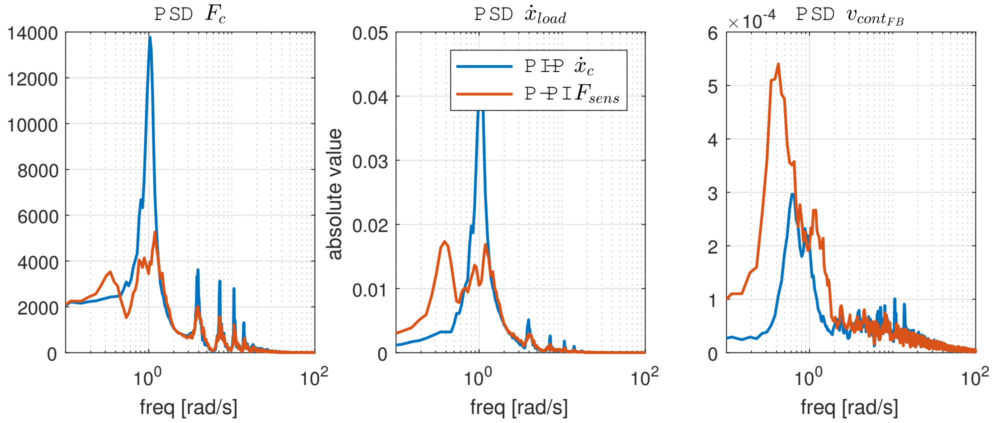

Figure 6-2: PSD of P-PI F_{sens} and PI-P $\dot{x}_c$ with noise on $\dot{x}_{IMU}$ and F_{sens} with heave and disturbance on F_{load}.

inspection. This is also visible when comparing the PSD with and without noise of the same controller (Figure C-2 in Appendix C). This shows that for both controllers the power at the resonance frequencies is higher with noise, while the power at the frequencies in between is almost the same. The PSD of $v_{cont_{FB}}$ has on top of this significantly more power at high frequencies due to noise, which is not desirable. Both controllers seem to have approximately the same level of robustness to noise.

Perfomance indicator: P-PI F_{sens} *with noise*

$rms_{\dot{x}_{load}}$	0.0853	[m/s]
$rms_{x_{load}}$	0.153	[m]
rms_{F_c}	2.45×10^4	[N]
$\dot{x}_{load-max}$	0.51	[m/s]

Perfomance indicator: P-PI F_{sens}

$rms_{\dot{x}_{load}}$	0.0934	[m/s]
$rms_{x_{load}}$	0.137	[m]
rms_{F_c}	2.22×10^4	[N]
$\dot{x}_{load-max}$	0.51	[m/s]

Perfomance indicator: PI-P $\dot{x}_c$ *with noise*

$rms_{\dot{x}_{load}}$	0.124	[m/s]
$rms_{x_{load}}$	0.129	[m]
rms_{F_c}	4.12×10^4	[N]
$\dot{x}_{load-max}$	0.52	[m/s]

Perfomance indicator: PI-P $\dot{x}_c$

$rms_{\dot{x}_{load}}$	0.124	[m/s]
$rms_{x_{load}}$	0.126	[m]
rms_{F_c}	3.84×10^4	[N]
$\dot{x}_{load-max}$	0.53	[m/s]

6-2 Control Delay

Delays especially influence the Phase Margin (PM) of the designed controllers (P-PI F_{sens} and PI-P $\dot{x}_c$). As described in Section 3-2, the delay in the controller is expected to be around 100 ms as a realistic estimate. This delay is defined as a time delay on the controller's output such that the transmission of each input to v_{cont} has the same delay (including the feedforward controller).

In frequency domain both parallel controllers have an unstable force feedback loop when a delay of 100 ms is inserted. As both controllers have almost identical force feedback loops at high frequencies (≈ 5 rad/s), their stability under delays is very similar. Both the P-PI F_{sens} and PI-P $\dot{x}_c$ only meet the linear stability margins (PM and Gain Margin (GM)) with a delay up to 25 ms, where the PM is the limiting factor[1]. Nevertheless the controllers are simulated with this delay, of which the results are depicted in Figure 6-3 and Figure 6-4. The simulation shows that the non-linear model is stable with both controllers, although the force variations on F_c are significantly larger compared to the simulation without delay. The difference between the linear and non-linear model can be explained by the hydrodynamic damping on the payload and cable, which is quadratic. Therefore the damping increases at higher velocities, such that more energy is dissipated. This protects the non-linear system from unbounded oscillations. It can be seen that especially the PI-P $\dot{x}_c$ has large force deviations, which is visible both in the time domain and PSD analysis.

The effect of delays on the behaviour of P-PI F_{sens}, PI-P $\dot{x}_c$ and the benchmark controller can be seen in Figures C-3 to C-8 where delays of 0, 50, 100 and 200 ms are depicted together. This shows that the PSD of F_c and $\dot{x}_{load}$ of the P-PI F_{sens} is most affected around 1 rad/s (the first resonant frequency) due to delays, while the PI-P $\dot{x}_c$ shows large differences around the third natural frequency. When simulated with only heave and a delay of 100 ms, the

---

[1] Based on a cable length of 3000 m and a payload mass of 175×10^3 kg

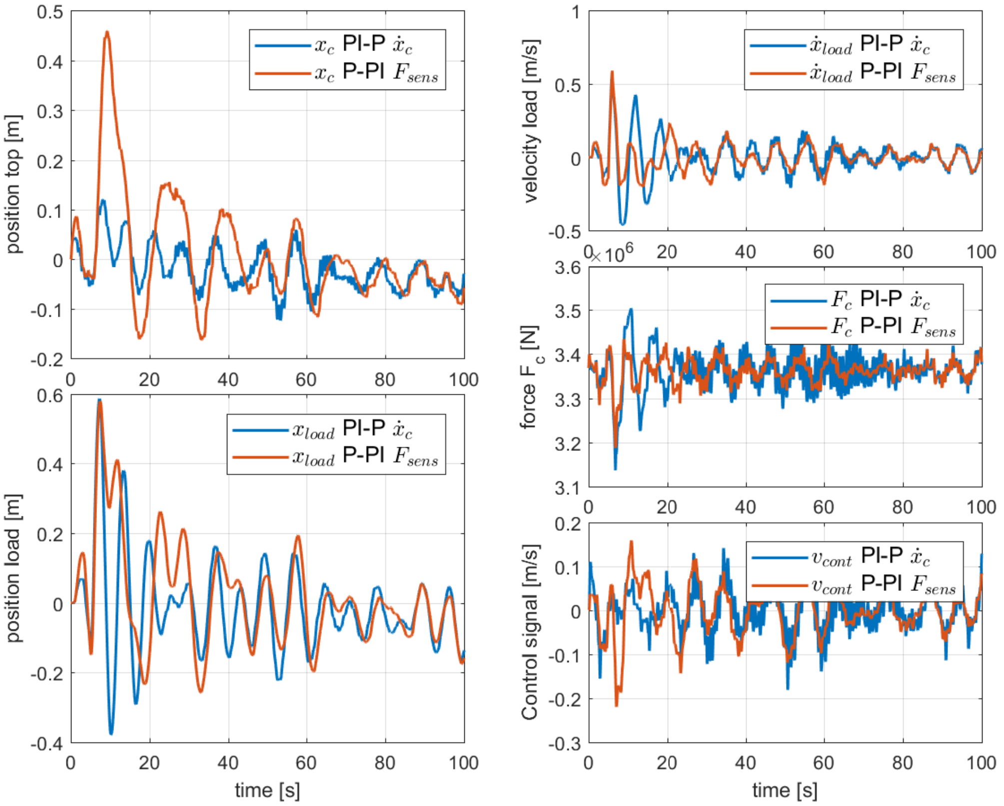

Figure 6-3: Simulation of P-PI F_{sens} and PI-P $\dot{x}_c$ with a delay of $0.1\,\mathrm{s}$ on the control signal (feedforward and feedback) with heave and disturbance on F_{load}.

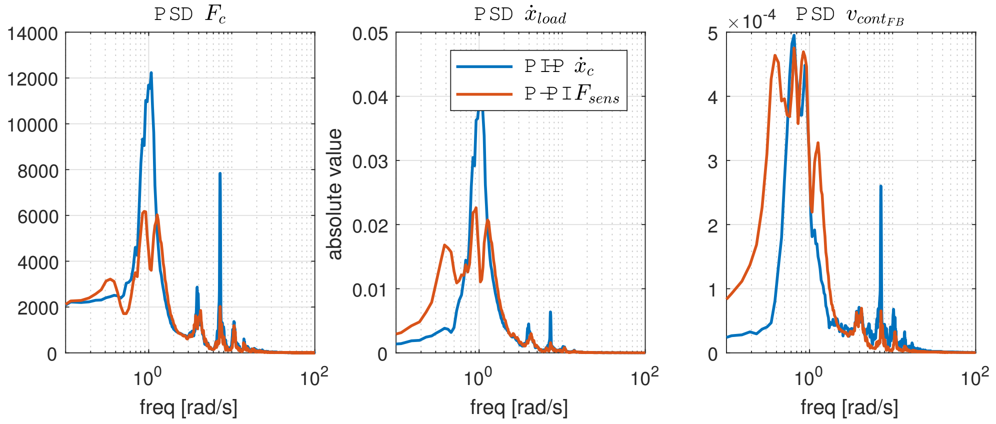

Figure 6-4: PSD of P-PI F_{sens} and PI-P $\dot{x}_c$ with a delay of $0.1\,\mathrm{s}$ on the control signal (feedforward and feedback) with heave and disturbance on F_{load}.

payload's position remain within tighter bounds with the PI-P $\dot{x}_c$ compared to P-PI F_{sens}, which suggests that the PI-P $\dot{x}_c$ performs better in counteracting heave motion. The velocities and force variations are however larger for the PI-P $\dot{x}_c$ as it contains a lot more high frequency oscillations. As can be expected, the benchmark controller also suffers from delays as visible in Figures C-7 and C-8. With this controller primarily the positions x_c and x_{load} are affected, while $\dot{x}_{load}$ and F_c only show minor degradation due to the delays.

As the PI-P $\dot{x}_c$ results in relatively high frequency oscillations, the force variations and payload velocity are very large, resulting in a lower performance than the P-PI F_{sens} under influence of delays. Based on Figures C-3 to C-6, delays cause primarily sustained high frequency payload oscillations when controlled with the PI-P $\dot{x}_c$, while the performance of P-PI F_{sens} is affected on a wide range of frequencies. Altogether, the P-PI F_{sens} results in the most desirable behaviour under the influence of delays.

6-3 Cable Length variation

Cable length variations are very important in Heave Compensation (HC), as the payload has to be lowered from a ship to the sea bed, such that each cable length in between occurs at a lifting operation. This emphasises the demand for a controller which is stable for each cable length. In this Thesis, a cable length is investigated between 100 and 3000 m, of which only 500 and 3000 m are discussed in this Thesis. In order to investigate the effect of length variations and stability at other cable lengths, a range of values is also investigated[2] of which the results are not explicitly shown in this Thesis.

Frequency response plots of the plants of respectively the force and velocity feedback loop for 500 and 3000 m are depicted in Figure 6-5 and Figure 6-6. The investigated payload mass is 175×10^3 kg. Note that also a combination of 3000 m with 10×10^3 kg is depicted, which is discussed in Section 6-4.

A short cable has higher resonance frequencies than a long cable when the same payload is connected. This is clearly visible in Figure 6-5 where the natural frequencies of the 500 m cable are significantly higher and are larger in magnitude compared to those with the 3000 m cable and the same payload mass. In the velocity plant (Figure 6-6), the resonant frequencies introduce large peaks and dips in magnitude and a local phase lag of about 135°. This peak and phase lag imply control limits when using a velocity feedback loop with a bandwidth around this frequency or higher.

The second natural frequency of the 500 m cable is higher than 20 rad/s, such that this peak has to be below 0 dB according to the defined maximum bandwidth. Both the P-PI F_{sens} and PI-P $\dot{x}_c$ as designed in Chapter 5 do not meet this requirement on bandwidth, combined with a too low PM of 20°.

Controller adaptation to 500 m cable

The P-PI F_{sens} controller is adapted to be used with a cable length of 500 m by lowering the K_P gain of the force feedback loop by gain scheduling. This resolves the PM and bandwidth

---

[2] The cable lengths of 100, 500, 1000, 1500, 2000, 2500 and 3000 m are used for this investigation

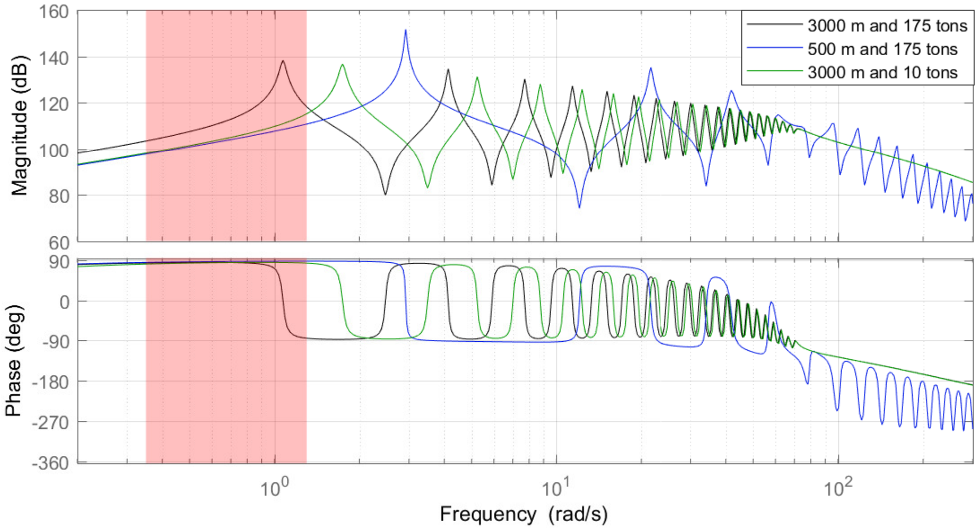

Figure 6-5: Bode plot of the System Model from v_{cont} to F_{sens} (the force feedback plant) with a cable length of $3000\,\mathrm{m}$ and $500\,\mathrm{m}$ with a payload mass of $175 \times 10^3\,\mathrm{kg}$, along with a cable length of $3000\,\mathrm{m}$ and $10 \times 10^3\,\mathrm{kg}$.

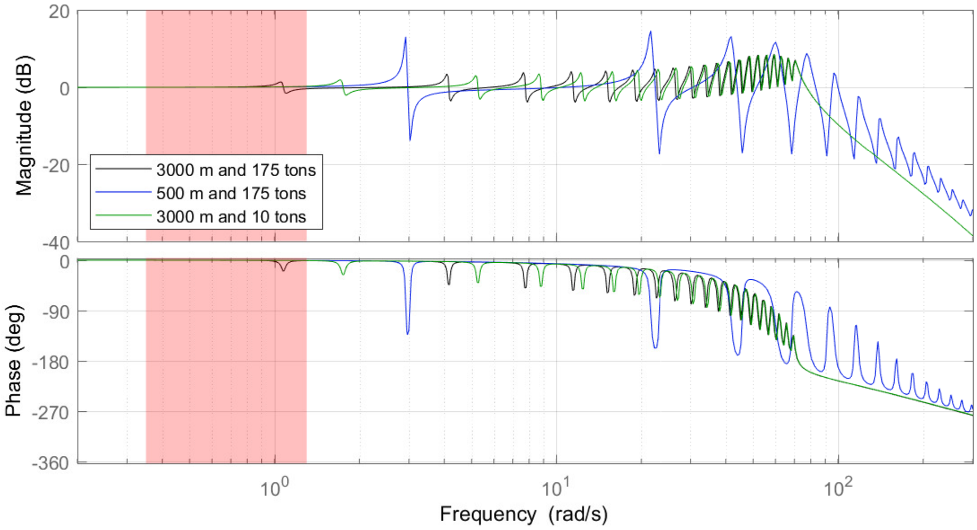

Figure 6-6: Bode plot of the System Model from v_{cont} to $\dot{x}_c$ (the velocity feedback plant) with a cable length of $3000\,\mathrm{m}$ and $500\,\mathrm{m}$ with a payload mass of $175 \times 10^3\,\mathrm{kg}$, along with a cable length of $3000\,\mathrm{m}$ and $10 \times 10^3\,\mathrm{kg}$.

requirements of the force feedback loop, while the velocity feedback still has adequate PM and GM.

When the cable length is set to 500 m, the velocity feedback of the PI-P $\dot{x}_c$ results in an unstable internal system[3]. In order to solve this, the bandwidth of the velocity feedback has to be reduced, such that the velocity feedback part becomes very comparable to that of P-PI F_{sens}. Therefore the PI-P $\dot{x}_c$ is not adapted, as the resulting controller is very similar to the P-PI F_{sens} except for the inverted notch.

Simulation results without noise and delays

Simulation results with the benchmark, P-PI F_{sens} with and without gain scheduling (gs) and the PI-P $\dot{x}_c$ is depicted in Figure 6-7 and Figure 6-8. In the time domain, it can be seen that the magnitude of the payload movement in this simulation is less than with the cable of 3000 m as can be seen in for example Figure 5-13 and Figure 5-16. In these figures the same controllers are included (except the one with gain scheduling), with as only difference a another cable length. The position of the payload remains within a smaller range for the short cable, while the payload's velocities are comparable in magnitude. The PI-P $\dot{x}_c$ which turned out to be unstable in the linear model turns out to be stable in the non-linear simulation. Due to the high frequencies, the performance is hard to inspect using the time domain, such that the performance is investigated with a larger focus on the PSD.

PSD analysis shows that the payload oscillates primarily in it's first resonant frequency when the benchmark controller is applied. The P-PI F_{sens} without gain scheduling performs best at rejecting the first natural frequency in both F_c and $\dot{x}_{load}$. The PI-P $\dot{x}_c$ on the other hand has the lowest payload velocities around the heave frequency band at the cost of a little higher force variation at those frequencies. The P-PI F_{sens} with adapted gain shows PSD values which are in between those of the two parallel PIDs without gain scheduling.

When no disturbance on F_{load} is exerted (in other words, only heave), the PI-P $\dot{x}_c$ performs best at minimising the payload's motion, but it causes high frequency oscillation in x_c at around 15 rad/s which is definitely not desired in practice (noise, vibrations etc.). In this case the P-PI F_{sens} with gain scheduling is at practically every frequency outperformed by the P-PI F_{sens} with adapted gain, at the cost of a larger feedback signal.

Simulation results with noise and delays

When noise is added to the simulations, the difference in PSD values of the P-PI F_{sens} with and without gain scheduling are becoming smaller compared to the simulation in Figure 6-7. This result is based on the noise as described in Section 3-2 and a delay of 100 ms. The P-PI F_{sens} without gain scheduling performs however still best when it comes to F_c when the entire frequency range is considered and best on $\dot{x}_{load}$ for high frequencies. The payload position is minimised best with the PI-P $\dot{x}_c$, but at the cost of high frequency oscillations.

The P-PI F_{sens} without gain scheduling performs best with a cable length of 500 m and a payload mass of 175×10^3 kg. Even though linear analysis shows a very low phase margin

---

[3] The cable and payload become a non-minimum phase system, which shows a phase of $-270°$ instead of the expected $90°$ before the first natural frequency. This is caused by a pole in the right half plane.

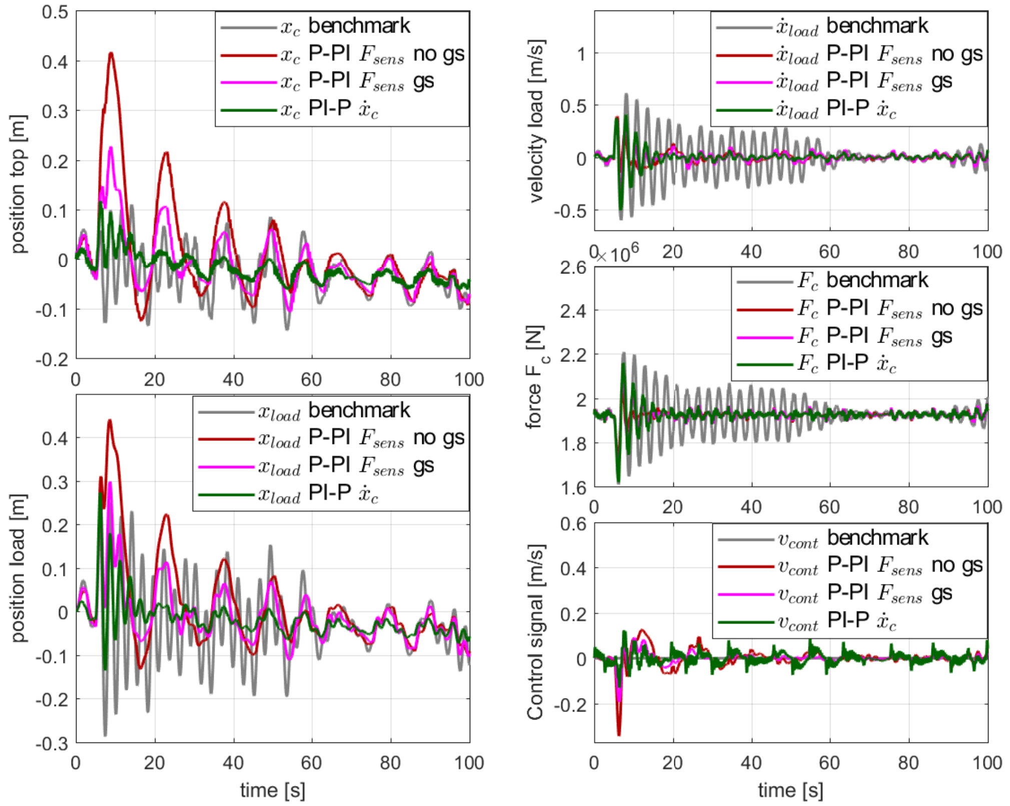

Figure 6-7: Simulation of the benchmark controller, P-PI F_{sens} with and without gain scheduling (gs) and the PI-P $\dot{x}_c$ with a cable length of $500\,\mathrm{m}$. The controller with gs has a lower gain in the force feedback loop. The simulation is performed with heave and the disturbance on F_{load} with a payload mass of $175 \times 10^3\,\mathrm{kg}$. The PSD of this figure is depicted in Figure 6-8.

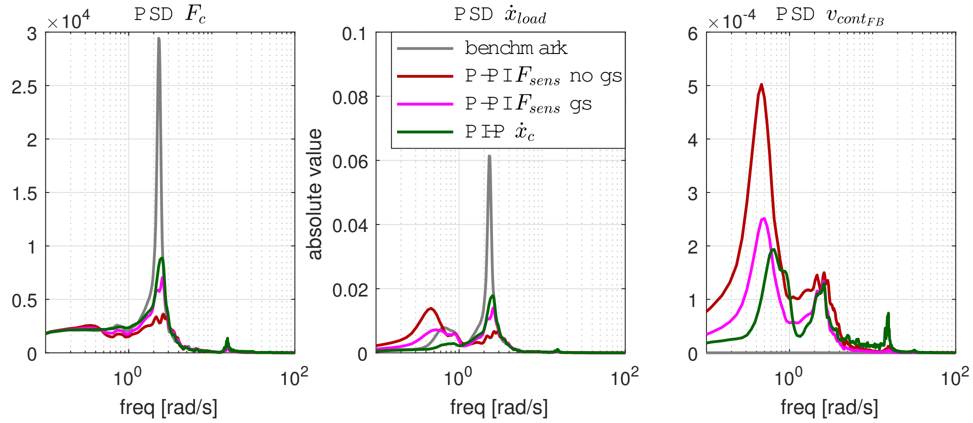

Figure 6-8: PSD of the benchmark controller, P-PI F_{sens} with and without gain scheduling (gs) and the PI-P $\dot{x}_c$ with a cable length of $500\,\mathrm{m}$. The controller with gs has a lower gain in the force feedback loop. The simulation is performed with heave and the disturbance on F_{load} with a payload mass of $175 \times 10^3\,\mathrm{kg}$. The simulation of this figure is depicted in Figure 6-7.

of 20° at a frequency of 22 rad/s, simulations indicate that the system is stable with noise and delays. This is not expected from the linear model, as a delay of 100 ms results in a significantly higher phase lag than the 20° at this frequency, which would result in an unstable system. Consequently, it can be concluded that the non-linear model is less sensitive in the high frequencies from v_{cont} to F_c than expected from the linear model.

In different scenario's with and without noise, delays and other cable lengths, the P-PI F_{sens} performs best[4]. This is *without* the proposed gain scheduling, which turns out to be not necessary due to differences between the non-linear simulation model and the linearised version used for control design.

6-4 Payload Mass variation

The controllers (P-PI F_{sens} and PI-P $\dot{x}_c$) are designed to be used with a payload mass of 175×10^3 kg, which is the maximum load. When the payload mass is smaller, the natural frequencies rise. The frequency response of a cable of 3000 m with a payload mass of 10×10^3 and 175×10^3 kg are depicted alongside in Figure 6-5 (force loop) and Figure 6-5 (velocity feedback loop). The bode plots indicate that the magnitude and phase with the small load appear to be shifted to higher frequencies, while the shape of the magnitude and phase remain comparable.

Both controllers (P-PI F_{sens} and PI-P $\dot{x}_c$) as designed in Chapter 5 are robust to variation of the payload mass with a cable length of 3000 m in linear frequency analysis. This is verified with payload masses of 100×10^3 and 10×10^3 kg, thus only smaller inertia's as the test case already consists of the maximum load. The PM of the force feedback loops increases for both controllers when a smaller payload mass is used, while the velocity feedback loops still have high PM. At a cable length of 500 m, the P-PI F_{sens} PM in the force feedback is also improved with a small payload mass, although it is still less than 45°, based on a mass of 10×10^3 kg. The PI-P $\dot{x}_c$ remains unstable with the linear model and load variation at 500 m (see Section 6-3).

Based on the linearised System Model, there is no need for control adaptation when using a lighter payload. Even though the resonant frequencies become higher, the magnitude and phase are similar and even a little more beneficial, resulting in a minor increase of phase margins of the force feedback loops. Therefore, the controller tuning could best be performed with the heaviest load.

Simulations show that decreased payload mass does not influence the stability with both controllers at 3000 m. At 500 m cable length, the PI-P $\dot{x}_c$ has very low damping with a 10×10^3 kg payload, and becomes unstable when a delay of 100 ms is simulated. With payload masses of 100×10^3 and 175×10^3 kg , the PI-P $\dot{x}_c$ is however stable under these conditions. The P-PI F_{sens} turns out to be stable at both cable lengths and the three different payload masses, also with noise and control delays up to at least 200 ms. Simulation results with the P-PI F_{sens}, a 3000 m cable and the three different payload masses is depicted in Figure 6-9

---

[4] The P-PI F_{sens} performs especially well compared to the PI-P $\dot{x}_c$ when large payload masses are involved. The P-PI F_{sens} has in every case the best performance at high frequencies, while the PI-P $\dot{x}_c$ is usually best at low frequencies due to the relatively large low frequency payload motion due to the disturbance at F_{load} of the P-PI F_{sens}. Altogether, the P-PI F_{sens} results in the smoothest payload motion

for the time domain and the corresponding PSD in Figure 6-10. The difference in payload motion directly after the disturbance on F_{load} (at $t = 5\,\mathrm{s}$) is caused by the magnitude of the force disturbance, which is linearly dependent on the payload's inertia. Due to the significant cable inertia, the payload motion is smaller when the payload is less heavy.
An interesting phenomenon with small payload mass is the spikes in $\dot{x}_{load}$ as visible in Figure 6-9. These are caused by the coulomb friction in the heave compensation cylinder, which affect the payload movement. As can be seen, the spikes in F_c are comparable in magnitude at the end of the simulation which indicate that the force variation due to this friction is comparable.

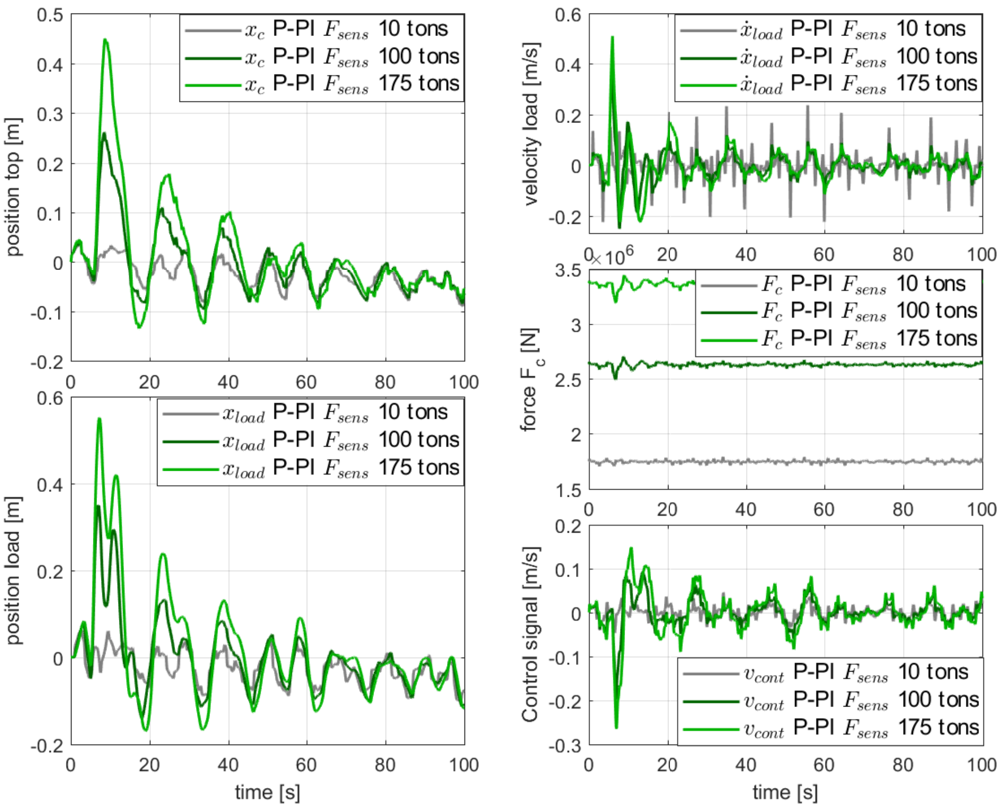

Figure 6-9: Simulation with payload masses of 10×10^3, 100×10^3 and $175 \times 10^3\,\mathrm{kg}$ with heave and disturbance on F_{load}. The difference in payload motion directly after the disturbance on F_{load} (at $t = 55\,\mathrm{s}$) is caused by the magnitude of the force disturbance. The controller is the P-PI F_{sens} with a cable length of $3000\,\mathrm{m}$.

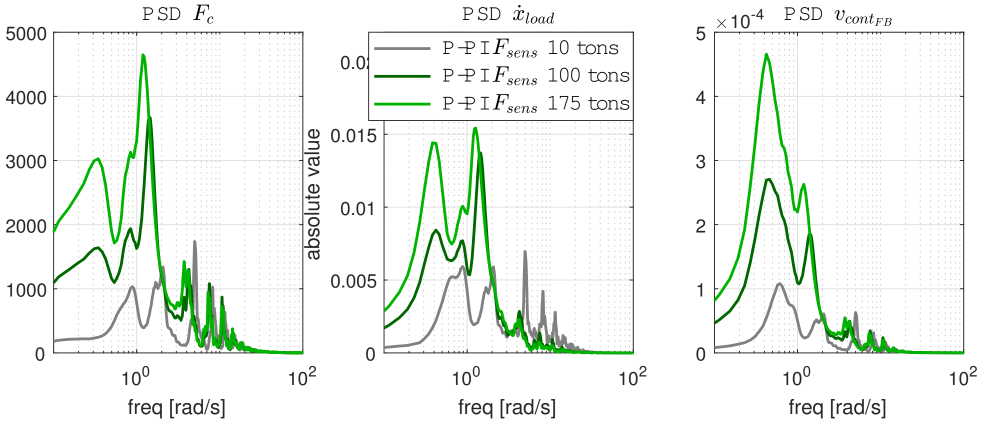

Figure 6-10: PSD with payload masses of 10×10^3, 100×10^3 and $175 \times 10^3\,\mathrm{kg}$ with heave and disturbance on F_{load}. The controller is the P-PI F_{sens} with a cable length of $3000\,\mathrm{m}$.

Chapter 7

Conclusion

In this Thesis, the dynamics involved with a marine lifting operation where the payload is hanging in deep sea is investigated and controlled. Under influence of the ship's heave (= vertical motion due to waves), the payload also moves, which has to be compensated with Heave Compensation (HC). A HC system aims to reduce the payload's motion due to ship movement and force variations in the cable, which requires to adapt the cable length dynamically. There are several working principles of HC used in practice, both active as passive, with multiple set-ups in order to control the cable length.
The considered actuator is a sheave-based heave compensation cylinder as depicted in Figure 7-1, composed of hydraulic cylinders (one active and a passive cylinder) between two sheaves. As the cable is wound around these sheaves, the cable is retracted when the hydraulic cylinders extract. This mechanism is called the heave compensation cylinder in this Thesis. A high fidelity non-linear simulation model is created of this actuator as well as a linearised model used for control design. Additionally sensor noise of an Inertial Measurement Unit (IMU) which measures the heave motion and that of a force sensor which measures the tension in the cable around the crane tip. The lifting and lowering of the payload itself is not evaluated in this Thesis, such that the winch (as visible in Figure 7-1) is not modelled nor discussed.

The cable dynamics are very important for HC in deep sea, as the cable and payload oscillate in multiple resonant frequencies. These resonant frequencies are usually not considered in Literature, which use very simplified cable models. In this Thesis, the cable dynamics are modelled using two separate techniques such that the most realistic cable model is generated. A cable model based on division of the cable in small sections is compared to a model based on the cable's Partial Differential Equation (PDE). Although both models resulted in very similar behaviour, the PDE model gives more accurate results due to material damping of the cable. Simulations point out that several resonant modes of the cable and payload combination are exited. Consequently, the inclusion of multiple resonances in the cable model proves to be required, even though these resonant frequencies are not exited by the frequencies in which the ship heaves.

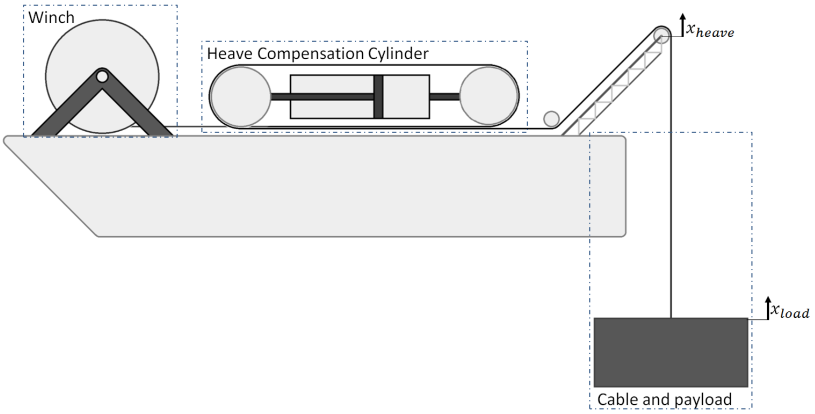

Figure 7-1: Mechanical design of the heave compensator on a ship, comprising of a winch, a heave compensation cylinder, a cable and a load. The variables x_{heave} and x_{load} are shown at the points where they are defined. Note that this figure is not drawn to scale.

7-1 Control Results

The performance of HC systems at large depths is increased significantly with use of PIDs. Without control, the payload's vertical peak to peak movement exceeds the ships heave elevation by a factor 2 as worst case position deviation. This is based on simulations with a cable of 3000 m and a payload mass of 175×10^3 kg under the influence of 4 m Significant Wave Height (SWH) waves which are depicted in Figure C-9 and Figure C-10. With different levels of control, this payload motion is improved, as summarised in Table 7-1[1]. The addition of feedforward (FF) control on the heave measurement already brings down the payload motion, which is further reduced by feedback (FB) control. With addition of realistic levels of noise and delays, the performance is slightly decreased.

The mentioned performance is dependant on several quantities, namely position payload deviation, payload velocities and force variations at the top of the cable. All these quantities are aimed to be minimised, although minimising one quantity does not necessarily reduce the others. Also the frequency content of oscillations is in some cases decisive to answer the question which simulation shows better performance. At last, a visual inspection helps deciding which behaviour is best, and thus has the highest performance.

Table 7-1: maximum peak to peak position deviation of an 175×10^3 kg payload hanging at an 3000 m long cable with an SWH of 4 m.

heave elevation ship	3.5 m
payload motion without control	9.5 m
payload motion with FF control (benchmark)	0.95 m
payload motion with FF and FB control (no noise and delays)	0.35 m
payload motion with FF and FB control (with noise and delays)	0.45 m

Three PID configurations, all with feedforward on the measured heave velocity, are compared

---

[1] The values of Table 7-1 are based on the same simulations as these figures, where the disturbance at $t = 230$ s is neglected

to a benchmark controller, which is a pure feedforward on the measured heave. This comparison is initially performed at one working point with ideal measurements (no noise and delay) on the non-linear simulation model. The best controllers are later on evaluated with other cable lengths, payload masses, noise and delay. As disturbances the heave motion, which is measured by an IMU, and an unmeasured impulse force on the payload (F_{load}) is inserted. These disturbances allow to evaluate the controllers on how well the heave is rejected in the payload motion and how fast unmeasured disturbances on the payload are dampened out.

A PI controller on the cable top velocity $\dot{x}_c$, with feedforward, is at this depth unable to reject the heave motion any better than the benchmark controller. This is because the controller aims to keep the top of the cable as static as possible, which diminishes the cable's damping. The low damping in it's turn causes the cable and payload to oscillate in it's eigenfrequencies which results in a worse performance at this depth than the benchmark controller.
The feedforward combined with a P controller on the measured force at the top of the cable (F_{sens}) results in a lot better performance, both in decreasing payload motion and reducing force variations. As no feedback on the position of the actuator is present, the controller is prone to drifting away of the heave compensation cylinder, such that the cylinder is limited by the end of it's stroke. As this control structure performs well, the P on F_{sens} is extended with PI velocity feedback to prevent drifting.

Parallel PID combinations

With a parallel PID structure the best property of the PI on $\dot{x}_c$ (position tracking) is combined with the best of P control on F_{sens} (payload damping). Two types of balances between these two are used for tuning the separate PIDs:

P-PI F_{sens}	emphasis on force control (P) with velocity control (PI) for tracking
PI-P $\dot{x}_c$	emphasis on velocity control (PI) with payload damping by force control (P)

In the P-PI F_{sens} controller, the force loop is responsible for rejection of the heave motion. This capability is improved by increasing the gain in the frequency band contained in the heave motion with an inverted notch filter. In comparison to the standalone force feedback, this results in better heave rejection at the cost of being more prone to drifting. As the (low bandwidth) velocity feedback takes care of this, drifting is no longer a problem. Due to the velocity feedback, the P-PI F_{sens} dampens the payload less quick, but in turn the heave is better rejected and the system does not drift.

The tuning of the PI-P $\dot{x}_c$ is performed such that the velocity feedback is active around the frequencies contained in the heave motion. Parallel to this controller the force feedback is applied with the same gain as on the P-PI F_{sens}, but without the inverted notch. A lead-lag filter is added to the velocity feedback which improves stability margins of the linear design and non-linear simulation performance. This structure performs comparable to P-PI F_{sens}, but with a lower damping on the payload motion. When subjected to only heave, x_{load} has lower amplitudes, but has high frequency oscillations which gives worse results on $\dot{x}_{load}$ compared to the P-PI F_{sens}. Therefore the P-PI F_{sens} is considered as the best performing controller at 3000 m depth and a payload of 175×10^3 kg and without noise and delays.

Under influence of noise in measurements of $\dot{x}_{IMU}$ and F_{sens} and a 0.1 s delay in the control signal, the P-PI F_{sens} has a decreased performance, but still manages to keep the payload static with a maximum peak to peak motion of 0.45 m instead of 0.35 m. The vertical position stays within a range of ≈ 0.4 m for the PI-P $\dot{x}_c$, but the cable force and $\dot{x}_{load}$ show significant high frequency oscillations, which is definitely not desired in HC. Therefore the P-PI F_{sens} is chosen as the best performing and most robust controller under influence of noise and delays.

Both the PI-P $\dot{x}_c$ and P-PI F_{sens} are simulated under parameter variations, where both controllers prove to be robust to other (smaller) payload masses. when decreasing the cable length to 500 m, the P-PI F_{sens} has low linear stability margins (Gain Margin (GM) and Phase Margin (PM)) and the PI-P $\dot{x}_c$ is even unstable on the linearised model. Simulations (on the non-linear model) however point out that both controllers are stable[2], although the PI-P $\dot{x}_c$ suffers from high frequency oscillations of the payload. This could be solved using gain scheduling, which is only performed for the P-PI F_{sens}, as the other controller would be almost equal to the P-PI F_{sens} when gain scheduling is used to render the system stable on the linear model. Simulations point out that non-gain scheduled P-PI F_{sens} is at 500 m still stable with noise and delays, and it shows that the gain scheduled P-PI F_{sens} has decreased performance. Consequently, gain scheduling is not required, it is more complicated and it decreases performance, such that gain scheduling is not recommended.

Variation of the payload mass also does not require gain scheduling, and even is a little more stable, as long as the payload is lighter than the mass for which the controller is tuned.

Based on the aspects as described in the foregoing, the parallel controller with a focus on F_{sens} control (P-PI F_{sens}) is the best controller for HC at deep sea to minimise the payload's motion and force variations. This controller is:

- robust to cable length and payload mass variation
- robust to expected levels of noise and delays
- high performance, especially at high frequency oscillations
- smooth dampening out of payload motion

7-2 Recommendations for further investigation

The following subjects are still open for investigation, categorised by subject.

Validating the simulation model:

---

[2] The fact that the controller is unstable on the linear model and stable on the non-linear model is caused by the quadratic damping present on the cable and payload. When the

Cable dynamics measurement In order to validate the dynamics of the cable, like damping forces and non-linearities, the model should be compared to real-life measurements. This could be done with accelerometers at the payload and preferably also on the cable. Based on these measurements the cable model could be verified or fitted to the data. Especially for long cables this is interesting.

Real-life (scale model) tests The proposed controller should be validated in a real-life test. These are however very expensive and possibly dangerous, which could be overcome by scale tests.

Improving passive compensator performance:

Optimize the passive cylinder The passive cylinder and the size of the accumulator could be optimized to work with the controller. The larger the accumulator, the more constant the pressures and forces will be from the passive cylinder. Larger accumulators are however more expensive, and the controller should handle less constant forces without problems, but probably at the cost of more energy losses and little less performance.

Insert a passive heave compensator at the bottom of the cable The cable dynamics can be changed using a passive heave compensator connected to the payload. This should reduce especially the high frequency oscillations, and could therefore be beneficial. A drawback would be the cost of the passive cylinder and the need of adapting the device to the payload's mass.

Improving simulation accuracy:

Discrete control The controllers are designed and simulated in continuous time, such that they have to be converted to discrete time in order to be used in conventional control computers. This will deteriorate the performance, although it is expected not to be severe. An even better option would be to use hardware in the loop instead of a full simulation.

Include a winch and crane model The cable is assumed to be clamped at the point where it is connected to the winch, while in reality the winch would slightly give way. Additionally, the crane would move a little as result of force variations. Both of these phenomena results in a less stiff connection to the ship. The effect of these are assumed to be negligible compared to the cable's stiffness at long cable lengths. With a short cable, these effects will result in other dynamics, such that these effects have to be modelled when evaluating lifting operations with this controller from 0 up to 3000 m.

Investigate the touchdown of the payload on the sea bed It would be interesting to investigate what happens when the payload is lowered down on the sea bed. It could be that the payload hits the sea bed, is lifted up again and hits the sea bed for multiple times in a row, which has to be avoided. This is also dangerous as it could result in slack wire, which could cause cable breakage or damage to the payload. The controller should be optimised for this, if this phenomenon occurs.

Hydraulic model The hydraulics used in the heave compensation cylinder assume an immediate change in oil flows when when the valve opening changes. This is partially accounted for by high-pass filtering the control signal. This results in a more smooth behaviour of the valve, such that the oil flow also has to change less abrupt. It is however a simplification which should especially be investigated when the controller will be used in practice, as in general multiple valves are used instead of the one modelled valve. This also brings in more non-linearities to the valve and cylinder model.

Appendix A

Cable Model Derivation

In this Appendix some mathematical derivations are presented used to derive the cable model based on Partial Differential Equation (PDE). The Appendix is divided in several sections, based on separate derivations which are referred to in Chapter 4.

A-1 PDE: Separation of Variables

Start with Equation 4-6, which is also shown here for convenience:

$$c^2 \frac{\partial^2 u}{\partial x^2}(x,t) = \frac{\partial^2 u}{\partial t^2}(x,t)$$

Where $u(x,t)$ is the axial displacement of the cable due to stretch at position x at time t. Based on the principle of separation of variables, $u(x,t)$ is written as:

$$u(x,t) = U(x)T(t) \tag{A-1}$$

Now substitute Equation A-1 in 4-6:

$$c^2 U''(x)T(t) = U(x)\ddot{T}(t) \tag{A-2}$$

$$c^2 \frac{U''(x)}{U(x)} = \frac{\ddot{T}(t)}{T(t)} \tag{A-3}$$

With $\square'$ a derivative with respect to x, and $\dot{\square}$ a derivative to time. As the left side of Equation A-3 is only dependant on t, and the right side is only dependant on x, the equation must be equal to a constant, which is defined as $-\omega^2$. This results in periodic solutions for both $U(x)$ and $T(t)$:

$$U(x) = \alpha_1 \cos\left(\frac{\omega x}{c}\right) + \alpha_2 \sin\left(\frac{\omega x}{c}\right) \tag{A-4}$$

$$T(t) = \alpha_3 \cos(\omega t) + \alpha_4 \sin(\omega t) \tag{A-5}$$

With:

$U(x)$ = mode shape of the cable [m]
$T(t)$ = homogeneous evolution over time
α_i = arbitrary constant
ω = frequency of vibration [rad/s]

In general, $u(x,t)$ is built up of an infinite set of different modes, such that:

$$u(x,t) = \sum_{i=1}^{\infty} U_i(x) T_i(t) \tag{A-6}$$

Where i is used to denote different modes.

A-2 PDE: Orthogonality

Start with the governing equation of the PDE, Equation 4-2 which is:

$$E_c A_c \frac{\partial^2 u}{\partial x^2}(x,t) + f(x,t) = \rho_c A_c \frac{\partial^2 u}{\partial t^2}(x,t) \tag{A-7}$$

Define $f(x,t) = 0 \ \forall (x,t)$ (which gives the homogeneous solution) and fill in a random outcome of the free vibration response, denoted as $U_i(x)T_i(t)$. With $\dot{\square} = \frac{\partial \square}{\partial t}$ and $\square' = \frac{\partial \square}{\partial x}$, this results in:

$$E_c A_c U_i''(x) T_i(t) = \rho_c A_c U_i(x) \ddot{T}_i(t) \tag{A-8}$$

$$\tag{A-9}$$

With $\ddot{T}_i(t) = -\omega_i^2 T_i(t)$ as follows from the definition of T in Equation A-5, the foregoing can be rewritten as:

$$E_c A_c U_i''(x) T_i(t) = -\rho_c A_c \omega_i^2 U_i(x) T_i(t) \tag{A-10}$$

When the case of $T_i(t) \equiv 0 \ \forall (x,t)$ is neglected (which is the trivial solution), T_i can be taken out of the equation. Additionally, the equation is divided by A_c and the simplification constant $c = \sqrt{\frac{E_c}{\rho_c}}$ is substituted:

$$U_i''(x) = -\frac{\omega_i^2}{c^2} U_i(x) \tag{A-11}$$

This is multiplied with mode-shape $U_j(x)$ and integrated over x from 0 to l[1]:

$$\int_0^l U_i''(x)U_j(x)dx = -\frac{\omega_i^2}{c^2}\int_0^l U_i(x)U_j(x)dx \tag{A-12}$$

Partial differentiation of the left term gives:

$$\begin{aligned}\int_0^l U_i''(x)U_j(x)dx &= [U_i'(x)U_j(x)]_0^l - \int_0^l U_i'(x)U_j'(x)dx\\ &= U_i'(x=l)U_j(x=l) - \int_0^l U_i'(x)U_j'(x)dx\end{aligned} \tag{A-13}$$

Where the equation is simplified using the free boundary condition[2] at $x = 0$, which implies that $U_i'(x = 0) \equiv 0$. This is substituted in Equation A-12:

$$U_i'(x=l)U_j(x=l) - \int_0^l U_i'(x)U_j'(x)dx = -\frac{\omega_i^2}{c^2}\int_0^l U_i(x)U_j(x)dx \tag{A-14}$$

In order to simplify the terms $U_i'(x = l)U_j(x = l)$ and $U_j'(x = l)U_i(x = l)$, the boundary condition at $x = l$ has to be evaluated. This is done similar to the derivations before, starting with the boundary condition itself as defined in Equation 4-11, which is also shown here for convenience.

$$E_cA_c\frac{\partial u}{\partial x}(x=l,t) = -M\frac{\partial^2 u}{\partial t^2}(x=l,t) \tag{A-15}$$

$$E_cA_cU_i'(x=l)T_i(t) = -MU_i(x=l)\ddot{T}_i(t) \tag{A-16}$$

$$E_cA_cU_i'(x=l)T_i(t) = \omega_i^2MU_i(x=l)T_i(t) \tag{A-17}$$

$$E_cA_cU_i'(x=l) = \omega_i^2MU_i(x=l) \tag{A-18}$$

A new constant $\tilde{M} = \frac{M}{\rho_cA_c}$ is substituted in the equation, which can be seen as replacing the payload by an equivalent rigid piece of cable of length $\tilde{M}$. Combined with the substitution of the constant c results in:

$$U_i'(x=l) = \frac{\omega_i^2}{c^2}\tilde{M}U_i(x=l) \tag{A-19}$$

$$\tag{A-20}$$

This result is inserted in Equation A-14, with reordering:

---

[1] This results later on in the drop-out of some terms.

[2] Defined in Equation 4-10

$$\frac{\omega_i^2}{c^2}\tilde{M}U_i(x=l)U_j(x=l) - \int_0^l U_i'(x)U_j'(x)dx = -\frac{\omega_i^2}{c^2}\int_0^l U_i(x)U_j(x)dx \tag{A-21}$$

$$\frac{\omega_i^2}{c^2}\left(\int_0^l U_i(x)U_j(x)dx + \tilde{M}U_i(x=l)U_j(x=l)\right) = \int_0^l U_i'(x)U_j'(x)dx \tag{A-22}$$

Now Equation A-22 is copied, by flipping i and j:

$$\frac{\omega_j^2}{c^2}\left(\int_0^l U_j(x)U_i(x)dx + \tilde{M}U_j(x=l)U_i(x=l)\right) = \int_0^l U_j'(x)U_i'(x)dx \tag{A-23}$$

As U_i is a one-dimensional quantity, the order of multiplication does not matter. This property is used when Equation A-23 is subtracted from A-22, which results in:

$$\left(\frac{\omega_i^2}{c^2} - \frac{\omega_j^2}{c^2}\right)\left(\int_0^l U_i(x)U_j(x)dx + \tilde{M}U_i(x=l)U_j(x=l)\right) = 0 \tag{A-24}$$

As ω_i and ω_j are distinct eigenvalues (for $i \neq j$), it follows that for any $i \neq j$:

$$\rho_c A_c \int_0^l U_i(x)U_j(x)dx + MU_i(x=l)U_j(x=l) = 0 \tag{A-25}$$

This result indicates that the results are orthogonal, and therefore do not influence each other. This means that the cable and payload are able to oscillate in one natural frequency, without exiting other modes.

A-3 PDE: Derivation of Forced Response

The forced response of the cable is derived using the principle of conservation of energy. More specific: the internal energy of the cable-mass system changes according the work performed on it:

$$\begin{aligned}\underbrace{\frac{1}{2}\int_0^{l_c}\rho_c A_c\left(\frac{\partial u}{\partial t}(x,t)\right)^2 dx + \frac{1}{2}M\left(\frac{\partial u}{\partial t}(x=l_c,t)\right)^2}_{\text{Kinetic Energy}} + \underbrace{\frac{1}{2}\int_0^{l_c}E_c A_c\left(\frac{\partial u}{\partial x}(x,t)\right)^2 dx}_{\text{Strain Energy}} \\ = \underbrace{\int_0^t\int_0^{l_c} f(x,t)\frac{\partial u}{\partial t}(x,t)dxdt}_{\text{Work done}} + \underbrace{constant}_{\text{Initial energy}}\end{aligned} \tag{A-26}$$

Where the work is the integrand of $F \cdot v$. Equation A-1 is inserted, with $T_i(t)$ of the homogeneous solution replaced with $\eta_i(t)$ for the particular solution and reorder:

$$\begin{aligned}\sum_{i=1}^{\infty}\left(\frac{1}{2}\left(\rho_c A_c\int_0^{l_c}U_i^2(x)dx+MU_i^2(x=l_c)\right)\dot{\eta}_i(t)^2+\frac{1}{2}E_cA_c\int_0^{l_c}U_i'^2(x)dx\ \eta_i(t)^2\right)\\=\sum_{i=1}^{\infty}\left(\int_0^t\int_0^{l_c}f(x,t)U_i(x)dx\ \dot{\eta}_i dt\right)+constant\end{aligned}\tag{A-27}$$

Differentiate both sides one time with respect to time:

$$\begin{aligned}\sum_{i=1}^{\infty}\left(\left(\rho_cA_c\int_0^{l_c}U_i^2(x)dx+MU_i^2(x=l_c)\right)\ddot{\eta}_i(t)\dot{\eta}_i(t)+E_cA_c\int_0^{l_c}U_i'(x)^2dx\dot{\eta}_i(t)\eta_i(t)\right)\\=\sum_{i=1}^{\infty}\int_0^{l_c}f(x,t)U_i(x)dx\dot{\eta}_i(t)\end{aligned}\tag{A-28}$$

As the inside of the summation signs is only dependant on i and no other modes, the equations can be taken out to investigate the dynamics of each separate mode i. Substitution of Equation A-22 with $i=j$ in the foregoing equation in place of $\int_0^{l_c}U_i'(x)^2dx$, substitution of the constant c and taking out common terms in variable M_i results in:

$$M_i\ddot{\eta}_i(t)\dot{\eta}_i(t)+\omega_i^2M_i\dot{\eta}_i(t)\eta_i(t)=\int_0^{l_c}f(x,t)U_i(x)dx\dot{\eta}_i(t)\tag{A-29}$$

$$M_i\equiv\rho_cA_c\int_0^{l_c}U_i^2(x)dx+MU_i^2(x=l_c)\tag{A-30}$$

The equality has to hold for each $\dot{\eta}_i(t)$, including the trivial solution of $\dot{\eta}_i(t)=0\ \forall t$. As the trivial solution is clearly valid in this equation, it can be divided by $\dot{\eta}_i(t)$ and reordered:

$$M_i\left(\ddot{\eta}_i(t)+\omega_i^2\eta_i(t)\right)=\int_0^{l_c}f(x,t)U_i(x)dx\tag{A-31}$$

Now $\ddot{\eta}_i(t)$ can be seen to be equal to:

$$\ddot{\eta}_i(t)=-\omega_i^2\eta_i(t)+\frac{\int_0^{l_c}f(x,t)U_i(x)dx}{M_i}\tag{A-32}$$

Appendix B

Parameters used for Simulation

The results shown in this Thesis are dependant on the used parameters of for example the cable, payload and heave compensation cylinder actuator. A selection of these parameters is quantified here.

	Cable and payload properties	**value**	**unit**
A_c	nominal metallic area	87×10^{-3}	[m^2]
D_c	cable diameter	118×10^{-3}	[m]
E_c	apparent Young's modulus of the cable	100	[GPa]
	maximum breaking force	11×10^3	[kg]
ρ_c	specific density of the cable	7800	[kg/m^3]
ζ	material damping term of the cable	0.01	
A_p	(vertical) projected area of the payload	4	[m^2]
	height of the payload	2	[m]
d_{c-w}	Hydrodynamic damping term of cable due to water	0.02	
d_{p-w}	Hydrodynamic damping term of payload due to water	1	
	added mass coefficient	0.7	

	heave compensation cylinder properties	**value**	**unit**
A_{pc}	passive cylinder area	0.3	[m^2]
A_{ac}	active cylinder area	0.07	[m^2]
d_{visc}	viscose damping term of the heave compensation cylinder	170×10^3	[Ns/m]
d_{cyl}	linearised damping constant of the heave compensation cylinder	320×10^3	[Ns/m]
E_{oil}	Young's modulus of hydraulic oil	1.4	[Gpa]
F_{coul}	static Coulomb friction force	150×10^3	[N]
m_{act}	moving mass of the actuator	20×10^3	[kg]
	Cylinder maximum stroke	5	[m]
V_0	initial gas volume in the accumulator	6.5	[m^3]
κ	adiabatic gas constant	1.61	

Appendix C

Additional Figures

In this Appendix some figures are placed, which are referred to in Chapter 6. Information from these figures is used to generate the conclusions of Chapter 6, which is visualised here.

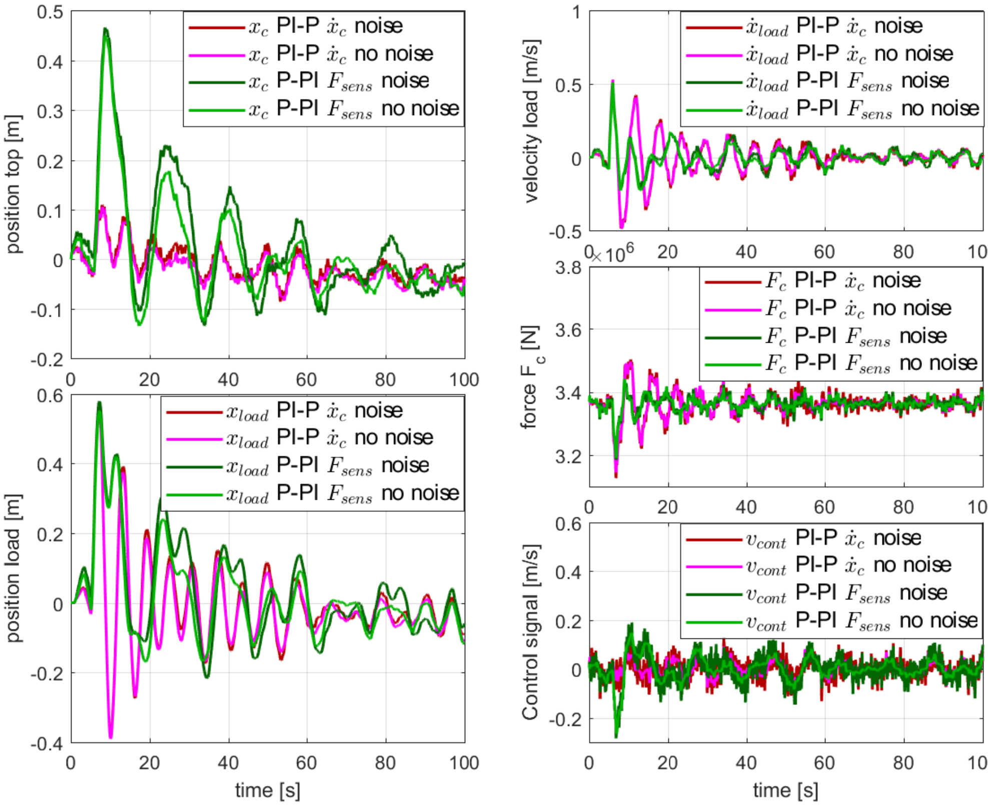

Figure C-1: Simulations of the PI-P $\dot{x}_c$ and P-PI F_{sens} with and without noise. Simulated with a cable length of $3000\,\mathrm{m}$ and a payload mass of $175 \times 10^3\,\mathrm{kg}$ with heave and disturbance on F_{load}. It can be seen that noise causes worse performance in reducing the payload's motion due to the disturbance on F_{load}, which is most visible with x_{load}. Less visible is that the noise causes more high frequency variations on F_c for both controllers, as well as larger feedback signals. The depicted v_{cont} is only the feedback part of the control signal. The PSD of the same simulations is depicted in Figure C-2.

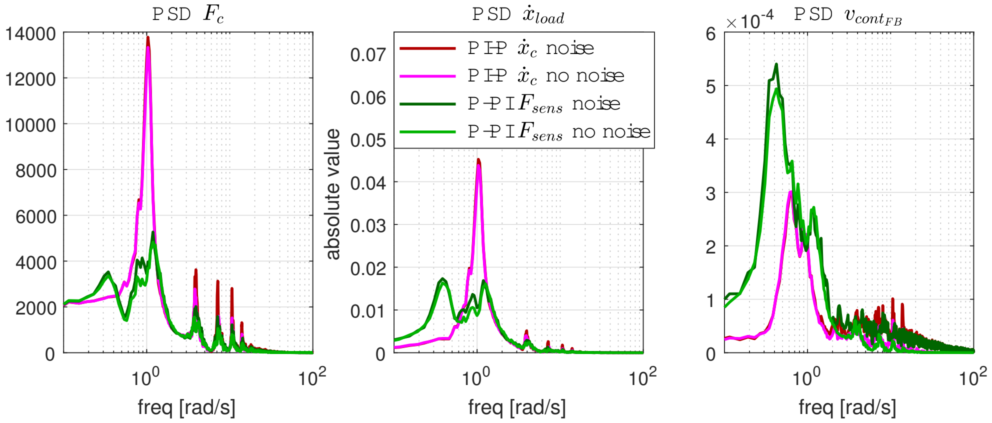

Figure C-2: PSD analysis of the P-PI F_{sens} with multiple delay values. Simulated with a cable length of $3000\,\mathrm{m}$ and a payload mass of $175 \times 10^3\,\mathrm{kg}$ with heave and disturbance on F_{load}. It is clearly visible that the performance of the controller decreases noise as the PSD's with noise are practically at every frequency higher than the PSD without noise for the same controller. Especially at the resonance frequencies between 3 and $20\,\mathrm{rad/s}$ the PSD of F_c and $\dot{x}_{load}$ is significantly larger. Also the control signal at high frequencies is a lot larger when noise is added, as could be expected. The time domain is depicted in Figure C-1.

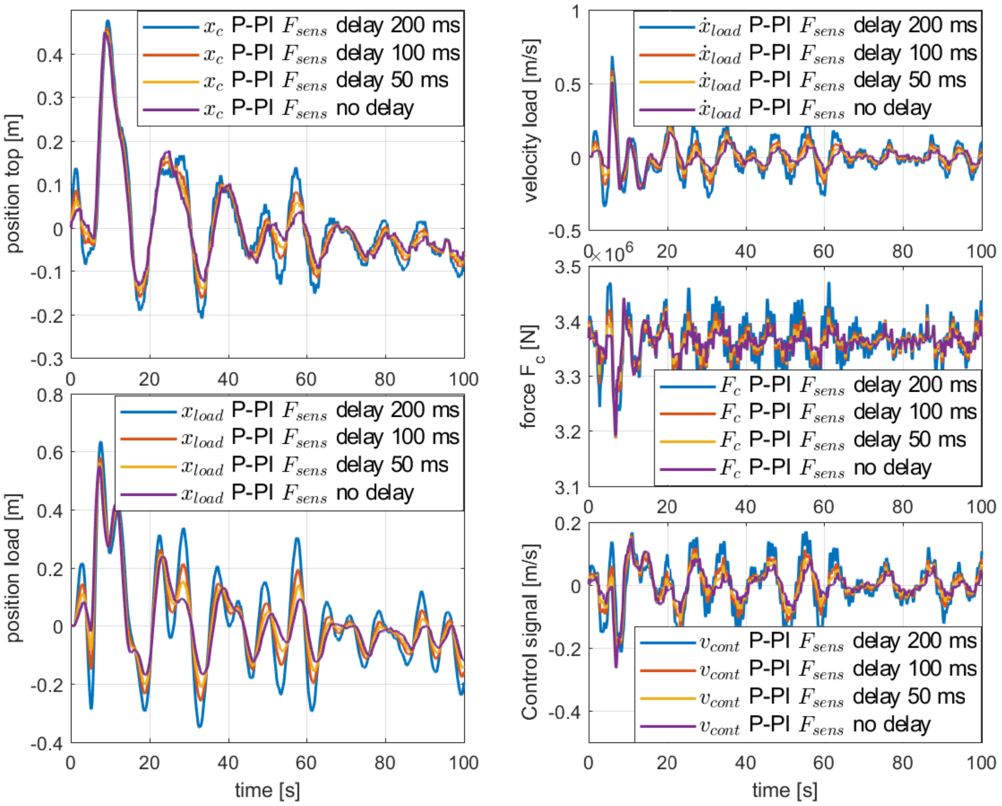

Figure C-3: Simulations of the P-PI F_{sens} with multiple delay values. Simulated with a cable length of $3000\,\mathrm{m}$ and a payload mass of $175 \times 10^3\,\mathrm{kg}$ with heave and disturbance on F_{load}. It is clearly visible that the performance of the controller decreases with larger delays and that larger control actions are used. Note that the control action is only the feedback part of the control signal ($v_{cont_{FB}}$). The PSD of the same simulations is depicted in Figure C-4.

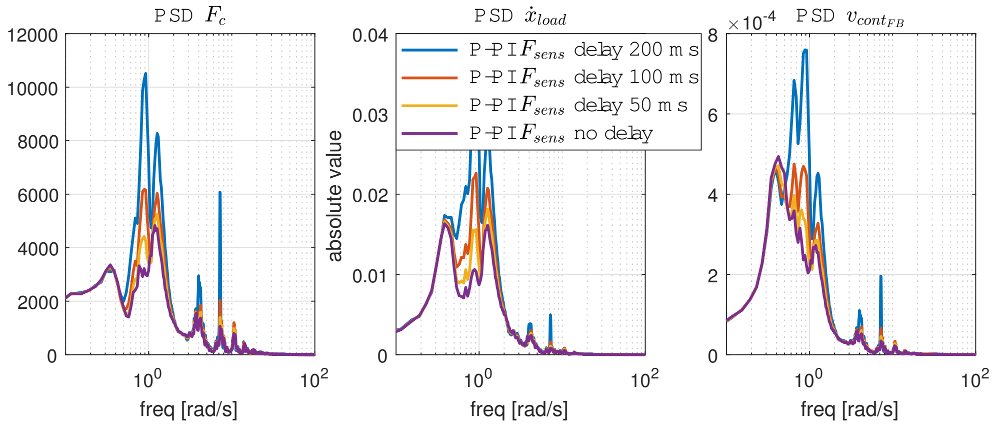

Figure C-4: PSD analysis of the P-PI F_{sens} with multiple delay values. Simulated with a cable length of $3000\,\mathrm{m}$ and a payload mass of $175 \times 10^3\,\mathrm{kg}$ with heave and disturbance on F_{load}. It is clearly visible that the performance of the controller decreases with larger delays and that larger control actions are used. The time domain is depicted in Figure C-3.

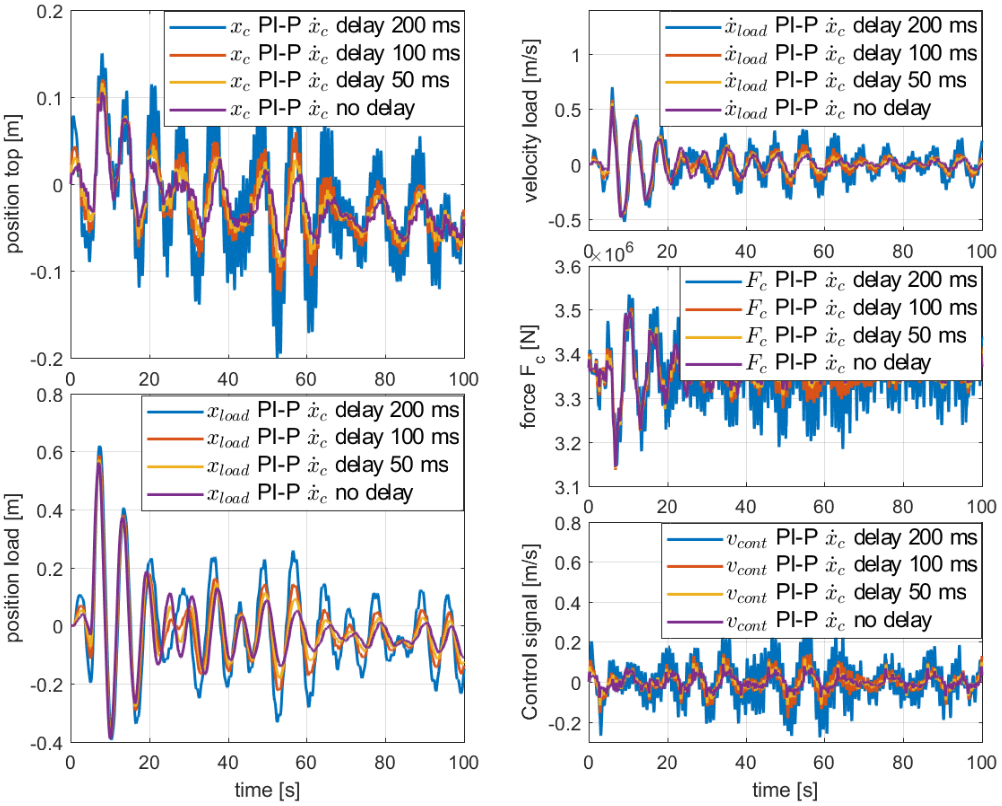

Figure C-5: Simulations of the PI-P $\dot{x}_c$ with multiple delay values. Simulated with a cable length of $3000\,\mathrm{m}$ and a payload mass of $175 \times 10^3\,\mathrm{kg}$ with heave and disturbance on F_{load}. It is clearly visible that the performance of the controller decreases with larger delays and that larger control actions are used. Note that the control action is only the feedback part of the control signal ($v_{cont_{FB}}$)The PSD of the same simulations is depicted in Figure C-6.

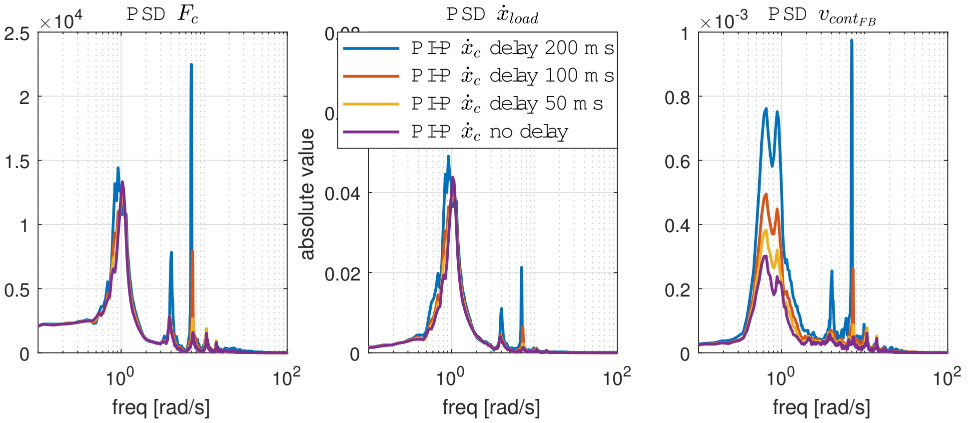

Figure C-6: PSD analysis of the PI-P $\dot{x}_c$ with multiple delay values. Simulated with a cable length of $3000\,\mathrm{m}$ and a payload mass of $175 \times 10^3\,\mathrm{kg}$ with heave and disturbance on F_{load}. It is clearly visible that the performance of the controller decreases with larger delays and that larger control actions are used. The time domain is depicted in Figure C-5.

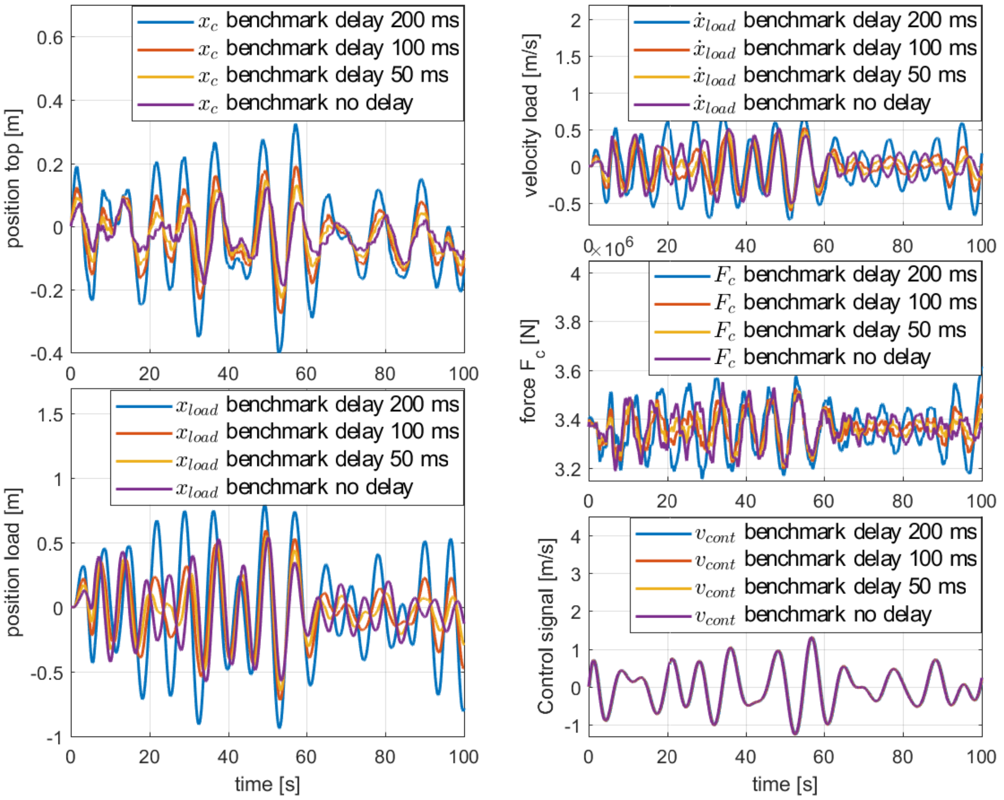

Figure C-7: Simulations of the benchmark controller with multiple delay values. Simulated with a cable length of $3000\,\mathrm{m}$ and a payload mass of $175 \times 10^3\,\mathrm{kg}$ with heave and disturbance on F_{load}. It is clearly visible that the performance of the controller decreases with larger delays and that larger control actions are used. Note that the control action is only the feedforward part of the control signal ($v_{cont_{FF}}$)The PSD of the same simulations is depicted in Figure C-8.

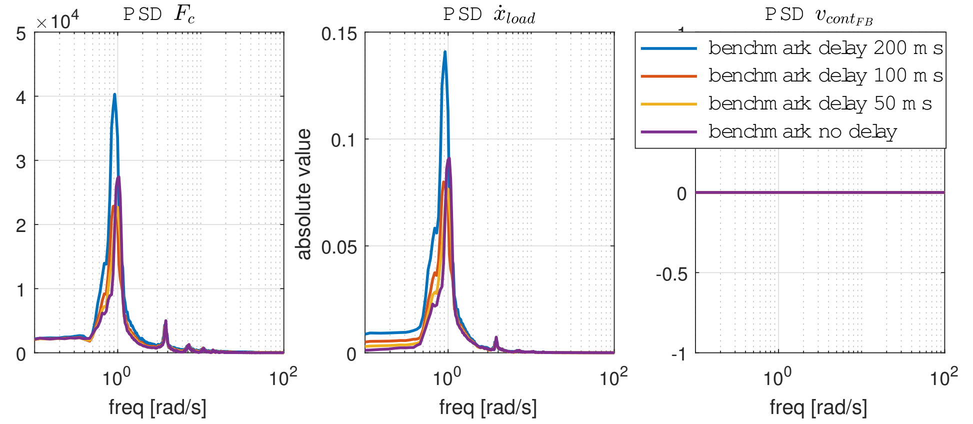

Figure C-8: PSD analysis of the benchmark controller with multiple delay values. Simulated with a cable length of $3000\,\mathrm{m}$ and a payload mass of $175 \times 10^3\,\mathrm{kg}$ with heave and disturbance on F_{load}. It is clearly visible that the performance of the controller decreases with larger delays and that larger control actions are used. The time domain is depicted in Figure C-7.

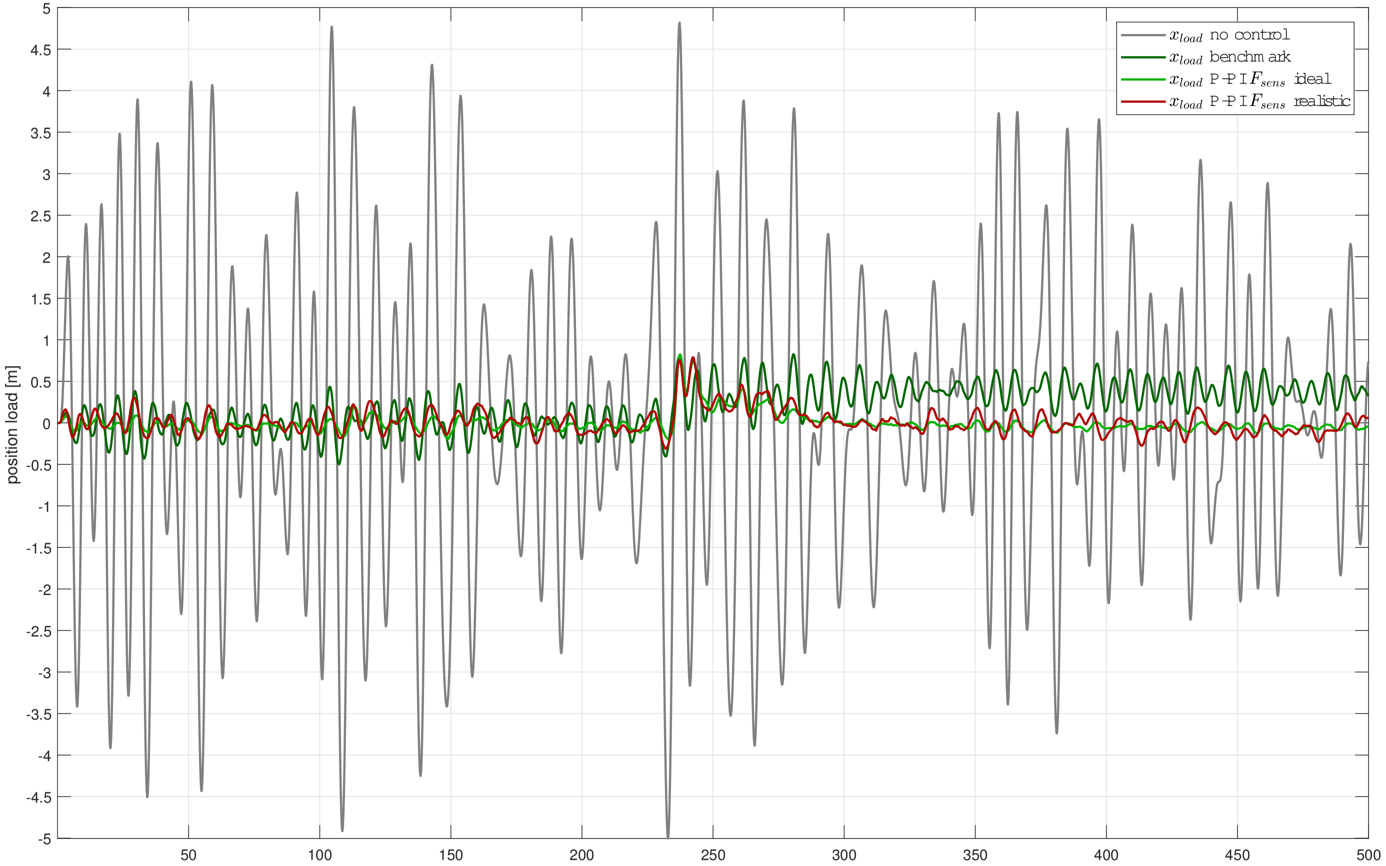

Figure C-9: Simulations no control, compared to the benchmark controller and the parallel P-PI F_{sens} with ('realistic') and without ('ideal') noise and delays. It can be seen that the feedforward control (benchmark) has a large improvement over 'no control'. The both P-PI F_{sens} simulations are in their turn an improvement to the benchmark controller. At around $t = 230\,\mathrm{s}$, the heave velocity is larger than the maximum control speed of the heave compensation cylinder due to the capability of the driving pump. As can be seen, this results in an offset of the benchmark controller, while this is compensated by the P-PI F_{sens} controllers. Furthermore it can be seen that the P-PI F_{sens} controller's performance at x_{load} decreases under influence of noise and delays, but performs still better than the benchmark controller. Simulation performed with a cable of $3000\,\mathrm{m}$ and a $175 \times 10^3\,\mathrm{kg}$ payload and only heave as disturbance. A close-up of the benchmark and P-PI F_{sens} is depicted in Figure C-10.

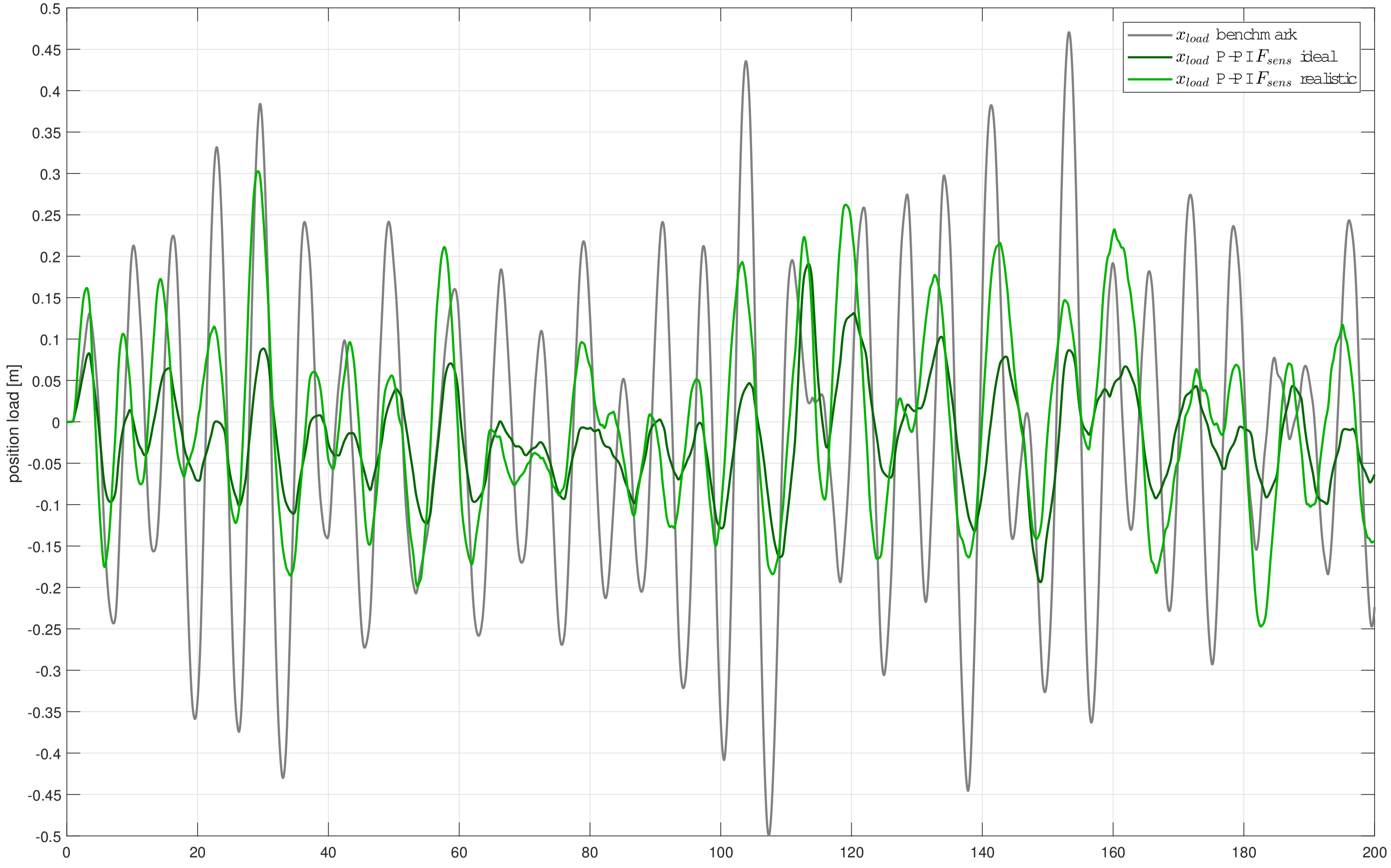

Figure C-10: Simulations of the benchmark controller, compared to the parallel P-PI F_{sens} with ('realistic') and without ('ideal') noise and delays. Both P-PI F_{sens} simulations are an improvement to the benchmark controller. It can be seen that the P-PI F_{sens} controller's performance at x_{load} decreases under influence of noise and delays, but performs still better than the benchmark controller. Simulation performed with a cable of $3000\,\mathrm{m}$ and a $175 \times 10^3\,\mathrm{kg}$ payload and only heave as disturbance. This figure is a close-up of Figure C-9.

Bibliography

[1] J. Verhage, "Heave compensation, optimized for deep sea, literature survey," Master's thesis, Delft University of Technology, 3mE, 2017.

[2] J. Woodacre, R. Bauer, and R. Irani, "A review of vertical motion heave compensation systems," *Ocean Engineering*, vol. 104, pp. 140–154, June 2015.

[3] C. Amante and B. Eakins, "Etopo1 1 arc-minute global relief model: Procedures, data sources and analysis. noaa technical memorandum nesdis ngdc-24, 19 pp," 2009.

[4] P. Albers, *Motion Control in Offshore and Dredging.* Springer Netherlands, 1 ed., 2010.

[5] A. Heinze, "Modelling, simulation and control of a hydraulic crane," Master's thesis, School of Technology and Design, Munich University of Applied Sciences, 2007.

[6] S. Küchler, T. Mahl, J. Neupert, K. Schneider, and O. Sawodny", "Active control for an offshore crane using prediction of the vessel's motion," *IEEE/ASME Transactions on Mechatronics*, vol. 16, pp. 297–309, April 2011.

[7] J. Neupert, T. Mahl, B. Haessig, O. Sawodny, and K. Schneider, "A heave compensation approach for offshore cranes," in *2008 American Control Conference*, pp. 538–543, June 2008.

[8] S. S. Rao, *Vibration of Continuous Systems.* Wiley, 2007.

[9] A. Nestegard and T. Boe, *Modelling and analysis of marine operations.* Det Norske Veritas, Norway, April 2009.

[10] T. I. Fossen and T. Perez, "Marine systems simulator (mss)." http://www.marinecontrol.org, 2004.

[11] Q. Yuan, "Actively damped heave compensation (adhc) system," in *Proceedings of the 2010 American Control Conference*, pp. 1544–1549, June 2010.

Glossary

List of Acronyms

HC	Heave Compensation
AHC	Active Heave Compensation
PHC	Passive Heave Compensation
HHC	Hybrid Heave Compensation
IMU	Inertial Measurement Unit
IHC	IHC Systems, part of Royal IHC
MSS	MATLAB-toolbox Marine Systems Simulator
SWH	Significant Wave Height
PDE	Partial Differential Equation
GM	Gain Margin
PM	Phase Margin
PSD	Power Spectral Density